Effect of Tissue Viscoelasticity and Stiffness on Hemodynamics and Endothelial Cell Signaling

By,

Winston Elliott

A thesis submitted to the
Faculty of the Graduate School of the
University of Colorado in partial fulfillment
of the requirement for the degree of
Doctor of Philosophy
Department of Mechanical Engineering
November 15, 2017

Advisors:

Wei Tan

Claudio Migliaresi

Antonella Motta

This thesis entitled:

Effect of Tissue Viscoelasticity and Stiffness on Hemodynamics and Endothelial Cell Signaling
written by Winston Howard Elliott

has been approved for the Department of Mechanical Engineering

—————————————————————

Dr. Wei Tan

—————————————————————

Dr. Virginia Ferguson

Date—————————————

The final copy of this thesis has been examined by the signatories, and we
find that both the content and the form meet acceptable presentation standards
of scholarly work in the above mentioned discipline.

Elliott, Winston H. (Ph.D., Mechanical Engineering)

Effect of Tissue Viscoelasticity and Stiffness on Hemodynamics and Endothelial Cell Signaling

Dissertation directed by Associate Professor Wei Tan

Cardiovascular disease (CVD) is the most common cause of death in the United States of America, accounting for 24% of all deaths each year,(Anderson et al., 2003) and is projected to rise above 20% globally by 2030.(Mathers and Loncar, 2006) Options for CVD treatment do exist, but are limited by availability of healthy replant tissue from the patient or long term effectiveness and failure rates of both autologous tissue grafts and artificial implants. Grafting failure may often be attributed to the poor mimicry of the site-specific, healthy arterial tissue. While much TEVG research focuses on endothelialization of the graft lumen through chemical signaling, mechanotransduction plays a large role in forming and maintaining a healthy endothelial cell (EC) monolayer. Arteries and grafts interact with hemodynamics to determine flow pulsatility and create healthy, or pathological, mechanical signaling environments. Though arterial tissue is known to be viscoelastic,(Armentano et al., 2006; Bergel, 1961; Bia et al., 2006) the importance of this in developing healthy blood flow is undetermined. Therefore, a gap in the knowledge occurs in the importance of arterial mechanics affecting graft outcomes. To address this we attempt to examine specific shortcomings: 1) Determine whether pathological flow is capable of maintaining EC monolayer in a low arterial compliance model, 2) Establish methods of catering protein hydrogel frequency-dependent properties towards establishing biodegradable materials intended for TEVG, 3) Determine benefits of viscous wall damping in improving hemodynamics towards improved cell response.

This proposal centers on improving cell response to pathological hemodynamics through catered viscoelastic material response at the arterial wall. To address this, we hypothesize that maintaining healthy EC monolayer is predicated on hemodynamic mechanotransduction, which results from both graft compliance and viscous damping of the material. To validate this hypothesis, we examine healthy and

pathological hemodynamic effects on EC monoculture, and systematically determine the role of

viscoelastic material response in maintaining healthy hemodynamics.

Table of Contents

Tables

Figures

Chapter 1

Introduction & Background

Cardiovascular disease (CVD) is the most common cause of death in the United States of America, accounting for 24% of all deaths each year,(Anderson et al., 2003) and is projected to rise above 20% globally by 2030.(Mathers and Loncar, 2006) Arterial stiffening and narrowing are important signals in CVD, including myocardial infarction, heart failure, and overall mortality.(Zieman et al., 2005) Decreased compliance and luminal narrowing are directly responsible for high pulsatile flow (HPF),(Mitchell, 2008; Stewart and Lyman, 1992; Tan et al., 2014) which is linked to the inflammatory response, vascular fibrosis, intimal hyperplasia (IH), and endothelial-to-mesenchymal transition.(Elliott et al., 2015; Scott et al., 2013) Conduit arteries, such as the carotid, femoral, or coronary are important in maintaining physiologic hemodynamics and preventing CVD. Increased resistance in conduit arteries may reduce transport downstream, and increase left ventricular work, which is tied to many vascular diseases. These phenomena result from the influence of material mechanics on blood flow, and resulting dynamic shear signaling on cell response. Therefore, understanding fluid-structure interaction in arterial blood flow is important in determining pathological mechanical and hemodynamic changes, as well as new avenues for treatment.
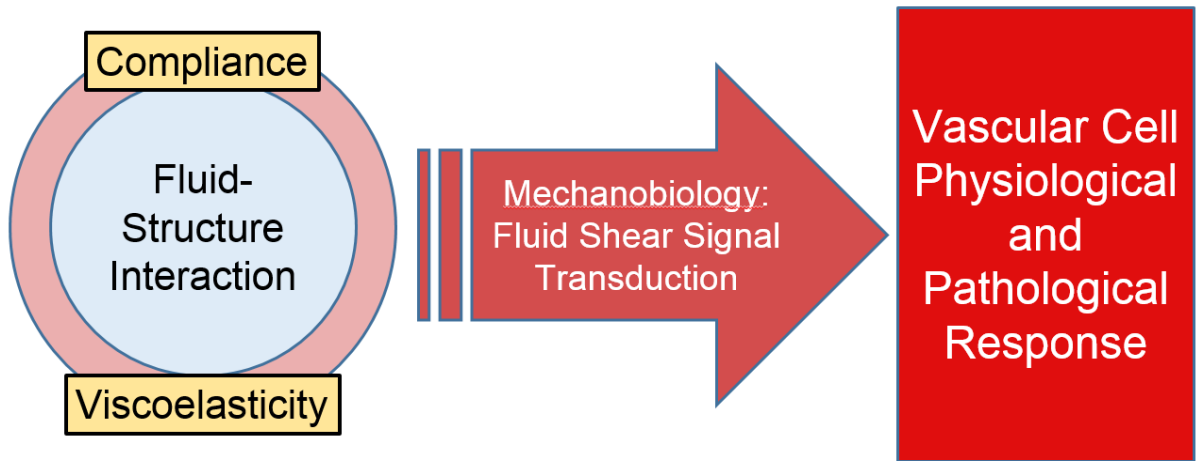
Figure 1.1- Scheme of proposed dissertation. Effect of arterial compliance and viscoelasticity on fluid body, and resulting mechanical signaling of vascular cells.

Examining the past 25 years of arterial health and disease, focus has gradually shifted from static vascular geometries towards dynamic response of the wall, and their respective contributions to haemodynamic signaling of the cells. This has coincided with improved imaging of time-dependent response of tissues *in situ*. Early emphasis in mechanical propagation of the disease state revolved around geometry of the arterial tree, including branching, bifurcation, and anastomoses interaction with pulsatile flow.(Kim et al., 1993; Ku et al., 1985; Ojha, 1994) While the importance of compliance mismatch had been examined over the past 25 years,(Abbott et al., 1987; Friedman et al., 1992; Okuhn et al., 1989; Shadwick, 1999) arterial mechanics as a measure of health have been a focus in the past 10-15 years.(Gessaroli et al., 2012; Liu et al., 2010; Wagenseil and Mecham, 2009) This has allowed for treatment design schemes to shift towards maintaining dynamic mechanical response of arterial walls.(Greenwald and Berry, 2000; Inoguchi et al., 2006; Madhavan et al., 2013; Nagiah et al., 2015; Sarkar et al., 2006) Time-dependent response of the arterial wall has garnered more attention in the past 10 years.(Armentano et al., 2014; Bia et al., 2006; Valdez-Jasso et al., 2011) This has led to viscoelastic properties of arteries being used as a metric of health,(Liu et al., 2015; Wang et al., 2013c) and coincided with application of time-dependent materials in tissue replacement treatments,(Zhao, 2014; Zhao et al., 2014), including vascular grafting.(Nagiah et al., 2015; Neufurth et al., 2015) Further understanding of

the interaction between viscoelastic properties and haemodynamics is important moving forward in both understanding vascular health, and defining treatment design criteria.
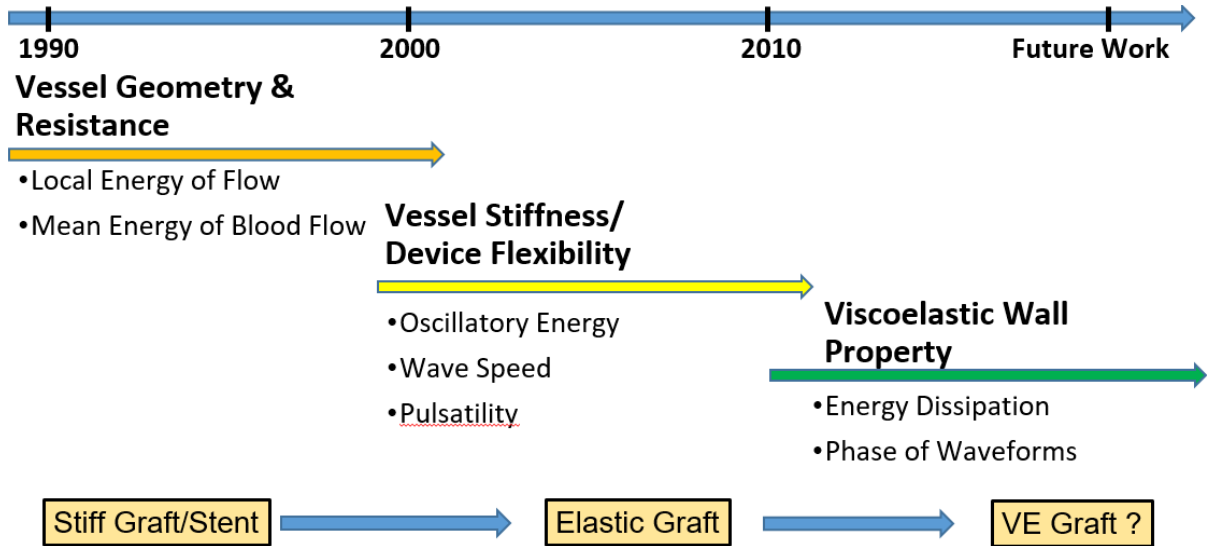
Figure 1.2- Historical perspective of arterial mechanics contributing to disease and resulting treatment designs.

This dissertation reports a comprehensive study, expanding on the importance of mechanical signaling in maintaining healthy arteries, integrating time-dependent material property design schemes into an experimental platform for studying vascular mechanics to improve our understanding of the relationship between blood flow and vascular material properties. By expanding on this complex relationship, we may help provide direction in further understanding arterial health and vascular graft design. Chapter 2 reports our comprehensive reviews of state-of-the-art understanding of vascular mechanobiology, and its application to improve treatments. Chapter 3 reports our own contribution towards understanding cellular mechanotransduction of high pulsatility flow (HPF) in the vasculature. Chapter 4 is our study on time-dependent material design schemes of a biodegradable material, silk fibroin. Chapter 5 reports the results of time-dependent properties on pulse wave propagation, and therefore mechanical signals applied to vascular cells. Chapter 6 concludes and discusses the overall study by highlighting important findings and provides suggestions for future direction in the area.

1.1 Arterial Properties

Vasculature may be separated into three distinct layers: the intima, media, and adventitia. Endothelial cells line the inner lumen of the vasculature, and are attached to the basal media, which forms the tunica intima. Tunica intima structure contributes little to overall vascular stiffness, as it is approximately 1-2 microns thick with elastic modulus of 1-3 kPa.(Peloquin et al., 2011) Alternately, in muscular arteries such as the carotid, femoral, and coronary arteries, extra cellular matrix (ECM) of the media contributes to 50% of the dry weight. The media layer consists of layered elastin lamellae, which alternate with collagen, vascular smooth-muscle cells (vSMC), and high proteoglycan layers. This layer is largely responsible for material properties within the physiologic range,(Wagenseil and Mecham, 2009) and the viscoelastic response of muscular arteries.(Armentano et al., 1995) . Additionally, proteoglycan (PG) content contributes to tissue swelling and hydration, and has been shown to provide poroelastic viscous response within other tissues.(Korhonen et al., 2003) The adventitia, or outer layer, is primarily composed of Collagen Type-I (COL-I) and fibroblasts (FB), and counters vessel over-distension.(Dobrin, 1978; Wagenseil and Mecham, 2009)

The highly elastic, and relatively soft elastin layering within the media acts as an energy reservoir within the aorta. During systole, the aorta undergoes significant strain, which decreases as during aging.(Redheuil et al., 2010) Contrastingly, the muscular arteries, such as the carotid, femoral, and coronary exhibit stiffer wall properties, and greater viscous material response (Figure 1.1.1).(Armentano et al., 1995, 2014; Bergel, 1961; Bia et al., 2006; Learoyd and Taylor, 1966)
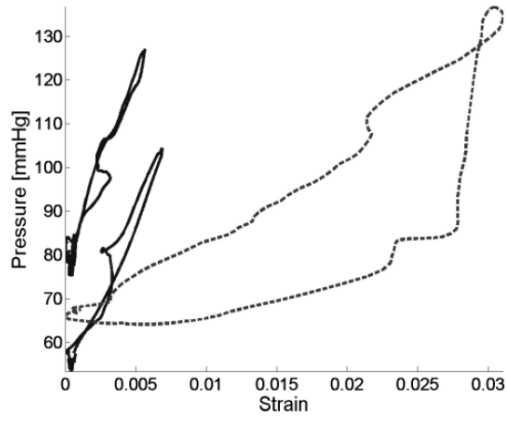
Figure 1.1.1- Noticeable hysteresis curve from ovine femoral artery (dashed line), as compared to artificial polymer material (Poly(L-lactic acid), solid line). Image taken from Armentano. (Armentano et al., 1995)

This may be seen in histological comparison of ECM and cellular content, with muscular arteries exhibiting much greater SMC and PG content (Figure 1.1.2). These properties may directly relate to flow and pressure wave attenuation in healthy physiology, decreasing pulsatility and improving cell response downstream.
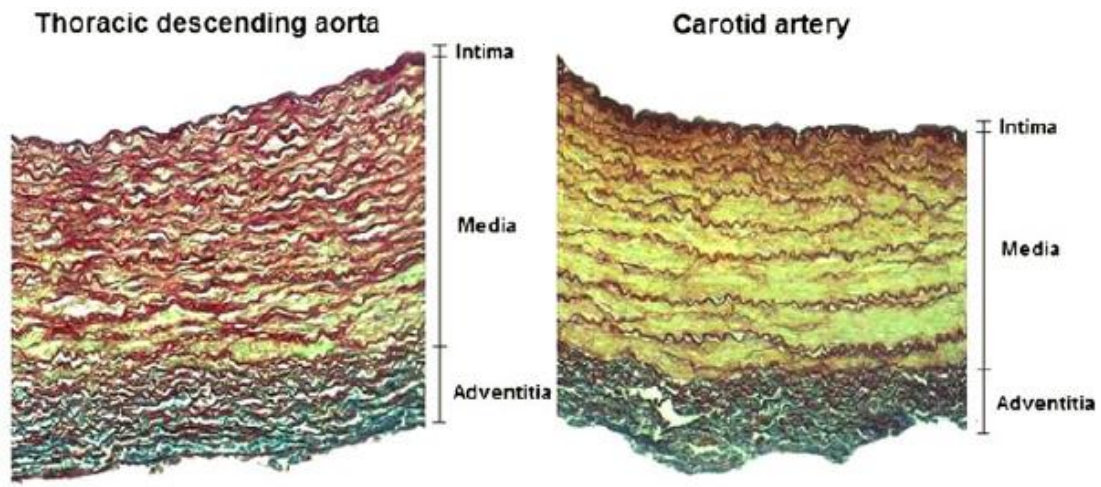
Figure 1.1.2- Representative cross sections of the aorta and muscular arteries. Material components were stained using the Cajal-Gallengo histological method, with smooth muscle cells (yellow), elastin

(red), and collagen (blue), being the main components imaged. Image taken from Valdez-Jasso, 2011.(Valdez-Jasso et al., 2011)

Fluid shear at the wall, both direction and amplitude, has a significant effect on cell response and disease development, therefore healthy blood flow is important to maintain. There is some disagreement in the literature of how these properties affect wave attenuation. Previously, arterial compliance was described as the main contributor to decreased blood velocity, by increasing the cross-sectional area and maintaining volumetric flow.(O'Rourke et al., 2011) Additionally, conduit artery viscoelasticity has been described as damping pressure and flow wave forms.(Armentano et al., 1998, 2006) This is additionally supported by coupling wall and fluid mechanics, both in continuous body theory, and advanced numerical models.(Raghu and Taylor, 2011) More recently, attenuation has been attributed to pressure wave reflections resulting from impedance disparities between the aorta and muscular arteries.(Mitchell, 2008)

1.2 Disease State

Common disease states in the vasculature are atherosclerotic plaques, vascular fibrosis, and intimal hyperplasia, all of which increase arterial stiffness and eventually lead to occlusion.(Zieman, 2005) Atherosclerosis occurs through the deposition of calcified scar tissue, which may eventually occlude the artery, and is associated with vascular fibrosis and IH.(Lan et al., 2013) Vascular fibrosis and IH exhibit cell proliferation within the vascular intima, though origins of these cells have been indicated throughout all layers of the artery, and are an ill-defined cell-type.(Arciniegas et al., 2000; Berard et al., 2013; Elliott et al., 2015; Frid, 2002; Li et al., 2007; Rekhter et al., 1993; Sakao et al., 2009) Additionally, vascular cells respond with increased matrix metalloproteinase (MMP) and transforming growth factor-β (TGF-β) release, with resulting inflammatory response and COL-I production. This all contributes to adventitial FB migration and endothelial-to-mesenchymal transition (EndMT), as well as increased scarring and

vascular stiffness.(Elliott et al., 2015; Lan et al., 2013; Li et al., 2007; Medici et al., 2011; Owens, 2010; Zeisberg et al., 2007a) Eventually, cell proliferation and migration end in vascular occlusion, or stenosis.

As stated in the preceding section, vascular material properties are important in maintaining healthy hemodynamics. Unhealthy wave reflectance may cause pressure amplification,(O'Rourke and Hashimoto, 2007) and systemically increase flow pulsatility within the peripheral arteries.(Mitchell, 2008) Additionally, locally decreased compliance in arteries, which occurs during the aging process, or other disease states such as vascular fibrosis and IH, increases PI values present.(Okuhn et al., 1989; Tan et al., 2014) As mentioned previously, this is important not only as an indication of pathological flow conditions, but increased PI and HPF are indicated heavily in the inflammatory response, vascular fibrosis, and IH.(Elliott et al., 2015; Scott et al., 2013) Vascular fibrosis, IH, and atherosclerosis all decrease arterial compliance,(Lan et al., 2013; O'Rourke and Hashimoto, 2007; Zieman, 2005) which in turn begins a positive feedback loop, worsening hemodynamics and resulting disease state.

Effects of the disease state on viscoelasticity are unclear, and change between species, anatomical location, and disease types. Viscoelastic arterial response has most frequently been examined in hypertensive patients,(Armentano et al., 1998, 2006; Wang et al., 2013c) though results vary. Previous work examining human common carotid artery indicate similar ratio of viscous to elastic response after remodeling occurs.(Armentano et al., 1998, 2006) This corresponds well with the PG rich medial thickening known to occur in hypertension. Alternately, changes in viscoelastic response to vascular fibrosis have not been thoroughly examined, but it is known that remodeling occurs within the wall material,(Claridge et al., 2009) most likely from increased COL-I presence.

1.3   Cell Response to Fluid Shear

Hemodynamics play a large role in plaque formation, vascular fibrosis, and IH. Normal blood flow involves an oscillating flow waveform which is unidirectional, ergo the mean flow is greater than the waveform amplitude. Blood flow is most easily quantifiable by the pulsatility index (PI), which as

defined as the quotient of peak-to-peak wave amplitude, and mean flow rate ($PI = \frac{V_{Max} - V_{Min}}{\bar{V}}$). Healthy, unidirectional, low pulsatile flow (LPF) occurs when PI is less than one, and is important in maintaining EC homeostasis, and protecting against artherosclerotic pathology.(Chien, 2006) Cells respond to this flow type by maintaining a quiescent state, with elongated morphology in the direction of flow.(Malek and Izumo, 1996)
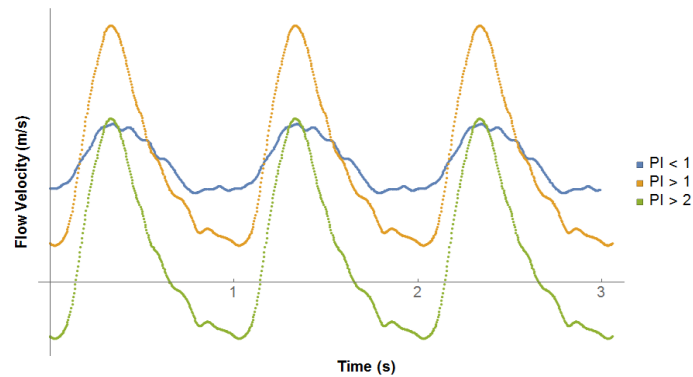
Figure 1.3.1- Examples of different pulsatility indices (PI). Here we see examples of healthy, or low pulsatility flow (LPF → PI < 1.0), pathological high pulsatility flow (HPF→ 1.0 < PI < 2.0), and recursive flow (PI > 2.0).

Pathological flows may be advanced by discontinuities at the wall, or diseased tissue, both of which will increase local PI values. High pulsatile flow (HPF) results from decreased wall compliance, and/or reduction of wave reflection during the pulse cycle. HPF has been shown to induce the inflammatory response, resulting in vascular fibrosis.(Elliott et al., 2015; Scott et al., 2013) This flow type is clinically measured through pathological PI values greater than 1. These PI values correlate with high risk of CVD, in both the elderly,(Mitchell et al., 2011) and diabetics with a history of smoking, hyperlipidemia, and hypertension.(Panaritis et al., 2005) Reciprocating flow defined by PI as greater than two, is indicated at wall discontinuities resulting from compliance mismatch and anastamosa structure.(Chien, 2006; Ku et al., 1985; Ojha, 1994) This additionally contributing to many atherosclerotic pathologies. Both HPF and reciprocating flow are marked by increased PI, inflammation, and IH.

Egorov
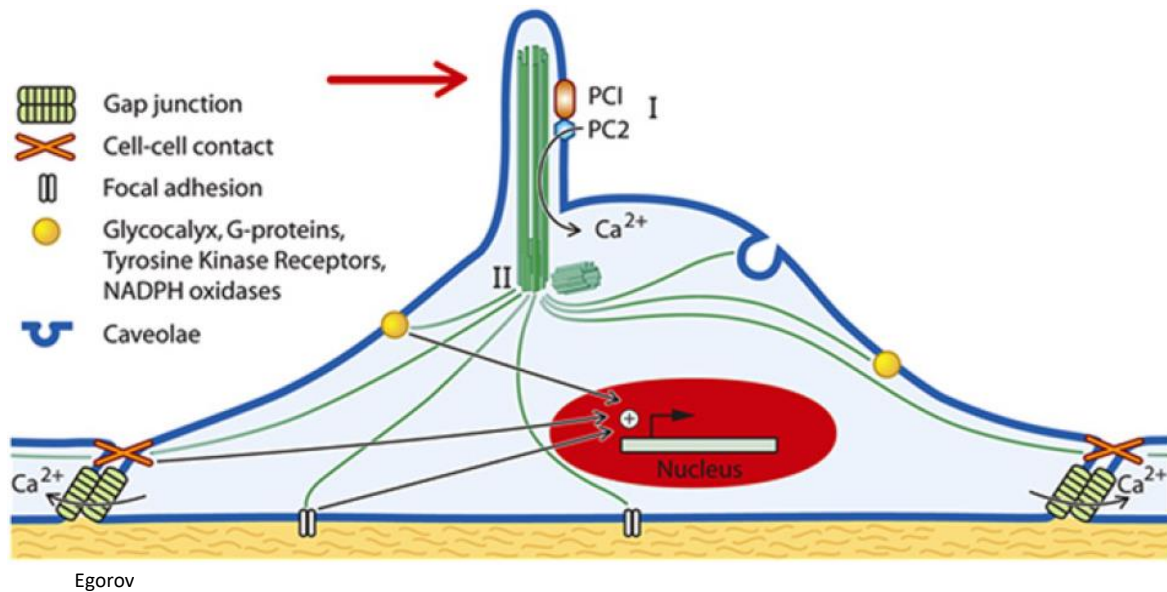
Figure 1.3.2- Cell mechanotransduction in response to fluid shear. Primary cilia, and G-proteins sense fluid shear, causing actin cytoskeleton tension, and subsequently interacting with focal adhesions and cell junctions. This mechanical signal communicates to the nucleus to respond. Image taken from Egorova et al. (Egorova, 2012)

1.4   Treatment Options

Treatment of vascular occlusion has evolved over the years from balloon angioplasty, vascular stenting, and ultimately grafting. Compliance mismatch in many treatments is additionally indicated in producing IH,(Abbott et al., 1987; Fontaine et al., 1994; Okuhn et al., 1989; Seifalian et al., 2002; Stewart and Lyman, 1992) leading to restenosis. The gold standard in vascular grafting is autologous grafts, specifically the saphenous vein. Saphenous veins may not be available in the patient for transplant, and still results in 30-50% failure rate, specifically due to arterial hemodynamics.(Jiang et al., 2009; Morinaga et al., 1987; Owens, 2010) In alternative treatments such as stenting, resulting wall rigidity leads to HPF,(Greil et al., 2003; Vernhet et al., 2001) and IH without drug treatment. The only FDA approved prosthetic graft materials are polyethylene terephthalate (PET), and expanded polytetrafluoroethylene (ePTFE), which may only treat arteries above 6mm in diameter,(Deutsch et al., 2009) and can exhibit a

9

10-40 fold increase in construct stiffness from native arteries.(Bia et al., 2006) While newer artificial graft design has centered on improving compliance,(McKenna et al., 2012; Neufurth et al., 2015; Soletti et al., 2010; Wise et al., 2011) this has been measured as a static, time-independent stiffness response. Most saphenous vein and artificial graft mechanical characterization do not examine dynamic pressure loading of the wall, nor resulting hemodynamics. Above works indicate the necessity and difficulty in matching artery mechanical response, and additionally do not address the dynamic viscoelastic response of arterial tissue, within graft design.

1.5   Conclusion and Impact

Native arterial tissue is viscoelastic, with measurable viscous and elastic properties.(Bergel, 1961; Bia et al., 2006; Gow et al., 1974; Tanaka and Fung, 1974) In artificial graft development, previous work has focused on improved graft compliance.(Hasan et al., 2014; McKenna et al., 2012; Neufurth et al., 2015; Sankaran et al., 2015; Soletti et al., 2010; Wise et al., 2011) But this has not included testing dynamic compliance or hemodynamics,(McKenna et al., 2012; Neufurth et al., 2015; Wise et al., 2011) thereby assuming frequency independence and perfectly elastic response. Mechanical signaling in arterial disease and treatment is important in improving outcomes, understanding the effect of viscoelastic properties in blood vessels on cell response may improve occlusion treatment design. While viscoelastic tissue properties may be important in creating healthy environments for vascular cells, they are rarely mimicked or examined in occlusion solutions. Understanding of the hemodynamic effects on vascular cell populations, in both healthy and pathological flow, may contribute to new directions in treatment design. Therefore, we attempt herein: to determine the effect of compliance on endothelial cell response, explore new avenues in viscoelastic material development for tissue engineering, and establish a bench top model for fluid-structure interaction.
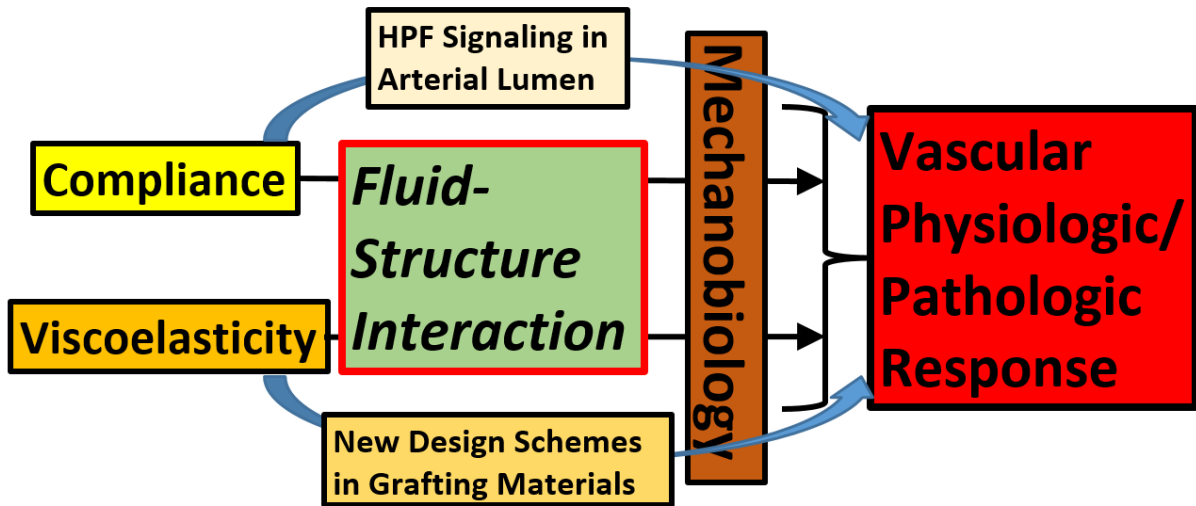
Figure 1.5.1- Project outline: contributions of both compliance and viscoelasticity fluid-structure interaction. This may affect HPF signaling in the arterial lumen, generate new design schemes for grafting materials, and provide insight into arterial mechanics on mechanical signaling of vascular cells.

Chapter 2

Cardiovascular Mechanobiology: Exploitation for Medical Benefit

Winston Elliott[1], Amir Keshmiri[2], Wei Tan[1,*]

[1] *Department of Mechanical Engineering, University of Colorado at Boulder, Boulder, CO 80023, USA.*

[2] *Engineering and Materials Research Centre, Manchester Metropolitan University, Manchester M1 5GD, UK.*

[*] *Corresponding Author:* *wtan@colorado.edu*

2.1 Introduction

Cardiovascular disease (CVD) is the most common cause of death in the United States of America, accounting for 27% of all deaths each year (Anderson et al., 2003), and is projected to rise above 20% globally by 2030 (Mathers and Loncar, 2006). Traditional CVD biomedical research studies have been largely focusing on biochemical signaling cascades which then lead to improved understandings of CVD pathogenesis and thus innovations in CVD treatment. In the last two decades, more attention has been brought to cardiovascular mechanobiology, and researchers have started the journey of exploiting it for medical benefit, including modeling vascular diseases and vascular treatments to unravel insightful understandings and to achieve optimal therapeutic results, respectively. This chapter reviews recent trends in research related to cardiovascular mechanobiology, and contains two main topics, (i) arterial wall mechanics and mechanobiology and its exploitation in understanding arterial disease progression and therapeutics, and (ii) the role of computational hemodynamics in cardiovascular mechanobiology and its exploitation in vascular graft application. We will discuss each particular topic only in its essentials with no intention of exhausting it.

The cardiovascular system is a dynamic, cyclically-loaded, pressure-driven flow system, involving ongoing mechanical feedback loops directing cell response and/or extracellular matrix (ECM) remodeling, which sustains homeostasis of the system, guides adaptive remodeling of the vessel wall, or perpetuates disease progression. Mechanotransduction thus represents an important mechanism in determining vascular health and disease response. Mechanical signals within the vasculature have been shown to be atheroprotective in healthy blood vessels, while initiating or exacerbating vascular lesions in diseased vessels. Current knowledge about mechanical signaling in the cardiovascular system has extended to improve treatment options; for example, performances of many artificial grafting and stenting devices resulting in restenosis may be enhanced, when the local impact of their mechanics on the biomechanical environments in the vascular of neighboring blood vessels as well as the global impact on

the upstream and downstream vascular system are considered for design optimization. To address how the interactions of vascular flow and vessel wall have an impact on vascular health and disease, we begin with an overview on the importance of mechanotransduction to vascular health and the development of different mechanical signals leading to the disease states. We then give examples showing that the pulsatile artery flow interacts with artery structural mechanics to alter mechanical signals, making the healthy vasculature progressing to diseased one. We also review the use of computational flow dynamics (CFD) to explore vascular mechanobiology and guide the design of vascular implants, and finally we suggest the potential avenues for future work using fluid-structure interaction combining CFD and finite element models (FEM) together with the bench mechanobiology models for better understanding of clinical measures and improved design of treatment interventions.

2.2   Arterial Wall Mechanics and Mechanobiology

In general, mechanical signaling in the vasculature originates from the intermittent (or pulsatile) blood flow due to the rhythmic ventricular contractions. The flow travels through the vasculature, interacting with each vascular section and altering its waveform along the way. In particular, the structure and mechanical properties of arteries including conduit elastic arteries and muscular arteries, play important roles in modulating the blood flow, thus influence arterial cell biology as well as ventricular loading and downstream vascular function (). Increased resistance in conduit arteries may reduce transport downstream, and increase ventricular work, which is tied to many vascular diseases. Muscular arteries, such as femoral or coronary arteries, are also important in maintaining physiologic hemodynamics and preventing CVD. Such influences result from the impact of vessel material mechanics or vessel geometry on blood flow in the vessel, which is translated into dynamic shear signaling on cell response promoting vessel homeostasis or vessel adaptive remodeling towards dysfunctional conditions. Arterial stiffening and narrowing (or stenosis), for example, are both important indicators to predict CVD conditions, including myocardial infarction, heart failure, and overall mortality (Zieman et al., 2005). Therefore,

14

understanding how fluid-structure interaction influence flow stresses on vessel wall and resulting cell mechano-sensing and mechano-transduction mechanism of the flow stresses is crucial to modeling and predicting pathological progression of CVD, as well as to the determination of new avenues for treatment optimization.
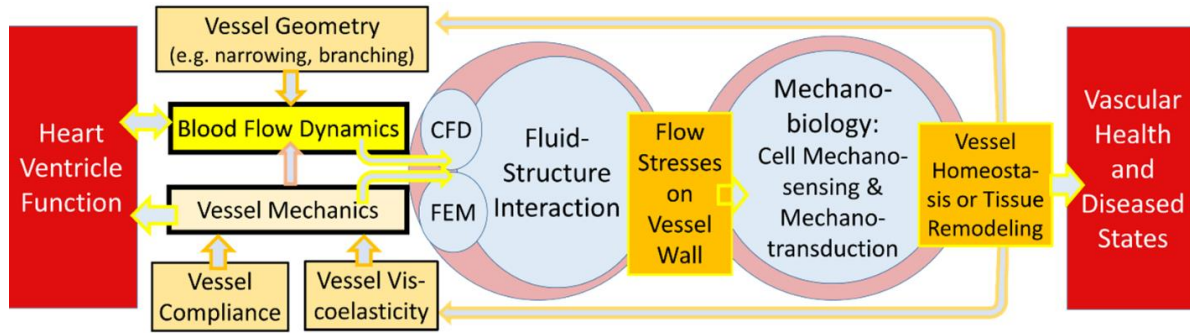
Figure 2.2.1 – The impact of vessel mechanics and geometry on blood flow dynamics through the interaction of flow with vessel wall, which in turn promotes mechano-sensing and mechano-transduction signaling cascades within vascular cells to further determine tissue homeostasis or remodeling and thus vascular healthy or diseased states.

2.3 Mechanical Signal and Mechanotransduction on the Arterial Wall

Historically, chemokine release and reception was the initial paradigm studied towards physiologic and pathologic understanding of vascular tissue response (Gimbrone et al., 1997). Further work in biochemical signaling also emerged, examining extracellular matrix (ECM) ligand and integrin influence on cellular response (Alenghat and Ingber, 2002; Clark and Brugge, 1995; Davis and Senger, 2005). Within the vasculature, this has then progressed to focus on mechanical signaling, another important initiator of cell and tissue adaptation within the artery (Birukov, 2009; Chien, 2006; Chiu and Chien, 2011; Lan et al., 2013). Similar to biochemical signals, mechanical signals applied on the blood vessel wall alters cellular activities, through signaling cascades that lead to morphological, functional and behavioral changes in cells, and thereby remodeling of vascular tissue. Mechanical signals applied onto the blood vessel wall result from three different stresses: compressive stress from hydrostatic pressure,

cyclical circumferential stress from wall stretching, and fluid shear stress. Mechanotransduction occurs in response to application of stresses on the vascular cell, as well as traction forces applied by the cell on the ECM (Davis and Senger, 2005; Huynh et al., 2011; Mason et al., 2013). Additionally, applied stress and resulting strain may be shared amongst cells through cell-cell connections such as vascular endothelial cadherin (Birukov, 2009; Chien, 2006; Chiu and Chien, 2011; Shav et al., 2014). This results in not only localized disease response, but likely also systemic responses within the vasculature.

From the viewpoint of clinical measures, the determination of the mean and/or dynamic pressure and cyclic stretch occurs indirectly through a pressure cuff, or cyclic stretch and fluid velocity values may be measured directly through Doppler ultrasound (McArthur et al., 2011; Mitchell, 2008; Mitchell et al., 2010, 2011). Often, clinical measured hemodynamic results focus on the mean arterial pressure, peak-to-peak pressure values, and the pulsatility index (PI; $PI = \frac{V_{Max} - V_{Min}}{V_{Mean}}$), which may each be differentiated between physiological and pathological values in determining disease states (Armentano et al., 2006; Arribas et al., 2006; Lemarié et al., 2010; Mitchell, 2008; Mitchell et al., 2011; Panaritis et al., 2005).

At the cell and tissue level, studies on mechanical forces applied to the blood vessel have mainly focused on wall stretch stress and fluid shear stress. While hydrostatic pressure exerts compressive stress to affect vascular ECs (Shin et al., 2002), its most important role lies in regulating fluid shear and cyclic stretch through radial expansion of the arterial wall (Ando and Yamamoto, 2009; Birukov, 2009; Chien, 2006; Chiu and Chien, 2011). ECs are especially susceptible to shear forces, with numerous mechano-signaling transduction methods, namely, ion channels, surface glycocalyx, primary cilia, tyrosine kinase receptors, G-proteins, caveolae, adhesive proteins, and simply the cytoskeleton (Ando and Yamamoto, 2009; Chien, 2006; Chiu and Chien, 2011). Cyclic stretch of the vascular wall is also important in determining cell response, for both ECs (Birukov, 2009; Birukov et al., 1995) and smooth muscle cells (SMCs) (Birukov, 2009; Birukov et al., 1995; Haga et al., 2007; Kim et al., 1999; Leung et al., 1976; Mata-Greenwood et al., 2005). These may induce the release of molecules that facilitate paracrine signaling, such as nitric oxide, reactive oxygen species, and protein or steroidal paracrine molecules

16

(Birukov, 2009; Chien, 2006; Chiu and Chien, 2011; Egorova et al., 2011a; Elliott et al., 2015; Leung et al., 1976; Scott et al., 2013; Tan et al., 2014). These biomolecular signals may in turn cause changes in vascular tone, ECM production or degradation, which effectively alter matrix composition and stiffness, and in turn change hemodynamic environment (Birukov, 2009; Chien, 2006; Chiu and Chien, 2011; Davis and Senger, 2005; Noris et al., 1995). Some signal cascades may only occur when mechanical and chemical signals are applied together (Bergh et al., 2009; Birukov, 2009; Mata-Greenwood et al., 2005; Resnick and Gimbrone, 1995; Shav et al., 2014), indicating a complicated signaling network and interplay between chemical and mechanical signaling.

At the subcellular level, vascular cell cytoskeletal structure, cellular protrusion (i.e. primary cilia) as well as cell membrane proteins or macromolecules such as PECAM, VE-cadherin, surface glycocalyx and ion channels, play key roles in sensing or measuring mechanical signals applied on the vessel wall. Cell cytoskeletal structure aids in controlling the cell cycle and regulating proliferation or apoptosis (Chien, 2006; Chiu and Chien, 2011). In particular, cell shape is an indicator of focal adhesion location and density (Caterina, 2000), cytoskeletal restructuring in response to stress (Chien, 2006), and cytoskeletal actin tension. Flow stresses as well as substrate or ECM stiffness and fiber alignment have been shown to play an important role in determining cell spreading and orientation (Chaudhuri et al., 2015; Chien, 2006; Huynh et al., 2011; Mason et al., 2013; Uttayarat et al., 2010). Additionally, ECM chemical structure aids in EC migration to denuded areas (Herbst et al., 1988; Uttayarat et al., 2010), regulates EC activity through focal adhesion kinase (Chien, 2006; Chiu and Chien, 2011; Lu and Rounds, 2012; Wu, 2005; Zebda et al., 2012). Also, specific matrix ligands and their corresponding integrins may further alter cell mechano-sensing and mechanotransduction of flow stress conditions (Wu, 2005). Regarding intracellular signaling molecules involved in flow mechanotransduction, several transcriptional factors as well as epigenetic mechanisms have been identified in recent studies as critical players in ECs that respond to mechanical signals applied on the vessel wall. The regulatory hierarchy of endothelial function includes control at the epigenetic level; very recent reports have highlighted three epigenetic mechanisms in cell

mechanotransduction of flow. MicroRNAs, histone modifications and DNA methylation to endothelial gene expression are all recognized epigenetic regulators that respond to disturbed flow. The discovery of a connection between endothelial cell structures such as cilia and signaling mechanisms at the genetic and epigenetic levels would open a new chapter in our understanding of the molecular mechanisms regulating vascular responses to the changes in flow.

2.4   Physiological and Pathological Responses to Mechanical Signals

Mechanical signaling is an important mediator of healthy vascular activities, affecting both vascular EC and SMC in concert with paracrine signaling. Fluid shear and cyclic wall stretch signaling to cells within the vasculature may preserve a healthy, physiological state (Asakura and Karino, 1990; Bergh et al., 2009; Berk, 2008; Birukov, 2009; Birukov et al., 1995; Ku et al., 1985; Takada et al., 1994; Traub and Berk, 1998; Uttayarat et al., 2010; Zarins et al., 1983), or induce a pathological response (Birukov, 2009; Egorova et al., 2011b; Elliott et al., 2015; Sakao, 2006; Scott et al., 2013; Tan et al., 2014). Importantly, these mechanical signals can exhibit a dose-dependent response (Ando and Yamamoto, 2009; Bergh et al., 2009; Birukov, 2009; Noris et al., 1995; Shav et al., 2014; Takada et al., 1994; Uttayarat et al., 2010), or may be optimized towards physiological ranges (Birukov, 2009; Birukova et al., 2008; Scott et al., 2013; Shi et al., 2009; Shin et al., 2002). Additionally, vascular cells have been found to be phenotypically specific between different vascular branches (Chiu and Chien, 2011; Liu et al., 2008), in that beneficial shear and cyclic stretch values in arteries could initiate inflammation and remodeling response in the venous system (Liu et al., 2008; Owens, 2010). Both wall shear and stretch stresses may work in concert with each other, or with matrix signals, paracrine signals or other biochemical signals (Bergh et al., 2009; Egorova et al., 2011a).

For normal vascular physiology, mechanical signaling plays a critical role in maintaining homeostasis of arteries, with both cyclic stretch and fluid shear sustaining healthy state of the blood vessel. Vascular lumen is lined with a confluent, interconnected, EC monolayer, protecting the lumen from occlusion.

Laminar flow occurs throughout the vasculature, and induces a quiescent state in arteries (Asakura and Karino, 1990; Berk, 2008; Chien, 2006; Chiu and Chien, 2011; Ku et al., 1985; Traub and Berk, 1998; Zarins et al., 1983). Expression of anti-thrombogenic factors (Ando and Yamamoto, 2009; Chien et al., 1998; Takada et al., 1994; Traub and Berk, 1998), cell alignment (Chien, 2006; Chiu and Chien, 2011; García-Cardeña et al., 2001; Resnick and Gimbrone, 1995), cell migration (Chien, 2006; Hsu et al., 2001; Urbich, 2002), EC cell-cell connections (Chien, 2006; Kladakis and Nerem, 2004; Levesque et al., 1986; Traub and Berk, 1998), and nitric oxide (Chiu and Chien, 2011; Noris et al., 1995; Uematsu et al., 1995), are all upregulated by exposure to laminar shear stresses, while monocyte chemotactic protein, and lipid metabolism are downregulated (Chien, 2006; Chiu and Chien, 2011). Luminal laminar flow is additionally effective in preventing SMC and adventitial fibroblast migration (Garanich, 2005; Garanich et al., 2007), and counters inflammatory paracrine signals (Bergh et al., 2009). Additionally, cyclic stretch within the physiological range results in aligned actin and tubulin fibers within the EC (Birukov, 2009; Chien, 2006; Chiu and Chien, 2011), as well as SMC contractility (Birukov, 2009; Birukov et al., 1995; Kim et al., 1999; Leung et al., 1976). Alignment of the EC cytoskeleton, by shear and cyclic stretch, was shown to prevent proliferation or apoptosis (Chien, 2006). Cell-cell connections and cross-talk between EC and SMC are important factors to consider in maintaining homeostasis (Elliott et al., 2015; Liu and Goldman, 2001; Scott et al., 2013; Shav et al., 2014; Sho et al., 2002b; Wang et al., 2006).

Pathological conditions may also be progressed by mechanical signaling, either through reduction in atheroprotective expression (Asakura and Karino, 1990; Chiu et al., 2003; Hsu et al., 2001; Ku et al., 1985), paracrine signaling by ECs (Chien, 2006; Chien et al., 1998; Resnick and Gimbrone, 1995; Scott et al., 2013; Shav et al., 2014), or apoptosis of ECs (Elliott et al., 2015; Sakao, 2006; Shin et al., 2002). While high laminar shear stress (e.g. a mean value of 10-20 dynes/cm^2), in comparison to low shear stress (e.g. 1-2 dynes/cm^2), has been shown to be atheroprotective, shear above threshold values (e.g. 60-100 dynes/cm^2) for the cell type may induce apoptosis, endothelial-to-mesenchymal transition, and remodeling (Chien, 2006; Egorova et al., 2011b, 2012a; Sho et al., 2002a). Alternatively, interstitial flow

19

or low shear stress, induce SMC and adventitial fibroblast migration (Liu and Goldman, 2001; Sakamoto et al., 2006; Shi et al., 2009; Sho et al., 2002b), which may lead to IH when considered in conjunction with increased monolayer permeability. In addition to the mean flow shear conditions, dynamic flow profiles have great effects on disease progression, with increased PI associated with systemic fibrosis (Mitchell, 2008; Mitchell et al., 2011; Panaritis et al., 2005; Scott et al., 2013), endothelial-to-mesenchymal transition,(Elliott et al., 2015) increased lipid metabolism,(Chiu and Chien, 2011) plaque deposition (Asakura and Karino, 1990; Hsu et al., 2001; Ku et al., 1985), and inflammation (Chiu and Chien, 2011; Chiu et al., 2003; Elliott et al., 2015; Scott et al., 2013; Tan et al., 2014). Most notably, clinically measured high PI has indicated systemic fibrosis (Mitchell, 2008; Mitchell et al., 2011; Panaritis et al., 2005), in particular at branching points within the vascular tree, where reciprocal or disturbed flow occurs (Asakura and Karino, 1990; Chien, 2006; Chiu and Chien, 2011; Ku et al., 1985). This could account for shear-induced apoptosis and EC permeability (Chien, 2006; Chiu and Chien, 2011; Elliott et al., 2015), resulting in pathogenic cell migration or material deposition on the sub-endothelial ECM. Cyclic stretch outside physiologic ranges may also increase EC monolayer permeability, exacerbated by reactive oxygen species and VEGF release (Birukov, 2009; Mata-Greenwood et al., 2005), further perpetuating pathological conditions.

2.5 The Role of Vascular Mechanics in Modulating Mechanical Signals

Mechanical signaling within the vasculature is initiated and driven by the volumetric contraction of the heart which produces a complex flow wave that transmits throughout the hierarchical vascular system. The heart contraction causes a pulsatile pressure wave which precedes the volumetric flow wave in the vascular system. Localized pressure-induced stretch stress and flow-induced shear stress on the blood vessel are both reliant on local mechanical properties of the vessel. Radial expansion from resulting pressures increases cross-sectional area, decreasing centerline velocity of blood flow, and resulting fluid

shear at the wall. Therefore, localized remodeling of vessel ECM has an impact on local hemodynamics due to changes in vessel mechanics, and the matrix remodeling may thus exacerbate the disease process.

Arterial compliance has been often related to the maintenance of healthy hemodynamics (O'Rourke et al., 2011). Arterial compliance likely results from changes in elastin and/or collagen content or in vascular tone, and its importance is evident in maintained steady shear values throughout the arterial tree (Humphrey, 2007). The ECM content changes along the arterial tree, with higher elastin content occurring within the aorta, and greater SMC and proteoglycan content in branching, muscular arteries and arterioles (Kawasaki et al., 2005; Valdez-Jasso et al., 2011). This results in different mechanical properties of arteries and varied arterial response to flow, namely an elastic response coming from elastin content, creating a "windkessel" damping effect (O'Rourke et al., 2011; Wagenseil and Mecham, 2009), and a viscoelastic response resulting from proteoglycan content (Armentano et al., 1995). Compliance, and the "windkessel" effect associated with aortic damping of pressure and fluid shear, have been the most commonly examined effect of arterial mechanics on hemodynamics, and have been shown *in vivo* and *in vitro* to decrease PI levels (Elliott et al., 2015; Humphrey, 2007; Scott et al., 2013; Tan et al., 2014). While cell mechanotransduction with steady shear has been studied thoroughly (Chien, 2006; Chiu and Chien, 2011), dynamic flow shear conditions have mostly been examined in clinical settings or computational studies (Mitchell et al., 2010, 2011), and only recently been studied with benchtop models (Elliott et al., 2015; Scott et al., 2013; Tan et al., 2014). Pathological dynamic flow profiles may be related by PI values, with normal physiologic pulsatile flow marked by PI less than one, high pulsatility flow marked by an increased PI value, and oscillating or reciprocating flows with even higher PI. Occurrence of high pulsatility flow was related to systemic fibrosis within the arterial tree (McArthur et al., 2011; Mitchell, 2008; Mitchell et al., 2011), while recursive flow is often indicated in atherosclerotic lesions (Asakura and Karino, 1990; Ku et al., 1985). To further understand the dynamic interaction and relationship of hemodynamics and arterial wall mechanics, studies should be performed to relate wall mechanics to hemodynamics at different vascular disease states. This information will also advise

treatment options. To keep this amount of information manageable, we will limit ourselves to localized responses within the aorta and arteries, leaving systemic effects to other reviews.

Within the aorta, the highly elastic, and relatively soft elastin layering within the media acts as an energy reservoir. During systole, the aorta undergoes significant strain, which decreases during aging (Redheuil et al., 2010). Contrastingly, the muscular arteries, such as femoral and coronary arteries exhibit stiffer wall properties, and greater viscous material response (Armentano et al., 1995; Bergel, 1961). Such difference in arterial wall mechanics may be explained by the histological comparison of ECM and cellular content, in that muscular arteries exhibiting much greater SMC and proteoglycan content. These mechanical properties may directly be related to flow and pressure wave attenuation in healthy vascular physiology, decreasing pulsatility and improving cell response downstream. The effect of wall mechanics becomes more apparent in diseased conditions. In chronic hypertension, for example, increased systemic pressures result in arterial remodeling with initial ECM breakdown and weakening, allowing for luminal expansion and thereby decreasing mean fluid shear, which is followed by wall thickening and ECM stiffening to counter increased pressure (Arribas et al., 2006; Lemarié et al., 2010). Eventually, ECM reconstruction results in decreased elastin content, and increased collagen type-I content with greater crosslinking of the ECM protein, or even calcification of the tissue (Lemarié et al., 2010). Arterial wall stiffening in hypertension has been associated with downstream vascular dysfunction, enhancing risks of stroke and kidney failure. Increased collagen I deposition and calcification on the lumen may additionally be seen in the lumen under recursive flow (Asakura and Karino, 1990; Chien, 2006; Chiu and Chien, 2011; Ku et al., 1985; Peloquin et al., 2011). Atherosclerotic plaque may also build at, and distal to branching points (Asakura and Karino, 1990; Ku et al., 1985), identified by altered flow pulsatility. Stiffness of plaque depositions are much greater (100-300 fold) than healthy ECM (Ebenstein et al., 2009; Peloquin et al., 2011), affecting EC health (Huynh et al., 2011; Mason et al., 2013), and creating surface discontinuities exacerbating local PI values (Ojha, 1994).

Generally speaking, arterial tissue is moderately viscoelastic (Bergel, 1961; Bia et al., 2006; Fung, 1967; Tanaka and Fung, 1974), with significant hysteresis curves present during *in situ* dynamic measurement (Armentano et al., 1995, 2006; Giannattasio et al., 2008). Hysteresis marks energy loss, and wave attenuation in flow, and is predominantly located within the muscular arteries which further reduce pulsatility before flow enters the arterial tree. While the impact of viscous material response within the vasculature is not fully understood, some previous modeling efforts using in vivo pressure/diameter relationships have exhibited significant pressure and flow wave attenuation, especially with increased frequencies associated with exercise (Holenstein et al., 1980; Vignon-Clementel et al.). Remodeling in mild-to-moderate hypertensive patients also suggests the importance of viscous property, when the ratio of viscous-to-elastic damping ratio is still maintained though wall stiffening through media thickening occurs (Armentano et al., 1998, 2006). This provides an interesting new avenue in understanding the fluid-structure relationship and future treatment design.

2.6   Therapeutic Strategies Exploiting Mechanobiology

With the fast increasing research efforts devoted to vascular mechanobiology recently, the next decade may see a big surge in exploiting the new findings to identify novel therapeutic targets, to develop new therapeutic drugs targeting mechanosensing or mechanotransduction pathways, or to enhance disease prognosis and management of CVD. Thereby, the future application perspective of vascular mechanobiology is likely expanded beyond the realm of its current uses, often towards the design of vascular implant devices. Current solutions in small vessel occlusion often results in compliance mismatch, a common cause of restenosis (Abbott et al., 1987; Okuhn et al., 1989; Stewart and Lyman, 1992). The gold standard in vascular grafting, for example, is autologous grafts, specifically the saphenous vein. Saphenous veins may not be available in the patient for transplant, and still results in 30-50% failure rate, specifically due to arterial hemodynamics (Morinaga et al., 1987; Owens, 2010). The anastomosis has long been a source of disturbed flow or high pulsatility flow (Chiu and Chien, 2011; Kim

et al., 1993), and new directions aim to cuff the graft anastomosis to reduce disturbed flow and compliance mismatch (Chiu and Chien, 2011). The only FDA approved prosthetic graft materials are polyethylene terephthalate, and expanded polytetrafluoroethylene (ePTFE), which may only show satisfactory outcomes for treating arteries above 6mm in diameter (Deutsch et al., 2009), and can exhibit a 10-40 fold increase in construct stiffness from native arteries (Bia et al., 2006). Alternatively, the design of tissue engineered vascular substitutes have often centered on improving compliance through incorporation of active biomolecules (McKenna et al., 2012; Neufurth et al., 2015; Soletti et al., 2010; Wise et al., 2011). While some may achieve similar values to native arteries (Wise et al., 2011), these studies often do not examine the hemodynamic response of the proposed graft. Also, testing of compliance focuses on steady-state material responses, assuming little or no frequency dependence. Similar compliance issues also exist in vascular stents which result in enhanced wall stiffness and thus flow pulsatility and tissue remodeling (Greil et al., 2003; Vernhet et al., 2001). These all indicate the necessity and difficulty in matching artery mechanical properties for proper hemodynamics and its beneficial effects on vascular cells. Additionally, current device designs do not address the dynamic viscoelastic response of arterial tissue. The next section provides review and examples of the current work that examines arterial flow environments computationally to aid in parametric design optimizations of vascular implant devices.

2.7   The Role of Haemodynamics in Mechanobiology

2.7.1   Computational Fluid Dynamics

The equations governing fluid flows are a set of coupled, non-linear partial differential equations such as:

Continuity

24

$$\frac{\partial \rho}{\partial t} + \frac{\partial \rho U_i}{\partial x_i} = 0 \tag{2.7.1.1}$$

Momentum

$$\frac{\partial \rho U_i}{\partial t} + \frac{\partial \rho U_i U_j}{\partial x_j} = \frac{\partial P}{\partial x_j} + \frac{\partial}{\partial x_j}\left(\mu \frac{\partial U_i}{\partial x_j}\right) \tag{2.7.1.2}$$

These equations are known as Navier-Stokes equations. Many real problems include additional terms and/or equations, governing heat transfer, chemical species, etc. Analytical solutions are known only for a few very simple flow cases. An alternative is to solve the governing equations numerically, on a computer. Computational Fluid Dynamics (CFD) is this process of obtaining numerical approximations to the solution of the governing fluid flow equations.

One could view CFD as *a numerical experiment*. In a typical fluids experiment, an experimental model must be built and the flow interacting with that model needs to be measured using various measurement devices, and the results are then analysed. In CFD, the building of the model is replaced with the formulation of the governing equations and the development of the numerical algorithm. The process of obtaining measurements is replaced with running an algorithm on the computer to simulate the flow interaction. The analysis of the results is, however, the same for both techniques.

Despite its many advantages, CFD does not remove the need for experiments; numerical models need to be validated to ensure they produce reliable and accurate results. Particularly in clinical applications, there is a pressing need for rigorous model validation against detailed laboratory data. With the growth of available computing power and the advent of powerful user-friendly graphical user interfaces and automated options/features in commercial CFD codes, it has become possible for a wide range of users to apply CFD to even very complex flowfields, giving detailed information about the velocity field, pressure, temperature, etc. This sometimes results in producing solutions that are haemodynamically irrelevant and fail to capture even the most basic flow features.
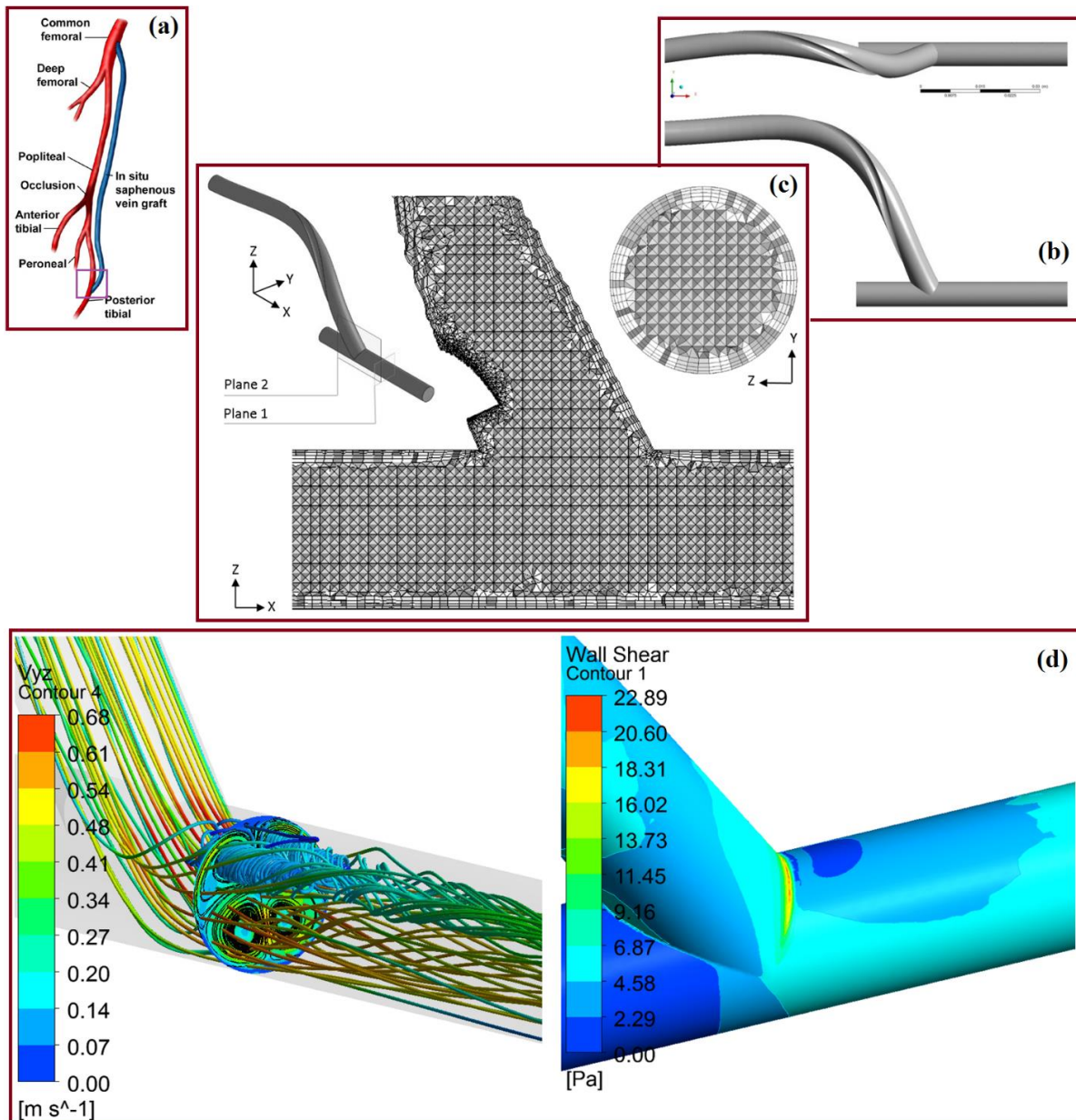
Figure 2.7.1.1- An example of a typical CFD process in a biomedical application: (a) a typical peripheral bypass grafting, (b) the solid Computer Aided Model (CAD) for the computational domain, (c) a hybrid mesh created consisting of quadrilateral cells near the wall boundaries and tetrahedral cells further away from the wall, (d) post-processing of the CFD simulation results using streamlines and contours of the haemodynamic parameters.

2.7.2   Biomedical Applications of CFD

In recent years, advances in vascular biology, biomechanics, medical imaging and computational techniques including CFD have provided the research community with a unique opportunity to analyse the progression of vascular diseases from a new angle and to improve the design of medical devices and develop new strategies for intervention. The increasing power-to-cost ratio of computers and the advent of methods for subject-specific modelling of cardiovascular mechanics have made the CFD-based modelling sometimes even more reliable than methods based solely on *in vivo* measurement. In fact, numerical simulations have played an important role in understanding the haemodynamics in several different clinical cases involving bypass grafting, cardiovascular treatment planning, cerebrovascular flow, the effects of exercise on aortic flow conditions, congenital heart disease and coronary stents.

In addition, the recent developments in patient-specific computer simulations have provided a means to assess new surgeries and interventions at no risk to the patient. Also similar to other engineering fields such as aerospace and automotive, design optimisation is now possible and can be applied to predictive tools and methods to optimise surgeries for individual patients. Therefore, in the new paradigm of predictive medicine, the surgeons for example may use advanced imaging tools along with computational techniques such as CFD to create a patient-specific model and predict the outcome of a particular treatment for an individual patient. However, to be effective and attractive to the medical community, these simulation-based medical planning systems must be quick and efficient and should require minimum user intervention.

2.7.3   Vascular Grafting

In general, there are two broad applications of vascular grafting:

1)   **Arterial Bypass Grafts (ABGs):** Examples of ABGs include peripheral vascular disease (PVD) and coronary artery disease (CAD). Each year over a million vascular grafts (excluding valves)

27

are used in current medical practice. Problems requiring the use of a graft include occluded vessels due to stenosis, damaged vessels resulting from trauma or aneurysm, and the formation of a new tissue structure through regenerative therapies. In ABGs, currently, the "gold standard" option is to use naturally occurring vessels ('autologous' vessels); however, this brings inherent problems including additional surgery for the patient, and the frequent unsuitability or limited availability of their veins due to systemic disease. There is also a lack of viable treatment options when the blood vessel is less than 6mm in diameter (Sarkar et al., 2007). Hence, prosthetic grafts, following either biomaterial or tissue engineered approaches, are utilised. Current prosthetic surgical options commonly include Dacron (polyethylene terephthalate, PET) and Teflon (expanded polytetrafluoroethylene, ePTFE). Unfortunately, prosthetic grafts are known to exhibit unsatisfactory long-term performances (Haruguchi and Teraoka, 2003), therefore, much research is being performed to reduce failure rates and improve patency rates, particularly for vessels under 6mm in diameter.

2)   **Arterio-Venous Access Grafts (AVGs):** The world is currently facing a huge increase in the number of people with diabetes. For example, in the United Kingdom, since 1996 the number of people diagnosed with diabetes has nearly doubled and diabetes remains the single most common cause of end stage renal disease (Health, 2007). AVGs are mainly used for creating an 'access point' for haemodialysis treatments for patients with renal diseases. The ideal vascular access for patients undergoing haemodialysis is an arterio-venous fistula in the forearm. However, the recent increase in the incidence of diabetes mellitus and the need for haemodialysis in patients with this disorder has expanded the number of patients who require implantation ePTFE graft for vascular access.

Generally, for prosthetic grafts, research is currently being undertaken under two separate strands; the first tends to focus on tissue-engineering and biomaterial science, while the second is concerned with biomechanics, flow field augmentations and haemodynamic forces. The attention of the present chapter is

restricted to the latter and introduces the role of CFD in investigating and designing novel grafts with improved patency rates.

2.7.4 Vascular Graft Failure

Graft failure is currently a major concern for medical practitioners in treating PVD and CAD. For instance, almost 35,000 coronary artery bypass graft (CABG) procedures are performed each year in the UK according to the British Heart Foundation, however, over 50% of CABG fail within 10 years. In 1999, an estimated 688,000 bypass surgeries were performed in the United States but up to 10% of these procedures failed within 30 days of surgery (Ku et al., 2005). Similarly, stenosis at the graft-vein junction caused by IH is the major cause of failure of arterio-venous access grafts used for haemodialysis. For example, in the United States alone there are 175,000 ePTFE grafts used for permanent vascular access, with the 1 and 2-year primary patency rates currently at 50 and 25%, respectively. These low patency rates have limited the use of AVGs and have resulted in arterio-venous fistula in the forearm to remain as an ideal vascular access for patients undergoing haemodialysis.

Early graft failure (within 30 days) is attributable to surgical technical errors (such as choosing a poor location for the distal anastomosis) and resulting thrombosis, while late graft failures are mainly caused by progression of atherosclerosis and intimal hyperplasia (IH) (Bryan and Angelini, 1994; Whittemore et al., 1981).

It is now widely accepted that haemodynamic factors play an important role in the formation and development of IH (Archie et al., 2001; Ghista and Kabinejadian, 2013). The intimal thickening (IT) and restenosis due to IH is normally characterised by unsteady shear stress, recirculation regions, pulsatile stress and graft deformations (Sottiurai et al., 1983). These haemodynamic factors include low and oscillating wall shear stress (WSS) (Ross Ethier et al., 1998), large spatial wall shear stress gradient (WSSG) (DePaola et al., 1992) and long residence time of blood cells (Perktold et al., 1997). Several studies have shown a correlation between the haemodynamic factors and localised sites of intimal

29

thickening, which in a conventional end-to-side (ETS) configuration occur predominantly at the heel and toe of the anastomosis, on the artery floor opposite the anastomosis, and on the suture line (Figure 2.7.4.1). Consequently, much research has been conducted in the past few decades to design grafts that will remain patent for far longer, ideally longer than the life-span of the patient. For example for CABGs, in order to achieve higher patency rates, numerous studies have been conducted in an attempt to improve the haemodynamics at the anastomosis by studying the effects of anastomotic angle, shape of distal anastomosis, out-of-plane graft, graft-to-host artery diameter ratio, competitive flow and distance of grafting (Ghista and Kabinejadian, 2013).
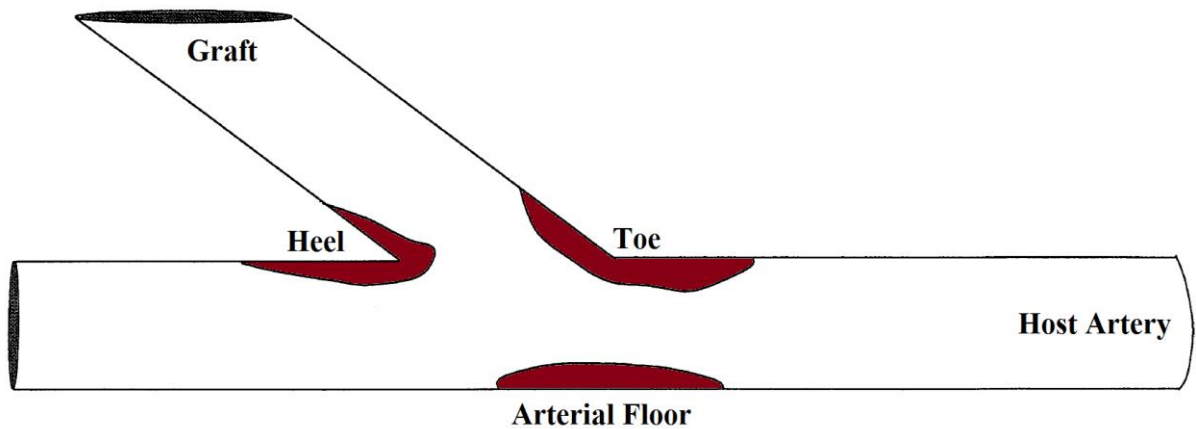
Figure 2.7.4.1- Spatial distribution and localized sites of intimal thickening/intimal hyperplasia in a typical arterial bypass graft.

2.7.5   *Novel Graft Designs*

As was alluded to above, it is now widely accepted that both IH and the acute thrombosis, which are the main causes of arterial bypass graft and arterio-venous graft failures, have close correlations with haemodynamics forces, including low and oscillating wall shear stress. Therefore, designs of new prosthetic grafts have started to take a new direction toward improving the patency of grafts through novel flow field augmentations.

One of the most significant contributions to this field was based on a research which showed that the 'spiral flow' is a natural phenomenon in the whole arterial system (Stonebridge and Brophy, 1991; Stonebridge et al., 1996). The spiral flow in arteries is caused by the rotational compressive pumping of the heart (Jung et al., 2006) and is supported by the tapered, curved and non-planar geometry of the arterial system (Caro et al., 1996; Stonebridge, 2011). In other words, the rotational motion of the blood flow is induced by the twisting of the left ventricle during contraction and then accentuated upon entering the aortic arch (Murphy and Boyle, 2012).

The spiral flow has also been used in many industrial applications, mainly to enhance mixing and turbulence for heat transfer augmentation. For example, as shown in **Error! Reference source not found.**, the fuel pins in the UK' fleet of Advanced Gas-cooled Reactors (AGRs) have been designed to induce helical flow through creating a series of protrusions in the form of spiral ridges on the outer surface of the fuel pins. These configurations have significantly enhanced heat transfer compared to conventional pins. Consequently, biomedical prosthetics could potentially use this concept to modify the haemodynamics forces in the cardiovascular system to mimic the physiological spiral blood flow in arteries and grafts. In fact, two of

(a)   (b)   (c)
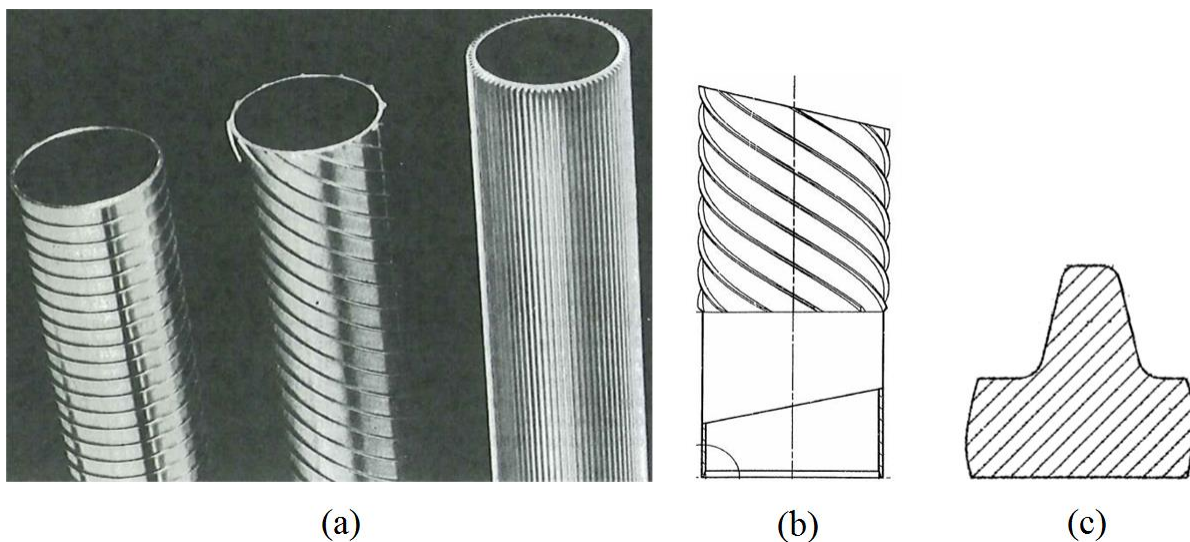
Figure 2.7.5.1- Industrial examples of inducing helical flow; (a) schematics of 'transverse-ribbed', 'multi-start ribbed' and 'longitudinally-finned' fuel pins used in the nuclear fuel pins of the UK's Advanced Gas-Cooled Reactors (AGRs); (b) schematic of the helical ridges on the outer surface of the 'multi-start' fuel pins; (c) the profile of the rib/ridge in the 'multi-start' design.

the most innovative and successful graft designs have used this principal in order to induce spiral flow in arteries. These designs are briefly discussed below:

(i) **'SwirlGraft'** which was developed by Caro and colleagues (Caro et al., 2005) at Veryan Medical Ltd was a new AV shunt graft with a helical out-of-plane geometric feature incorporating 'Small Amplitude Helical Technology' (SMAHT). Compared to a conventional ePTFE graft, the animal experiments reported in (Caro et al., 2005) demonstrated that there was less thrombosis in the SwirlGraft than in the conventional ones. The difference became even more remarkable after 8 weeks of implementation when occlusion occurred in the conventional grafts, while less thrombosis and IH occurred in the SwirlGraft. Recently a few attempts have been made to numerically simulate the blood flow in out-of-plane graft geometries that induce 3D swirling flows (Cookson et al., 2009; Lee et al., 2011; Sun et al., 2010; Zheng et al., 2009) with an aim of understanding the flow physics and improving the current graft designs. In addition, Veryan Medical Ltd has recently designed a peripheral stent known as 'BioMimics 3D Helical Stent' which appears to have evolved from SwirlGraft and SMAHT and is currently under clinical trials. However, there are some concerns associated with both SwirlGraft and 3D helical stent such as an increase in the pressure drop across the helical segment. The helical stent can also impose a severe geometric change on an artery causing damage to the arterial wall. The details of this design and its results are beyond the scope of this chapter and therefore will not be discussed any further.

(ii)   **'Spiral Flow Peripheral Vascular Graft'** which was introduced by Vascular Flow Technologies (VFT) Ltd consists of a prosthetic ePTFE graft design that is engineered to induce spiral flow through an internal ridge within its distal end. This design is primarily based on research carried out by Stonebridge and colleagues at Ninewells Hospital in Dundee, Scotland into the naturally occurring helical flow found in studies of the cardiovascular system using Doppler ultrasound. The results of an early clinical non-randomised study for VFT peripheral bypass graft are promising and show primary patency rates of 81% for above-the-knee bypasses and 57.3% for below-the-knee bypasses at 30 months of follow-up. The respective secondary patency rates were 81% and 64% (Stonebridge et al., 2012). In an unpublished research, similar improvements were also found when using the spiral flow graft for AV access for haemodialysis ('Spiral Flow AV Access Graft'). While these initial results highlight the potential for the idea of spiral-induced grafts in bypass surgeries, it has a number of limitations. For instance this design cannot currently be used for CABG since satisfactory prosthetic grafts have shown to be unsuccessful for small calibre applications due to their poor long-term patency rates (Yellin et al., 1991) (i.e. autologous internal thoracic arteries, radial arteries and saphenous veins still remain the most widely used conduits for CABG (Angelini and Newby, 1989; Cameron et al., 1996; Desai et al., 2011)). Another disadvantage of this type of prosthetic graft is associated with its limitation to ePTFE, which has shown to have poor patency rates due to poor mechanical characteristics (i.e. low compliance) and the lack of endothelial cells (ECs) lining the lumen (Salacinski et al., 2001).

While the physiological importance of secondary motion in circulation has clearly been highlighted in the literature (Stonebridge and Brophy, 1991; Stonebridge et al., 1996), the benefits of helical/spiral prostheses in vascular conduits have yet to be firmly established. Moreover, the range of possible design configurations is large and the effects of different design/geometrical parameters on haemodynamics forces are still not clear. Therefore, there is a scope to investigate existing and innovative flow field

augmentations using computational techniques to inform potential designs of novel prostheses and surgical vascular reconstructions.

2.7.6 *Haemodynamic Metrics*

One of the main attractions of using CFD in biomedical problems is its ability to calculate several different haemodynamic parameters/metrics, which could potentially have important clinical implications. For example, previous studies have shown that:

(i)   localised distribution of low Wall Shear Stress (WSS) and high-Oscillatory Shear Index (OSI) strongly correlates with the focal locations of atheroma (He and Ku, 1996),

(ii)   large spatial WSS Gradient (WSSG) contributes to the elevated wall permeability and atherosclerotic lesions (DePaola et al., 1992),

(iii)   combination of high-shear stress and large exposure times may induce platelet activation (Hellums, 1993; Ramstack et al., 1979; Wurzinger et al., 1985, 1986), and

(iv)   stagnant and recirculation flow regions can cause platelet aggregation and thrombogenesis.

The above haemodynamic parameters can be directly derived from the flow fields obtained by CFD-based simulation tools. It is worth noting that the reason for having to define different metrics for the variation in blood flow characteristics is mainly due to anatomic and physiologic variations and system complexity of the fluid flow as well as its interaction with the vessel wall and tissue. In addition, single-feature-haemodynamic metrics are generally unable to capture the multi-directionality of the flow field (Peiffer et al., 2013), hence, having to define different parameters.

In this chapter, the distributions of haemodynamic parameters, including Time-Averaged WSS (TAWSS), TAWSSG (Buchanan et al., 2003), OSI (He and Ku, 1996) and Relative Residence Time (RRT) (Lee et al., 2009) are calculated for one study below, according to the following equations:

$$TAWSS = \frac{1}{T}\int_0^T \left|\vec{\tau}_w\right| dt \tag{2.7.6.1}$$

34

$$TAWSSG = \frac{1}{T}\int_0^T \sqrt{\left(\frac{\partial \tau_x}{\partial x}\right)^2 + \left(\frac{\partial \tau_y}{\partial y}\right)^2 + \left(\frac{\partial \tau_z}{\partial z}\right)^2}\, dt \qquad (2.7.6.2)$$

$$OSI = \frac{1}{2}\left(1 - \frac{\left|\int_0^T \vec{\tau}_W\, dt\right|}{\int_0^T |\vec{\tau}_W|\, dt}\right) \qquad (2.7.6.3)$$

$$RRT = \frac{1}{(1 - 2 \times OSI) \times TAWSS} = \frac{1}{\frac{1}{T}\left|\int_0^T \vec{\tau}_W\, dt\right|} \qquad (2.7.6.4)$$

In the above equations, $\vec{\tau}_W$ is the WSS vector and T is the time period of the flow cycle.

2.7.7   Haemodynamics of Spiral and Helical Grafts

The main configuration studied in this section represents a typical ETS distal graft anastomosis, which can be found in the following three graft configurations: 1) Peripheral Artery Bypass Graft, 2) Coronary Artery Bypass Graft and 3) Arterio-Venous Access Graft. The former has been selected for the present work since both of the novel flow field augmentation designs discussed earlier, have only been tested for the peripheral artery bypass configuration.

It is important to note that while some resemblances can be found amongst the above three ETS graft configurations, the haemodynamic pattern and consequent location of IH formation are different. For instance, the blood flow rate in arterio-venous grafts is about 5-10 times higher than that in peripheral or coronary artery bypass grafts; consequently the spatial distribution of IH is different in each configuration (Haruguchi and Teraoka, 2003).

The dimensions and the schematics of the models tested here are given in **Error! Reference source not found.**. A brief description of each model is as follows:

- **Model 1 (Control Graft):** This model represents a baseline and a conventional ETS distal graft anastomosis for a peripheral artery bypass configuration.

35

- **Model 2 (Spiral Graft):** This model has an internal spiral inducer within the distal end of the graft in the form of an internal ridge. The ridge, which is one pitch long, provides ridged cross-sectional geometry to engender and deliver a single-spiral flow pattern.

- **Model 3 (Helical Graft):** The distal end of the bypass graft in this model consists of a small amplitude out-of-plane (non-planar) helical configuration. The helical section of this model involves a one-turn helix with pitch and amplitude approximately $14D$ and $0.5D$, respectively (where D is the internal diameter of the graft).

- **Model 4 (Helical+Spiral Graft):** The distal end of the bypass graft in this model combines the geometrical features present in both models 2 and 3. Note that in this model the out-of-plane helical and the internal ridge have the same pitch and turn in the same direction.
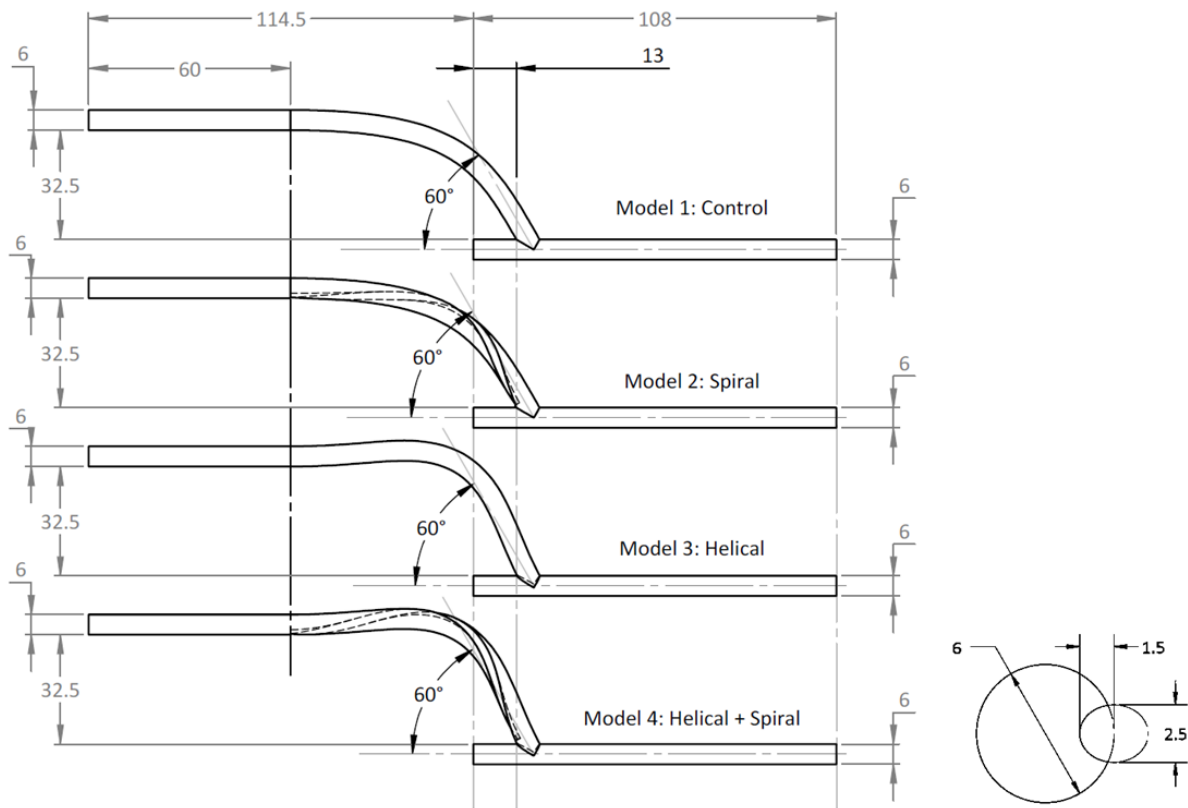
Figure 2.7.7.1- Schematics and the dimensions of the present four geometric models.
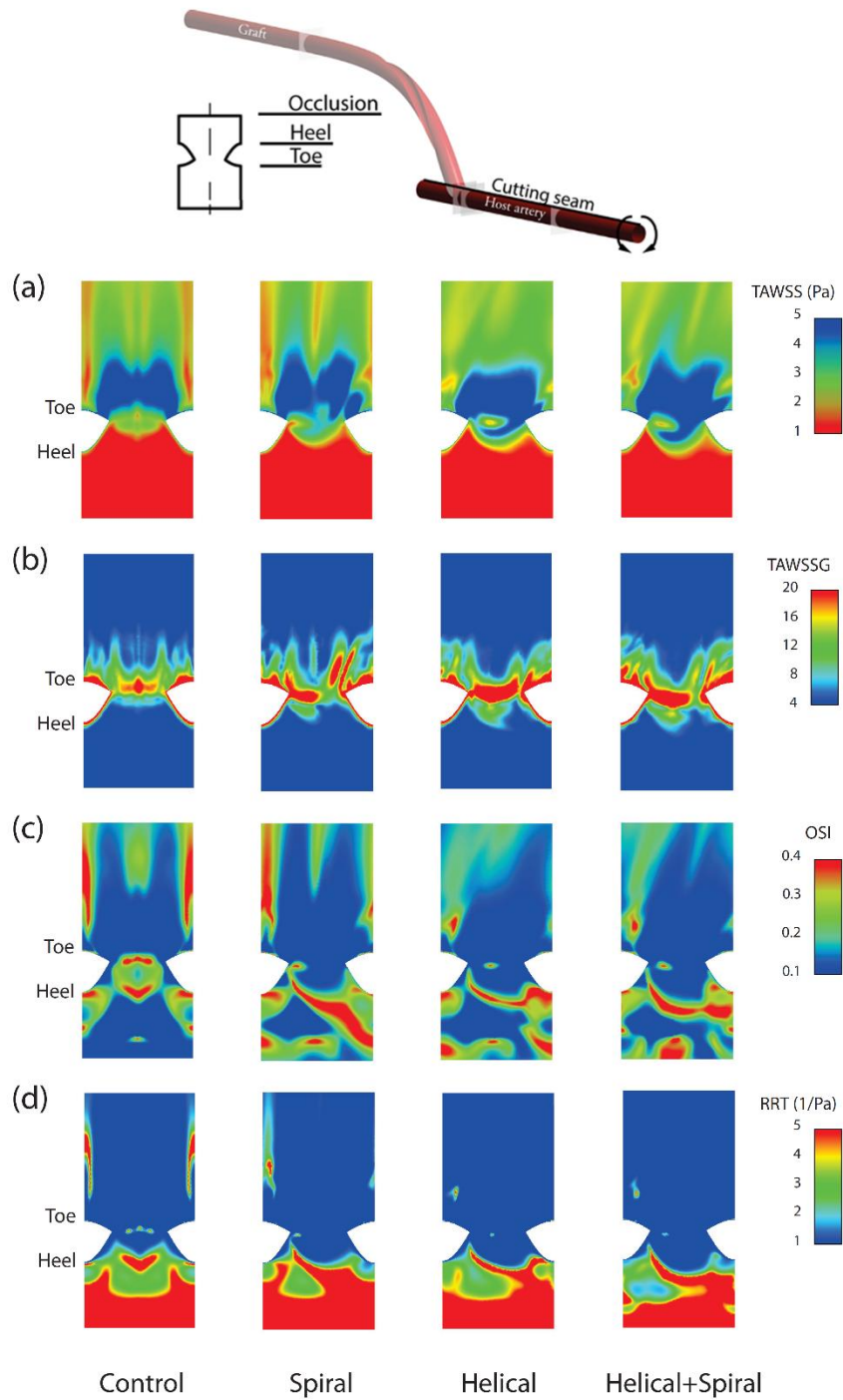
Figure 2.7.7.2- Distributions of different haemodynamic parameters viewed from the host arterial

wall, opened ventrally and shown *en face*: (a) Time-Averaged Wall Shear Stress (TAWSS); (b) Time-

Averaged Wall Shear Stress Gradient (TAWSSG); (c) Oscillatory Shear Index (OSI); and (d) Relative Residence Time (RRT). Note that the colour scale of the TAWSS map is inverted for ease of comparison.

Error! Reference source not found.2.7.7.2 shows the distribution of the above metrics for all the four geometrical models displayed on an unfolded model of the host artery, which has been opened ventrally. The maps shown in **Error! Reference source not found.** should be interpreted so that the vertical axis represents distance along the host artery (with blood flow from bottom to top) and the horizontal axis represents the circumferential distance along the wall of the host vessel (the bed region appears at the centre).

Investigation of the haemodynamic parameters distribution in 2.7.7.2 shows that the TAWSS increases on the arterial bed and around the anastomosis by adding the non-planar helicity (while the effect of including the spiral ridge was minimal). There are indications that the blood monocytes are more likely to adhere to the endothelial layer at regions with low-TAWSS (Pritchard et al., 1995); hence, introducing the non-planar curvature to the graft may reduce the spatial extent of early wall lesion. Also, significant correlations have been reported between the preferred sites of IT and the regions of low-WSS (Sunamura et al., 2007; White et al., 1993); as such the observed altered flow patterns may be perceived as a beneficial feature of the helical grafts which may positively impact the graft patency rate.

It was also found that the elevated OSI region on the host arterial wall (distal to the toe) reduces in size considerably in helical graft models (i.e., Models 3 and 4) and moderately in the spiral graft model (i.e., Model 2). Hence, a low-TAWSS/high-OSI region in the control model is replaced by a high-TAWSS/low-OSI area in the helical graft models. This is another positive feature of introducing the non-planar helicity (and to a lesser extent the inclusion of the spiral ridge) to the bypass grafts, since the combination of high-TAWSS and low-OSI is believed to be contributing to IT and atherosclerosis development as well as increasing the risk of the aggregation of red blood cells (He and Ku, 1996; Ku et al., 1985; Malek et al., 1999).

In addition, the swirling flow induced by the helical graft in Models 3 and 4 reduces the RRT distal to the toe of the anastomosis, by eliminating the flow separation in this region (which was present in Model 1 and to a lesser extent in Model 2). This could reduce the chance of platelet aggregation and thrombus formation (Hellums, 1993), and consequently enhances the patency of the bypass graft.

2.8   SUMMARY AND CONCLUSION

As observed in this chapter, cardiovascular biomechanics and mechanobiology is a pivotal research area for the improvement of existing therapeutic strategies for CVD or new therapeutics development. For example, inducing swirling flow into the bypass grafts can bring about positive flow features and more favourable distribution of haemodynamic parameters in the graft, anastomotic region, and the host artery, which may enhance the patency and longevity of the bypass graft. For this purpose, graft helicity was found to be significantly more effective than a spiral ridge. Also, it was found that a combination of graft helicity and spiral ridge can further enhance this swirling effect on the flow. However, in order to optimize these features for their utility in different types of bypass grafts, further studies are warranted. Equally important to future parametric improvement is more realistic models of the vessel wall. Instead of treating the wall as a non-linear orthotropic elastic cylindrical membrane for CFD analysis, the experimentally observed material damping (elastic) properties or the viscoelastic properties of the wall tissues should be incorporated in the analysis to reflect more realistic flow environments in vivo and thus more accurate prediction of cell and tissue responses based on the existing knowledge about cell mechanobiology of flow. Using models considering the fluid-structure interaction, analytical expressions for the displacement and shear stresses developed in the wall as well as the velocity distribution, fluid acceleration and volume flow rate of blood can be derived computationally.

In summary, future vascular mechanobiology studies will greatly benefit from highly integrated approaches using computational analysis together with *in vitro* and *in vivo* measures as well as benchtop

flow models containing vascular cells for the explorations of mechano-sensing and mechano-transduction mechanisms.

3 High Pulsatility Flow Promotes Vascular Fibrosis by Triggering Endothelial EndMT and Fibroblast Activation[1]

Winston H. Elliott[1], Yan Tan[1], Min Li[2], Wei Tan[1,2] *

[1] Department of Mechanical Engineering, University of Colorado at Boulder, Boulder, CO 80309

[2] Department of Pediatrics, University of Colorado at Denver, Aurora, CO 80045

* Corresponding Author

Abbreviations, symbols, and terminology:

EndMT – Endothelial-to-mesenchymal transdifferentiation

HPF – High pulsatility flow

EC – Endothelial cell

SMC – Smooth muscle cell

AdvFB – Adventitial fibroblast

HPAEC – Human pulmonary arterial ECs

PI – Pulsatility index

TGF-β – Transforming growth factor β

ABSTRACT

Vascular fibrosis, the formation of excess fibrous tissue on the blood vessel wall, is characterized by unmitigated proliferation of fibroblasts or myofibroblast-like cells exhibiting α-smooth-muscle-actin in vessel lumen and other vascular layers. It likely contributes to vascular unresponsiveness to conventional therapies. This paper demonstrates a new flow-induced vascular fibrosis mechanism. Using our developed flow system which simulates the effect of vessel stiffening and generates unidirectional high pulsatility flow (HPF) with the mean shear flow at a physiological level, we have shown that HPF caused vascular endothelial dysfunction. Herein, we further explored the role of HPF in vascular fibrosis through endothelial-to-mesenchymal transdifferentiation (EndMT). Pulmonary arterial endothelial cells were exposed to steady flow and HPF, which have the same physiological mean fluid shear but different in flow pulsatility. Cells were analyzed after being conditioned with flows for 24 hr or 48 hr. HPF was found to induce EndMT of cells after 48 hr stimulation; cells demonstrated drastically decreased expression in endothelial cell marker CD31, as well as increased transforming growth factor β, α-SMA, and collagen type-I, in both gene and protein expression profiles. Using the flow media from HPF-conditioned endothelial culture to cultivate arterial adventitial fibroblasts and endothelial cells respectively, we found that the conditioned media respectively enhanced migration, proliferation and α-SMA expression of adventitial fibroblasts, and induced EndMT of endothelial cells. It was further revealed that cells exposed to HPF exhibited much higher percentage of caspase-positive cells compared to those exposed to steady flow. Apoptotic cells together with remaining, caspase-negative cells suggested the presence of apoptosis-resistant dysfunctional endothelial cells which likely underwent EndMT process and perpetuated fibrosis throughout vascular tissues. Therefore, our results indicate that prolonged HPF stimuli induce vascular fibrosis through triggering EndMT and EC-mediated AdvFB activation and migration, which follows initial endothelial inflammation, dysfunction and apoptosis.

Key Terms: vascular fibrosis, endothelial cell, mechano-transduction, high pulsatility flow, endothelial-to-mesenchymal transition.

3.1 Introduction

Tissue fibrosis is the formation of excess fibrous <u>connective tissue,</u> due to increased activities of fibroblast-like cells in a reparative or reactive process. It is often preceded by tissue inflammation and resulting in increased content of collagen type I to improve structural integrity of injured or weak tissues. As a consequence of fibrosis, collagen-rich scar tissues accumulated with fibroblast- or myofibroblast-like cells replace normal functional tissues. Therefore, fibrosis is common in a number of diseases showing gradual tissue deterioration, as in the case of vascular tissue fibrosis, which is an important aspect of extracellular matrix remodeling in hypertension and other cardiovascular diseases. The exact cell type contributing to vascular fibrosis during blood vessel remodeling after injury is unclear. Evidence shows fibrosis may occur in all vascular tissue layers, namely intima, media and adventitial layers, as occurring in atherosclerosis, pulmonary artery hypertension, vascular grafting anastomose or stenting. Vascular fibrosis likely involves all resident vascular cell types, endothelial cell (EC), smooth muscle cell (SMC) and adventitial fibroblast (AdvFB). (Arciniegas et al., 1992, 1992; Berard et al., 2013; Frid, 2002; Li et al., 2007; Owens, 2010; Rekhter et al., 1993; Sakao et al., 2005) Understanding of vascular fibrosis pathologies are further complicated by all cells within vessel walls presenting α-smooth muscle actin (α-SMA), (Frid, 2002; Varcoe et al., 2006) most commonly associated with SMC previously. Studies also suggested that these α-SMA^{+} cells might be associated with the presence of transforming growth factor β (TGF-β). (Suwanabol et al., 2012; Tsai et al., 2009) Though the majority of previous studies have focused on illustrating the role of SMCs in vascular neointimal hyperplasia and fibrosis, evidence from recent studies supports the potential trans-differentiation of other vascular cells (ECs and AdvFBs) into the myofibroblast phenotype during pathological vascular remodeling (Sakao et al., 2007), but the underlying mechanism, particularly in relation to hemodynamics present in vascular diseases, has been seldom explored.

Increasing attention is now given to endothelial-to-mesenchymal transition (EndMT) and to its occurrence and roles in artery maturation during embryonic development as well as in intimal fibrosis during vascular remodeling. (Arciniegas et al., 2000; Egorova et al., 2011a, 2012b; Nakajima et al., 2000) EndMT is believed to contribute, at least partially, to pulmonary, renal, and cardiac fibrosis in adult mammals. (Hashimoto et al., 2010; Zeisberg et al., 2007b, 2007a, 2008) Activation of EndMT can result from biomechanical and/or biochemical signaling. It was shown increasing the mean magnitude of shear stresses from 0.5 to 5.0 Pa promoted murine and chicken embryonic ECs to the EndMT process, showing reduced endothelial marker and increased α-SMA expression. (Egorova et al., 2011b, 2011a) While flow-induced EndMT was thought to be a necessary step during vascular development, it may be harmful to healthy blood vessels. Recent findings have highlighted the contribution of EndMT to vascular pathogenesis in a number of fibrotic diseases. (Hashimoto et al., 2010; Maddaluno et al., 2013; Zeisberg et al., 2007a, 2008) The EndMT process is particularly correlated to the presence of TGF-β. (Arciniegas et al., 1992; Hashimoto et al., 2010; Imamura et al., 2010; Kokudo et al., 2008; Medici et al., 2011; Zeisberg et al., 2007b, 2008) In addition to EndMT, activation of AdvFB migration, proliferation or matrix production may also contribute to vascular fibrosis, hardening and reduced response to vasodilation therapy. Activation of AdvFB can be triggered by flow and/or cytokine stimuli. High interstitial flow was shown to activate AdvFB migration. (Acharya et al., 2008; Battegay et al., 1990; Garanich et al., 2007) TGF-β was also found to be involved in activating AdvFB proliferation and matrix production. (Khalil et al., 2005) Though the respective contributions of EC and AdvFB to vascular fibrosis during remodeling are increasingly recognized, few studies have examined their collaborative efforts in driving the fibrotic process. Understanding the cellular mechanisms during vascular fibrosis and hardening could greatly assist the development of new therapeutic approaches towards cardiovascular disease and hypertension.

Our previous studies have established unidirectional high pulsatility flow (HPF), a proximal stiffening-induced flow condition indicated in disease and aging,(Mitchell et al., 2011; Panaritis et al.,

2005) as a determinant to distal pulmonary artery endothelial health.(Li et al., 2009) We have shown that HPF altered pulmonary artery SMC physiology via vasoactive substances and cytokines produced by the endothelium. (Scott et al., 2013) In response to HPF with physiologic, mean shear stresses (1.2 Pa), distal ECs also demonstrated acute inflammatory response, simulating that occurring in pulmonary hypertension. Growing evidence supports that vascular intimal thickening of distal pulmonary arteries in diseased condition, due to inflammation or fibrosis, might contribute to the unresponsiveness of arteries to vasodilation therapies. (Gan et al., 2007; Pries et al., 2005) Palevsky *et al.* showed that an intimal area of more than 18% of the vascular cross-section had an 85% predictive value for identifying poor outcome from vasodilation treatment. (Palevsky et al., 1989) It is well known that during wound healing, fibrosis follows inflammatory events. This might occur during flow-induced vascular inflammation and remodeling. To further establish the role of HPF (with the mean flow shear at a physiological level) in fibrosis of vascular intima and other vascular layers, we therefore sought to test the hypothesis that prolonged HPF stimuli induce vascular fibrosis through triggering EndMT and EC-mediated AdvFB activation and migration, following initial endothelial inflammation. To address this hypothesis, we applied our developed flow system, simulating the effects of vessel stiffening, and HPF generation on the downstream cells.

3.2   Materials and Methods

3.2.1   Cell Culture

Human pulmonary arterial ECs (HPAEC) were obtained from Lonza Inc, and kept in a CO_2 incubator at 37°C and 5% CO_2. Cells were thawed as needed and grown to approximately 70-80% confluency using EGM-2 with additional growth factor and fetal bovine serum bullet kit (Lonza, Basel, Switzerland). Once confluent, cells at passages of 3-8 were seeded on two glass slides for the flow experiment. Human pulmonary artery adventitial fibroblasts were maintained in DMEM media containing 10% FBS and cultured in similar conditions.

3.2.2   Flow Setup and Experiments

To examine the response of HPAECs to various flow conditions, plain microscope glass slides were chemically functionalized with 20% of aqueous sulfuric acid and then coated with 6% of 3-aminopropyltriethoxysilane in acetone. After silanization, the glass slides were treated with 1.5% of glutaraldehyde solution. This formed an aldehyde which could initiate amine linkage to protein coating. The slides were then coated with 25 µg/ml fibronectin aqueous solution for 30-60min to provide a functional attachment layer for the HPAECs. HPAECs at a concentration of 6.0×10^5 per ml were seeded on the fibronectin-coated slides and given one hour to attach to the slides, and then the cells were covered in growth media and allowed to reach confluency, before they were transferred to the flow chamber apparatus.

To ensure the sterility and cleanness of the flow experiments, the exterior of a pulsatile blood pump (Harvard Apparatus Inc; Holliston, MA) or a peristaltic pump (Cole Parmer), which was used to circulate the medium, was sterilized by wiping it with 70% ethanol. Sterilization of the flow circuit was completed through perfusing all the tubings, pump chamber and connectors with 10% hydrogen peroxide (H_2O_2) under ultraviolet light within a biosafety cabinet Type II for a minimum of 30 minutes. To clean the circuit of any cytotoxicity, sterile Dulbecco's phosphate buffered solution (DPBS) was circulated through and removed. Perfusion with DPBS was repeated twice before flow experiments started. For generating

HPF condition, the blood pump simulated the heart function generating cardiac output, while the compliance-adjustment chamber simulated the flow buffering or cushion function of proximal arteries. The fluid levels of the compliance-adjustment chamber allowed for pulsatility control of dynamic flows, with lower fluid levels allowing greater dampening of dynamic pressures. Downstream to the compliance-adjustment chamber was the cell-plate flow chamber which holds the endothelium representing the distal pulmonary artery endothelium. Each component was connected by stiff polystyrene tubing. The circulating media used in the experiments consisted of a basal media (EBM-2, Lonza, Basel, Switzerland), medical grade dextran (MP-products Inc, Solon, OH) (7% w/w), and penicillin/streptomycin (2% v/v), as its viscosity was close to blood viscosity so that it reduces volumetric flow rate while maintaining a high shear stress. For flow measurements, a digital flow meter (Alicat Scientific Inc, Tucson, AZ) was placed before the flow chamber. A manifold section was used to run parallel studies.

Two flow conditions were applied within a closed fluid circuit: high pulsatility flow (HPF) using the blood pump and steady flow using peristaltic pump. Both pulsatile flows had the same mean flow rate with a mean surface flow shear stress of 1.2 Pa, at the frequency of 1 Hz. The steady flow showed no great variation in flow velocity with the flow pulsatility index (PI) less than 0.2, while the PI value of HPF was determined to be 1.7,(Mitchell et al., 2011; Panaritis et al., 2005) using the following equation:

$$\text{The pulsatility index (PI)} = \frac{\Delta Flow\ Velocity}{Average\ Flow}$$

For all the experiments, cells were preconditioned at low or no pulsatility ($PI < 0.5$) with low shear stress for between 4-6 hr before experimental flow conditions began. Experiments consisted of 24 hr and 48 hr of flow conditions. For the pharmacological treatment of cells using taxol (Paclitaxel, Sigma-Aldrich Inc), the experiments were performed with the addition of 10 ng/ml of taxol in the flow culture media. HPAECs grown in the absence of flow (the static condition) were used as a control. After

HPAECs were exposed to different flows, they were collected and analyzed for gene expression using real-time PCR and for protein expression using western blotting. The circulating media during flow culture period were collected as flow conditioned media (FCM) for studies that evaluate EC and AdvFB activation, in which confluent HPAECs and AdvFBs were cultured for 24 hr in FCM. Western blot analysis was performed on resulting cells, comparing α-SMA protein expression with β-actin. FCM was also used to evaluate its potential to induce AdvFB migration and proliferation.

3.2.3   Western Blot

Western blot analyses were performed as per the manufacturer's suggestions (Invitrogen, Carlsbad, CA). Briefly, to retrieve proteins, ECs were gently scraped off glass slides, lysed with RIPA lysis buffer, and then centrifuged at 14,000 rpm for 20 min at 4°C. Supernatant was then transferred to a clean tube. Protein concentrations were determined using a standard curve of BSA. Twenty micrograms of protein from each sample were separately loaded and subjected to gel electrophoresis. Following electrophoresis, resulting protein was transferred to a nitrocellulose membrane. The membrane was blot with COL1A1 rabbit polyclonal antibody, PECAM-1 mouse monoclonal, TGFβ1 mouse monoclonal, and 1A4 (α-SMA) antibodies (all antibodies from Santa Cruz Biotech, Santa Cruz, CA).

3.2.4   Real-Time PCR

To study the effects of HPF on the pulmonary artery endothelium, HPAECs were conditioned with HPF and steady flow for 24 hr and 48 hr, respectively. Real-time PCR was used to analyze the gene expression of the biomarkers important for EndMT.

Cell samples were gently scraped from slides after applying RLT buffer tissue lyser using the RNeasy mini-kit from Qiagen (QIAGEN, Hilden, Germany), according to the manufacturer's instructions. Samples were then prepared as per manufacturer's instructions for real time- PCR using RT^2 SYBR Green FAST Mastermix and corresponding gene primers, also from QIAGEN. Gene expression in 24 and

48-hr flow cycles were examined for PECAM-1 (CD31), α-SMA (ACTA2), TGF-β (TGF-beta1), and Collagen-I (COL1A1) with β-actin expression (ACTB) as the housekeeping gene. Primers (PPH01362E, PPH00508A, PPH01299F and PPH01300B) were directly obtained from Qiagen Inc. Data was analyzed using the $\Delta\Delta C_T$ method, and plotted. Statistical significance between groups was found using Welch's t-test using degrees of freedom derived from the Welch-Satterthwaite equation for unequal sample sizes and unequal variances.

3.2.5   Fibroblast Migration and Proliferation Assay

The flow conditioned media (FCM) from HPAECs were taken from those exposed to steady or HPF culture conditions for 24 hr or 48 hr, and were used to determine migration and proliferation of AdvFB. For cell migration study, the FCM was placed in the bottom well covered with a 3-mm transwell insert (BD Biosciences, San Jose, CA), while AdvFBs were placed on top of the insert and cultured for 24 hr. Subsequently, the cells on the top of the insert were gently scraped off with a cotton tip, and the cells on the other side of the insert were stained with 2% crystal violet or DAPI, and then imaged under a light microscope. The number of migrated cells was determined using ImageJ (National Institute of Health, Bethesda, MD).

For measurement of fibroblast proliferation, FCM was used to culture adventitial fibroblasts for 24 hr. Then, CyQuant proliferation assay kit (Invitrogen, Grand Island, NY) was used according to the manufacturer's instruction. Proliferation of AFB was measured using a CyQuant proliferation assay kit (Invitrogen, Grand Island, NY). Cells were cultured in FCM for 24 hr, and the assay was completed as per manufacturer's instructions.

3.2.6   Apoptosis Assay

Previous studies have shown that EC released TGF-β1 during EC apoptosis. (Cucina et al., 1998; Ten Dijke et al., 2012) These in conjunction with our findings that show ECs exposed to HPF continuously

produce TGF-β1 which further induce EC transition to mesenchymal fibroblastic phenotype and enhance AdvFB activities, suggest that ECs might show enhanced apoptotic activity prior to the EndMT process, releasing TGF-β1 for autocrine and paracrine signaling towards fibrosis. Apoptosis assay was applied to cells after exposure to flow for 24 hr. FLICA poly caspase reagent (Immunochemistry Technology LLC, Bloomington, MN) including fluorescent-labeled inhibitor of caspases, is a simple yet accurate method to measure apoptosis via caspase activity in whole cells. The assay was performed by following the manufacturer's instruction.

3.2.7   *Data Analysis*

All data are expressed as mean ± SEM, and the number of sample studied (n) is ≥3. One-Way ANOVA was used to determine effects of flow pulsatility on gene expression. If significantly difference exists, Student's t-test for one-to-one comparison and Tukey for post-hoc analysis were used to compare means of each individual group. A P value < 0.05 was considered significantly different.

3.3   Results

3.3.1   *HPF induced EndMT after 48 hr stimulation*

Our previous studies have shown that HPF changes vasoactive and proinflammatory activities of bovine PAECs. (Scott et al., 2013) Similar to the responses of bovine cells to HPF, HPAECs produced pro-vasoconstriction and pro-inflammation factors after exposure to HPF. We further asked whether HPAECs would resolve acute inflammation and vasoconstrictive response by making the phenotypic transition to a mesenchymal phenotype. As shown in Figure 3.3.1.1A, results demonstrated that HPF significantly increased HPAEC mRNA expression of α-SMA, TGF-β_1, and COL1A1 molecules by 4-20 folds, when compared to steady flow after 48 hr of flow condition, while no significant difference in all these mRNAs were found between cells under HPF and steady flow after 24 hr of flow condition. Also, HPF enhanced cell mRNA expression of these EndMT markers after cells were exposed to the flow for a longer period of time (48 hr vs 24 hr), whereas steady flow reduced cell expression of these mRNAs over the time, which, except COL1A1, showed no significant difference from the static condition after 48 hr. On the other side, HPAEC exposure to HPF for 48 hr significantly reduced mRNA expression of EC marker, PECAM-1, exhibiting up to 148-fold decrease when compared to the steady flow or static conditions (Figure 3.3.1.1B). Comparison to static control provided baseline EC response to fluid shear within the study, and reinforced steady flow as relevant model for comparison to HPF. These results indicate that EndMT occurs in the endothelial cells exposed to the HPF condition after 48 hr, a relatively longer period of time than that needed to induce pro-inflammatory responses (6-24 hr).
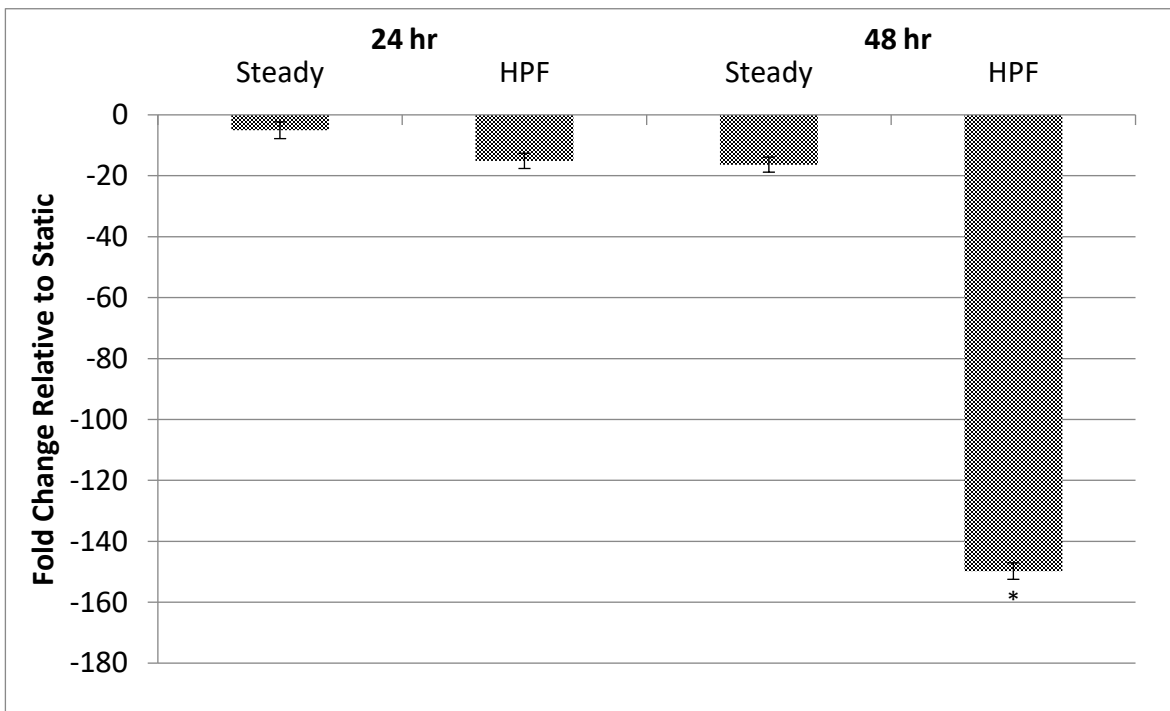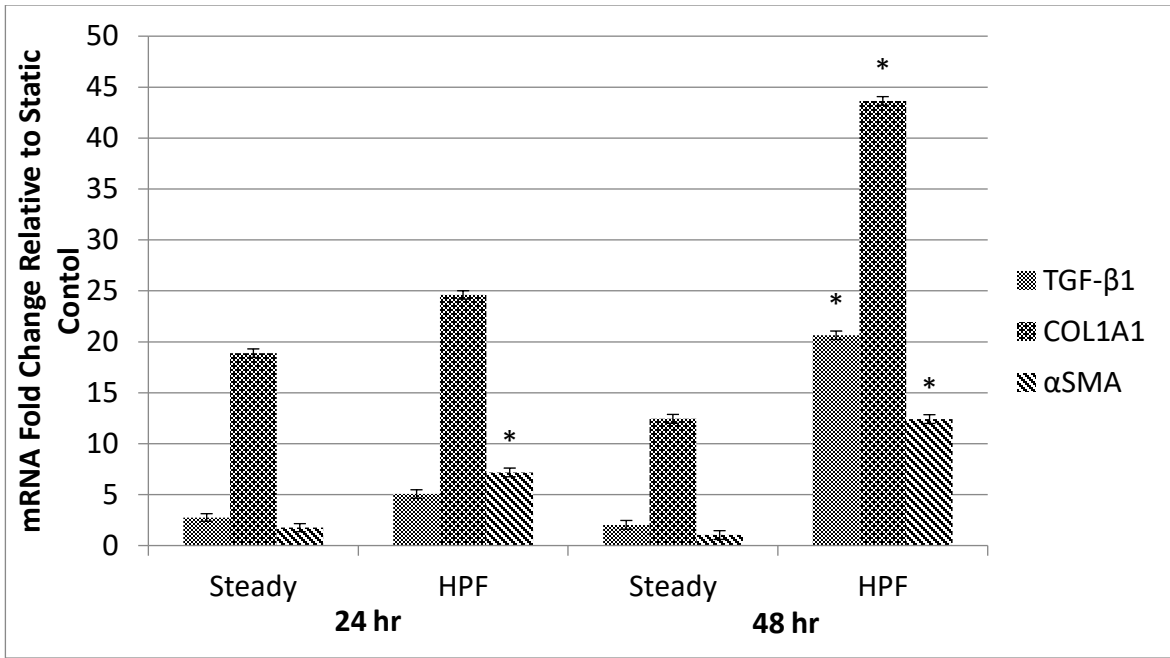
Figure 3.3.1.1- Gene expression results showing that ECs after 48 hr HPF stimulation undergo the EndMT process. (A) The EC expression of αSMA, COL1A1 (for collagen type I) and TGF-β1 mRNAs after 24 hr or 48 hr under steady flow or HPF, using the static condition for comparison. Compared to those exposed to the steady flow, cells after 48 hr of HPF stimulation showed significantly higher levels in all of

these mesenchymal phenotypic genes while cells after 24 hr of HPF stimulation only showed significantly higher expression in α-SMA mRNA. The ΔΔCT method was used to determine the gene expression. (B) The mRNA expression of endothelial marker, platelet endothelial cell adhesion molecule (PECAM-1), in ECs after flow stimulation. Compared to those under steady flow, the cells under HPF for 48 hr showed significantly reduced PECAM-1 mRNA expression, indicating a reduction in EC phenotype; the cells under HPF for 24 hr did not show different PECAM-1 expression when compared to those under steady flow. These results suggest that HPF promoted the mesenchymal transition of ECs after stimulation for a longer time period (48 hr). Statistical analysis using ANOVA and Welch's two-tailed t-test: "*"indicates $p < 0.05$ versus the steady flow after flow stimulation for the same period of time.

To confirm the findings from gene expression, protein analyses were performed on selected molecular markers. Results from western blots support the PCR results. As shown in Figure 3.3.1.2, when compared to the cells under steady flow for 48 hr, ECs under the HPF condition for the same duration increased the protein expression of α-SMA, TGF-β_1, and COL1A1, by 191%, 33%, and 25%, respectively, while these HPF-stimulated ECs exhibited 42.8% reduction in PECAM-1 protein expression.
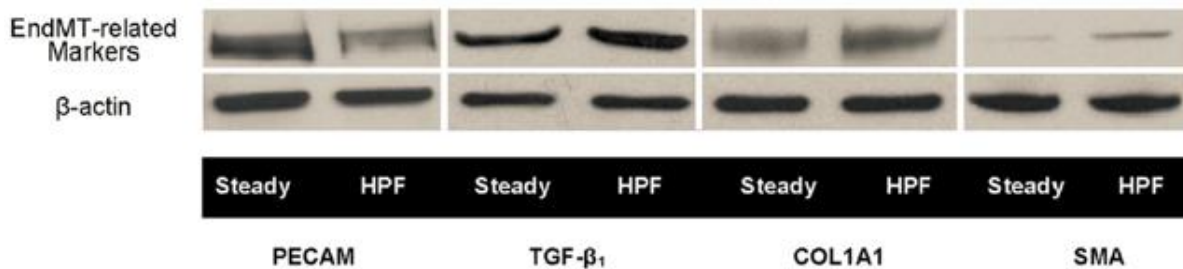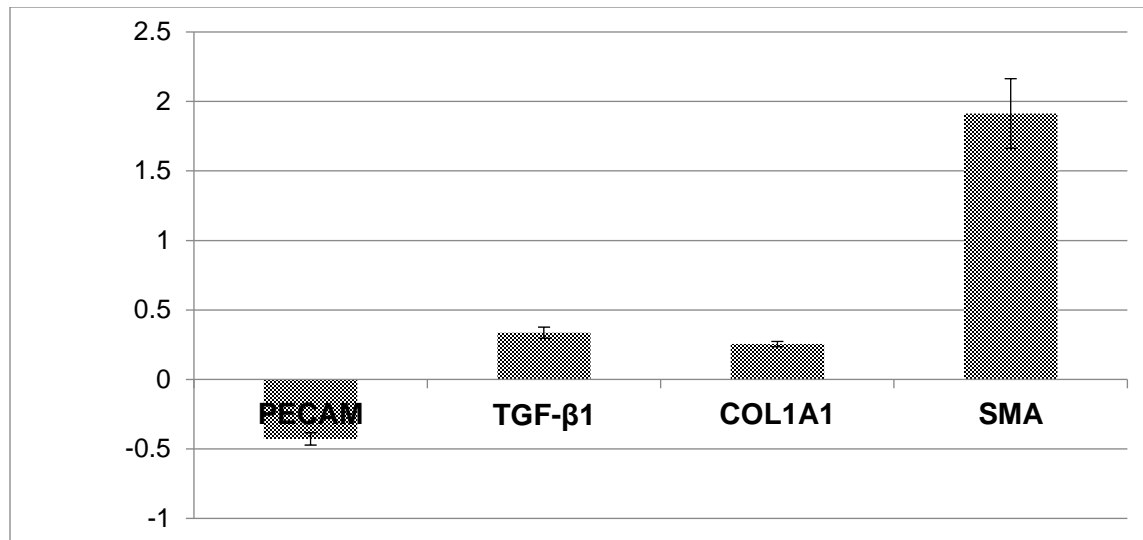
Figure 3.3.1.2- Results from western blotting assays show the EndMT-related markers expressed by ECs after 48 hr of flow stimulation. Compared to the steady flow condition, HPF significantly downregulated EC marker PECAM while it upregulated all the mesenchymal phenotype markers, which demonstrates the change of ECs under HPF from the endothelial phenotype to the mesenchymal, myofibroblast-like phenotype. Quantitative measures of protein expression increase and representative western blotting bands are shown. Statistical significance ($p < 0.05$) was found in all the protein expression comparisons between the steady flow and the HPF.

3.3.2 Flow-conditioned media from ECs under HPF induced EndMT of HPAEC and activated migration and proliferation of AdvEC

As we found that HPF promoted EC production of TGF- β_1, we further asked whether TGF- β_1 and other cytokines produced by the cells remain active in the flow conditioned media (FCM) and sufficient to affect neighboring ECs or AdvFBs. To address this question, FCM were collected after 24 hr or 48 hr flow experiments and were used to culture normal HPAEC and AdvFB, respectively. As shown in Figure 3.3.2.1, results demonstrated that FCM taken from the EC culture stimulated by the HPF condition for 48 hr significantly increased α-SMA protein expression in both AdvFB and EC, when compared to all the other FCM conditions. This suggests the cytokines secreted by HPAECs under HPF could sustain continuous trans-differentiation of ECs and activation of AdvFBs.
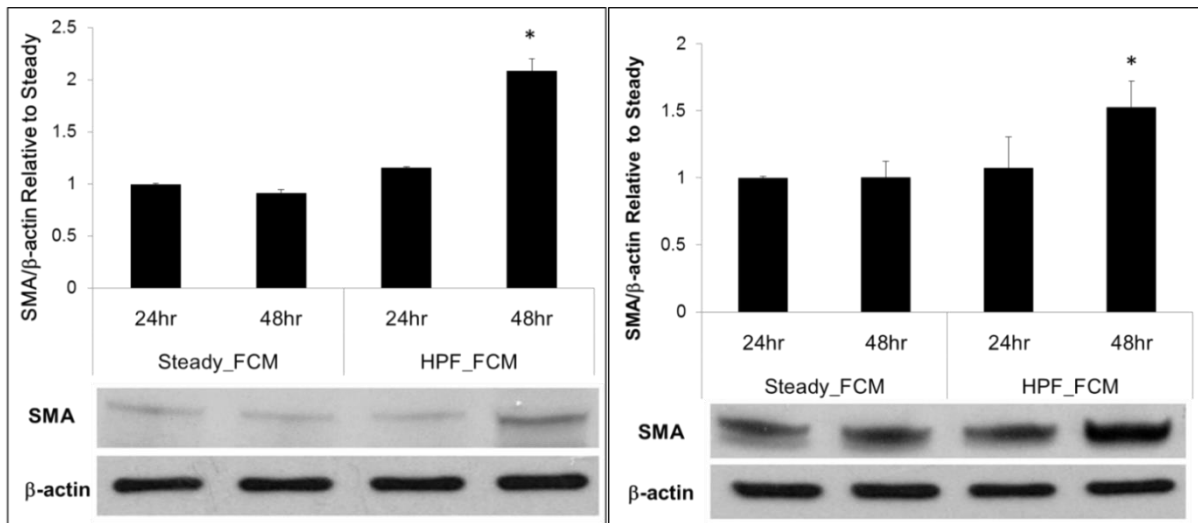
Figure 3.3.2.1- Flow-conditioned media (FCM) from ECs after 48 hr stimulation with HPF induced quiescent ECs and AdvFBs to express α-SMA protein expression. AdvFBs and ECs both cultured in FCM pre-conditioned with steady flow and HPF for both 24 hr and 48 hr time points. Quantitative measures of protein expression increase and representative western blotting bands are shown. (Left) Fold change of α-SMA/β-actin in AdvFBs cultured in different FCM conditions relative to that from the steady FCM. (Right) Fold change of α-SMA/β-actin in ECs cultured in different FCM conditions relative to that from the steady

FCM. Results showed that fractional differences in SMA dramatically increase for the 48 hr time points, with 127% and 52% for AdvFBs and ECs respectively. "*" shows $p < 0.05$ versus FCM from the steady flow condition after the same stimulation period.

In addition, migration and proliferation assays were performed on the AdvFB cultured with various FCM. As shown in Figure 3.3.2.2, migration assay results showed that significantly more AdvFB cells migrated towards FCM taken from ECs under HPF, when compared to the cells migrated towards steady flow, for both 24 hr and 48 hr time points. Proliferation assay results showed that AdvFB cell proliferation in FCM from HPF conditions was also significantly higher, when compared to that in FCM from steady flow, for both 24 hr and 48 hr time points.

| Steady 24hr FCM | Steady 48hr FCM | HPF 24hr FCM | HPF 48hr FCM |
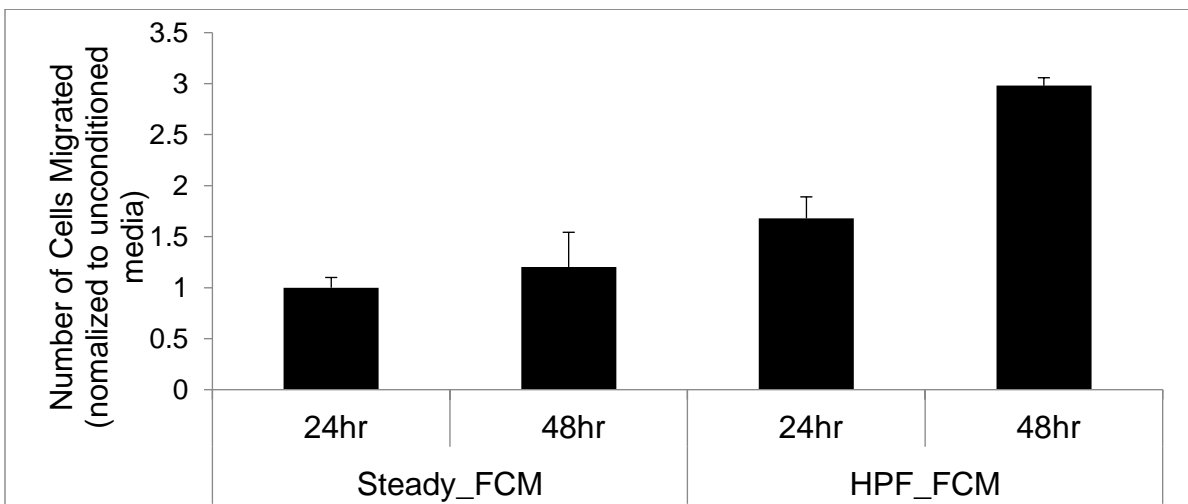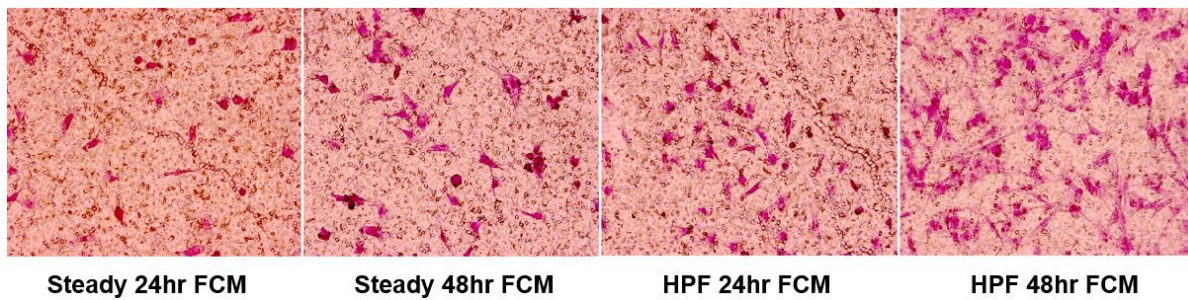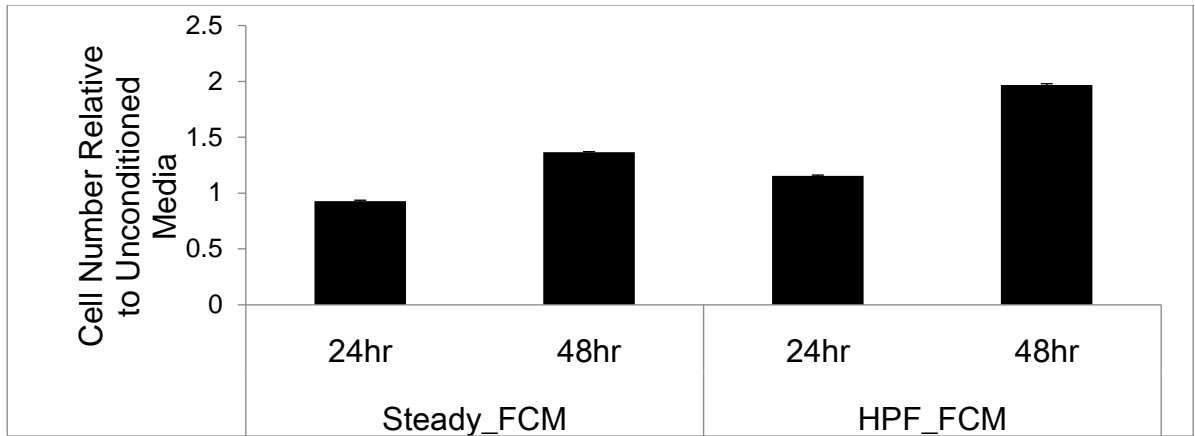
Figure 3.3.2.2- Flow-conditioned culture media from ECs exposed to HPF significantly enhanced AdvFB migration and proliferation. (Top) Representative images showing AdvFB migration towards flow conditioned media (FCM) from ECs under different flow conditions. AdvFBs are stained on the opposite side of the filter with crystal violet. (Middle) Quantitative results from AdvFB migration assays, showing fold changes of migrated cells in comparison with the control using unconditioned culture media. (C) Cell proliferation results of AdvFB cultured with FCM. Statistically significant results ($p < 0.05$) in AdvFB migration or proliferation are shown between FCM from high pulsatility flow and FCM from steady flow by (*) for similar time points. "†" shows statistically significant results ($p < 0.01$) between experimental conditions and the unconditioned media (control).

3.3.3 *Taxol reduced EndMT response of HPAEC*

Herein, we asked whether inhibiting microtubule dynamics using Paclitaxel (taxol) could inhibit microtubulin dynamics, and reverse the EndMT process of HPAECs under HPF stimuli. As shown in Figure 3.3.3.1, the addition of taxol reduced EndMT markers in HPAECs under HPF, including α-SMA, TGF-β1 and COLIA1, and retained the expression level of endothelial marker (PECAM-1). These results may be compared to steady-flow rate, which shows approximaMicrotubulin thus played an essential role in HPF-induced EndMT and stabilized the EC structure to protect cells from transitioning to a mesenchymal myofibroblast-like phenotype.
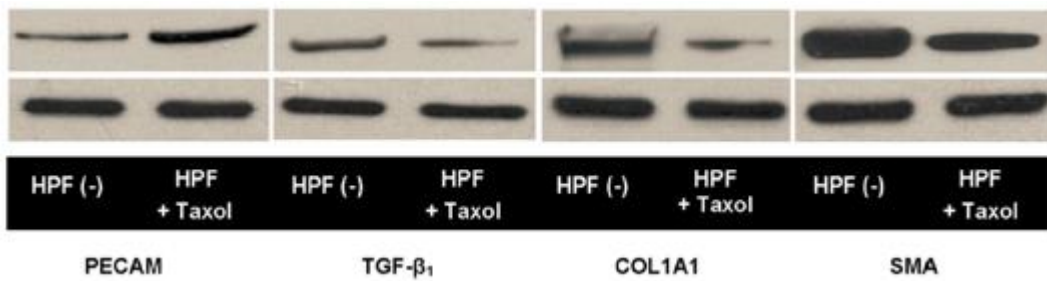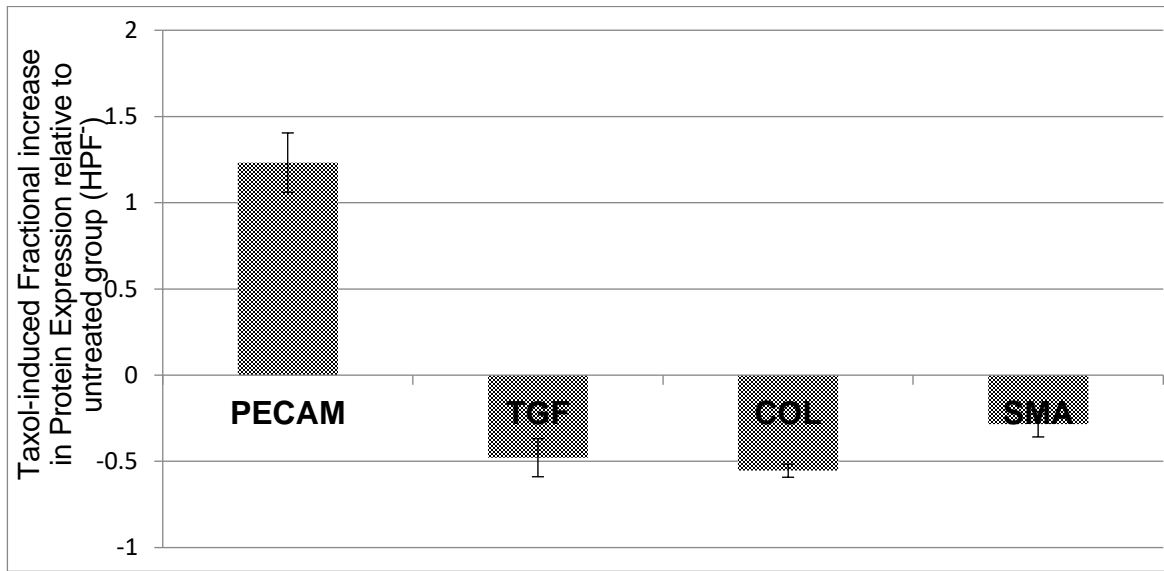
Figure 3.3.3.1- Results from western blotting assays show that taxol induced changes in the protein expression in ECs after 48 hr of HPF stimulation. Fractional increase in EC expression of EMT-related proteins after taxol treatment (HPF+Taxol) is shown in comparison with the untreated group, HPF(-). Quantitative measures of protein expression increase and representative western blotting bands are shown. Statistical significance ($p<0.05$) was found in all the protein expression comparisons between the treated and untreated groups. Increased PECAM expression as well as decreased TGF-β1, collagen I, and α- SMA all indicate a reduction in phenotype changes in ECs caused by HPF. Additionally, these results are additionally shown when taxol treatment (HPF+Taxol) compared to steady flow results, with the exception of α-SMA, which shows a significant increase.

3.3.4   Cell apoptosis preceded the EndMT

We therefore studied whether the occurrence of endothelial transition into a pathological fibroblastic

phenotype were preceded by endothelial apoptosis. To address this question, caspase assay was used to

assess cell apoptosis after 24 hr flow conditioning. Results showed that HPF induced much higher

percentage of apoptotic cells when compared to steady flow (Figure 3.3.4.1). The co-existence of

apoptotic cells and non-apoptotic cells are interesting facts of the HPF-induced changes.
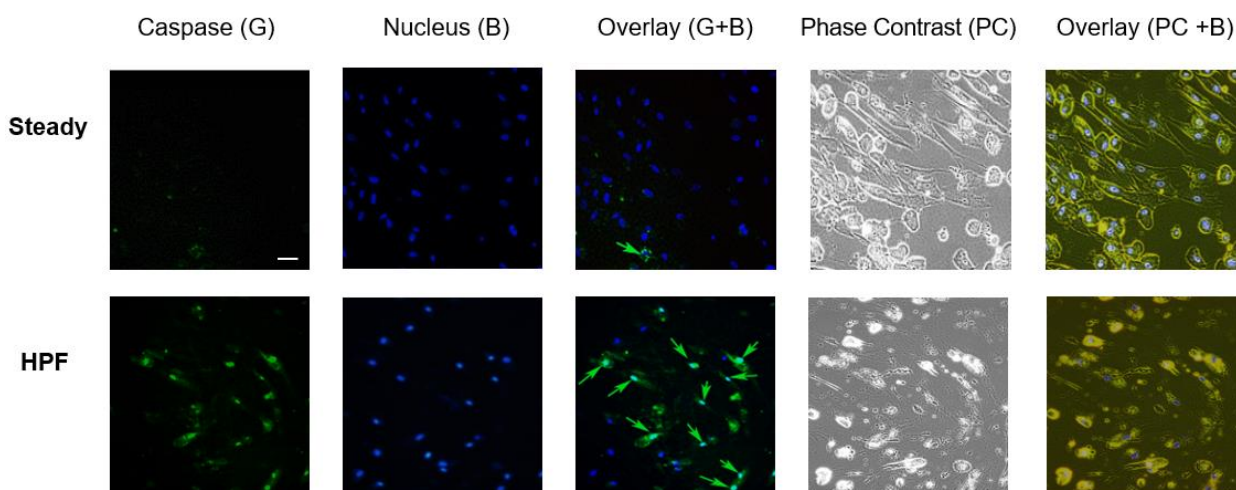
Figure 3.3.4.1- The EMT process of ECs is preceded with cell apoptosis.

3.4   Discussion

Results from the present study demonstrate that HPF induces EndMT in HPAECs, likely stemming

from HPF-induced endothelial dysfunction characterized by inflammation, adverse production of

vasoactive substances and apoptotic responses. Evidence is presented in gene and protein assays of cells

after 48 hr exposure to HPF, showing dramatic downregulation of PECAM-1 (EC marker), and

significant upregulation of mesenchymal cell markers including α-SMA, COL1A1, and TGF-β1. This

demonstrates EC changes into a myofibroblast-like mesenchymal phenotype. In addition, flow-

conditioned media further sustained the stimulating effects of HPF on EndMT and on activation,

60

migration and proliferation of AdvFBs, all of which are related to progressive fibrosis of vascular tissues in diseased conditions. We also found that paclitaxel application in the flow media effectively reduced EndMT response.

TGF-β_1 could play a critical role in perpetuating flow-induced vascular fibrosis. TGF- β_1 is such a highly potent cytokine that it alone may not only induce the inflammatory response, but also induce EndMT of ECs. [11, 42, 43] The presence of TGF-β_1 produced by HPAECs under HPF is likely instrumental in sustaining EndMT and increasing fibroblast proliferation, migration and activation to α-SMA+ myofibroblasts through myogenic process. Our finding is consistent with previous studies showing that TGF-β1 release was found after EC apoptosis, (Sakao, 2006; Sakao et al., 2005; Solovyan and Keski-Oja, 2005) or during EC exposure to high shear. (Cucina et al., 1998; Ten Dijke et al., 2012) TGF-β_1 has also been repeatedly shown to increase fibrosis and the encapsulation phase of the inflammatory response. More relevant to the current study is that TGF-β1 was shown to directly initiate EndMT in a number of previous studies. (Hashimoto et al., 2010; Imamura et al., 2010; Kokudo et al., 2008; Medici et al., 2011; Zeisberg et al., 2008)

Though little is known about cellular mechanisms underlying the EndMT and few successful chemical signals have been shown to prevent EndMT, evidence emerges that lack of primary cilia, acetylated microtubule, primes the EndMT process in the endothelium, while EndMT diminished with increasing primary cilia expression in ECs. (Egorova et al., 2011b) Our previous study showed that the microtubulin played an important role in transducing HPF to proinflammatory signals. (Li et al., 2009) Paclitaxel (taxol), inhibits microtubule dynamics and thus cell proliferation in cancer chemotherapy, has also been previously used to reinforce primary cilia. (Hamel et al., 1981; Hierck et al., 2008) Paclitaxel is commonly used in cancer chemotherapy to prevent tumor growth, and as prevention in restenosis through preventing SMC migration and proliferation. (Lao and Venkatraman, 2008) This study suggests that paclitaxel may attenuate vascular dysfunction by additionally helping to stabilize EC cytoskeleton and

reduce EndMT via altered endothelial mechano-transduction of HPF. (Egorova et al., 2011b; Hierck et al., 2008)

Different from previous studies on flow-induced endothelial dysfunction using disturbed flow, (Nagel et al., 1999) or oscillatory flow shear conditions (Ziegler et al., 1998) with the mean flow shear stress below a physiological value, as occurring in the case of arterial stenosis, HPF is characterized by unidirectional flow condition with the mean flow shear within the physiological range, and is correlated to increased upstream vascular stiffness. (London et al., 2011) The results shown here as well as our previous studies have provided evidence that HPF would create a positive feedback loop through applying high flow pulsatility to ECs on a stiff structure, exacerbating endothelial dysfunction and vascular fibrosis. Besides enhanced inflammatory response and EndMT in EC, HPF also led to increased apoptosis prior to EndMT. Previous studies have shown that a direct result of apoptosis-resistant EC, due to unfavorable flow conditions, chemically-induced EC apoptosis, or growth factor inhibition, is post-apoptosis proliferation of these cells; apoptosis-resistant ECs, likely showing a mesenchymal phenotype, may be hyperproliferative and more capable of withstanding harsh biochemical and biophysical stimuli. (Cucina et al., 1998; Sakao, 2006; Sakao et al., 2005, 2007, 2009; Scott et al., 2013; Ten Dijke et al., 2012) HPF fosters the emergence of mesenchymal fibroblasts, which likely are apoptosis-resistant cells either proliferating to thicken vascular intima by fibrosis or producing cytokines to activate fibroblast migration and proliferation. This may further explain *in vivo* findings of vascular fibrosis, which often is characterized by α-SMA+ cells in all vascular layers and/or increased intimal area. (Dilley RJ et al., 1988) The possible mechanism of HPF on vascular fibrotic remodeling is illustrated in Figure 7.
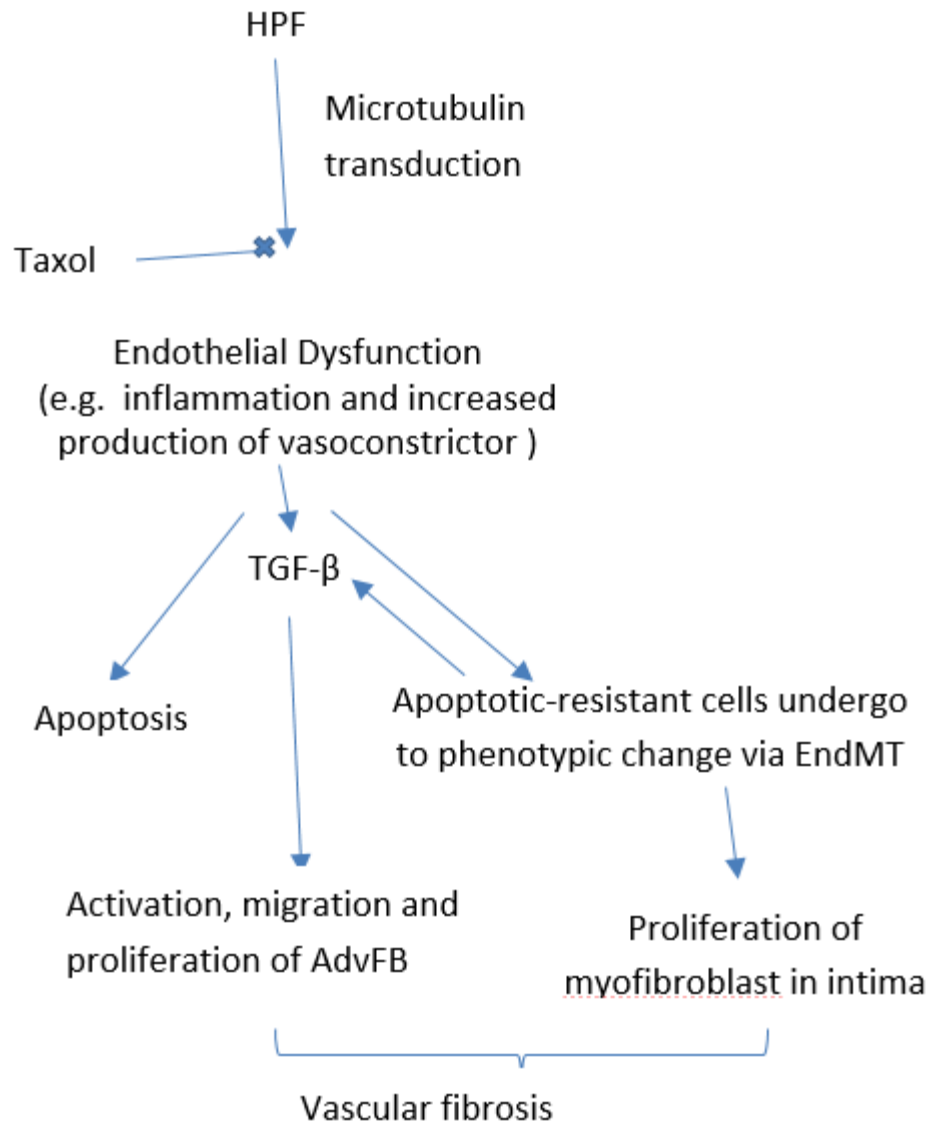
Figure 3.4.1- Possible mechanisms showing the effect of HPF on vascular fibrosis.

4   Silk Hydrogels of Tunable Structure and Viscoelastic Properties Using Different Chronological Orders of Genipin and Physical Crosslinking

Winston H. Elliott[†,‡,2], Walter Bonani[†,#], Devid Maniglio[†,#], Antonella Motta[†,#], Wei Tan[‡],

Claudio Migliaresi[†,#]

[†] *Department of Industrial Engineering and BIOtech Research Centre, University of Trento,*

Via Sommarive 9, 38123 Trento, Italy.

[‡] *University of Colorado Department of Mechanical Engineering, 1111 Engineering Dr. 427*

UCB, Boulder, CO 80309, U.S.A.

[#] *European Institute of Excellence on Tissue Engineering and Regenerative Medicine, and*

INSTM Trento Research Unit, Trento, Italy.

Keywords: Silk Fibroin Hydrogel, Genipin, High Pressure Carbon Dioxide, Large Amplitude Oscillatory Strain.

ABSTRACT

Catering hydrogel manufacturing process towards defined viscoelastic properties for intended biomedical use is important to hydrogel scaffolding function and cell differentiation. Silk fibroin hydrogels may undergo "physical" crosslinking through β-sheet crystallization during high-pressure carbon dioxide treatment, or covalent "chemical" cross-linking by genipin. We demonstrate here that time-dependent mechanical properties are tunable in silk fibroin hydrogels by altering the chronological order of genipin crosslinking with β-sheet formation. Genipin crosslinking before β-sheet formation affects gelation mechanics through increased molecular weight, affecting gel morphology, and decreasing stiffness response. Alternately, genipin crosslinking after gelation anchored amorphous regions of the protein chain, restricting reptation, and increasing stiffness. These differences are highlighted and validated through large amplitude oscillatory strain near physiologic levels, after incorporation of material characterization at molecular and micron length scales.

4.1 Introduction

During the past 30 years, engineered tissues have been researched as permanent treatments for many disorders.(Bartels and Lei, 1988; Lei et al., 1985) Tissue engineering implants require mimicry of tissue: chemically,(Aumailley and Timpl, 1986; Dahl et al., 2011) mechanically,(Dahl et al., 2011; Engler et al., 2006; Stewart and Lyman, 1992; Wingate et al., 2012) and morphologically, to best aid tissue growth. Both decellularized matrix,(Badylak and Nerem, 2010; Chen et al., 2001; Dahl et al., 2011) and novel biomaterials have been successful in developing new tissues. While decellularized matrices are advantageous in mimicking intended tissue, lab synthesized materials may still be a best option due to availability, storage, and cost. Hydrogels excel at mimicking tissue due to highly visco-elastic mechanical properties and nutrient transport capabilities.(Drury and Mooney, 2003; Peppas et al., 2000; Vepari and Kaplan, 2007) High porosity and hydrophilicity both aid in nutrient transport, especially peptide and protein-based drugs, through swelling and reduced adsorption,(Wahlgren and Arnebrant, 1991) leading to higher efficiencies. Due to the wide range of tissues requiring replacement, tunable hydrogels are ideal candidates for tissue engineering scaffolding.

While mechanical replacement of tissue has long been an emphasis in implantation medicine and tissue engineering, research in the last decade has shown that the cell interaction with scaffold mechanics is equally important. Tissue and implant mechanics have been shown as characteristic features in many disease pathologies(Ingber, 2003) and as critical factors to regulate cell activity,(Guo et al., 2006; Wang et al., 2000) such as stem cell fate.(Engler et al., 2006; Guilak et al., 2009; Wingate et al., 2012) Material stiffness may affect cells through cell deformation caused by matrix strain via cell adhesion sites,(Engler et al., 2006; Guo et al., 2006; Howard et al., 1997; Kim et al., 1999; Lee and Bader, 1997; Sen et al., 2008; Simmons et al., 2003; Wang et al., 2000; Wingate et al., 2012) where the time scale of strain loading is dependent on tissue use and location. Physiologic loading varies in frequency from static, to ~0.05 Hz in the small intestine, to ~1 Hz in the circulatory system, and to varied levels in orthopedics. The static environment, however, is most frequently used in examining cell activity,(Engler et al., 2006;

Guo et al., 2006; Wang et al., 2000; Wingate et al., 2012) which shows cell response over extended time scales.(Bao and Suresh, 2003; Wottawah et al., 2005) Stiffness of viscoelastic materials across a range of time scales offers frequency-dependent response for cells. Viscoelasticity of hydrogels measured by large amplitude oscillatory strain (LAOS) determines material response in application, and provides insight into contribution of microstructure to material stiffness response.(Guan et al., 2013; Hyun et al., 2011) Mechanical properties of hydrogels and tissues are dependent on hierarchical material organization, ranging from molecular structures to microstructures.(Discher, 2005; Saha et al., 2008) By characterizing material hierarchies of different length scales, we may gain more comprehensive understanding of hydrogel viscoelasticity, and thus develop new methods of tuning time-dependent properties.

Silk fibroin hydrogels are a versatile material, capable of excellent cell attachment and control of material properties. Silk fibroin derived from domesticated silk worms (*Bombyx mori*) is a long chain protein (~375 kDa) with repeat GAGAGS and GAGAGT amino acid sequences consisting of 90% of their primary structure. These repeat units form β-sheet secondary structures with hydrophobic side groups on their surface, leading to intra- and intermolecular, close-packed crystallization structures,(Bini et al., 2004; Hu et al., 2006, 2011) acting as "physical" crosslinks, resulting in stable gel structures. These gels can be highly porous and exhibit excellent cell attachment and viability.(Vepari and Kaplan, 2007) Fibroin gelation may occur through reduction of solution pH until the molecule isoelectric point is reached, and resulting nucleation and crystallization of the protein.(Ayub Haider et al., 1993) Fibroin stiffness is heavily reliant on secondary and quaternary protein structures and the overall content of β-sheet crystals within the gel.(Hu et al., 2006, 2011; Keten et al., 2010) Morphology of gel microstructure,(Discher, 2005; Hollister, 2005; Saha et al., 2008) and resulting pore connectivity,(Hollister, 2005; Mak, 1986) also contribute material stiffness response.

In addition to crystallization or physical crosslink through β-sheet formation, silk fibroin can be chemically crosslinked. Genipin, due to its low cytotoxicity and ease of use, is a common chemical crosslinker.(Bi et al., 2011; Madhavan et al., 2010; Silva et al., 2008a; Xiao et al., 2012; Yao, 2003) It

contains a bicyclic, fused ring structure of pentane and dihydropyran rings, and covalently bonds to primary amine structures,(Butler et al., 2003) often forming dimer bridges during crosslinking.(Mi et al., 2005; Sundararaghavan et al., 2008) Primary amines are available at the protein N-terminus and 2% of fibroin amino acid side groups,(Marsh et al., 1955; Wang et al., 2013a) allowing additional, but limited, tailoring of material by chemical crosslink formation.(Butler et al., 2003) Additionally, genipin crosslinking (GCX) was shown to increase fibroin "physical" crosslinking by β-sheet crystallization in both electro-spinning,(Silva et al., 2008a) ultrasonication gelation,(Sun et al., 2014) and film castings.(Motta et al., 2011) Genipin reactivity is proportional to its concentration, crosslinking temperature and time,(Bi et al., 2011; Madhavan et al., 2010; Nickerson et al., 2006) but is reduced at low pH,(Mi et al., 2005) allowing for control over crosslink density. Increased stiffness from changes in chemical cross link density by genipin content could be quantifiable by coloration changes,(Butler et al., 2003) primary amine content,(Foss et al., 2013; Sun et al., 2014) and fluorescence.(Sundararaghavan et al., 2008)

Though crystallization and genipin crosslinking are both employed in previous studies to manufacture fibroin hydrogels, no studies have been attempted to examine the impact of the sequence of using both processes for manufacturing.(Motta et al., 2011; Silva et al., 2008a, 2008b; Sun et al., 2014; Wang et al., 2013a; Xiao et al., 2012) Combining crystallization with chemical crosslinking may provide more control over hydrogel properties such as mechanical stiffness, viscoelastic ratio, and gel microstructure. However, the chemical crosslinking process is reliant on contact between two primary amine groups and the genipin molecule, which is limited by low primary amine amounts in fibroin and restricted diffusion and reptation within the hydrogel with β-sheet crystals. Additionally, the reaction would be limited by low pH of the solution during the gelation process of crystal formation. Therefore, optimizing crosslinking potential would be reliant on material phase transition and its relation to the order of crosslinking treatments; the chronology of these two processes can greatly influence the stiffness and morphology of fibroin gel.

This paper examines the interaction between chemical crosslinking and crystallization in the formation of fibroin hydrogels. We have previously developed high pressure carbon-dioxide treatment (PCT) to decrease solution pH for β-sheet crystal formation in silk fibroin, which improved gel structure when compared to common citric acid titration methods.(Floren et al., 2012) We also characterized silk fibroin materials chemically crosslinked with genipin.(Silva et al., 2008a, 2008b; Sun et al., 2014) Bulk gel strength, stiffness, degradation rate, and swelling properties are highly reliant on crosslink density.(Bi et al., 2011; Eichenbaum, 1992; Madhavan et al., 2010) Incorporation of these separate effects would allow for control over gel structures and properties. Cell response and activity may be improved and/or dependent on control of hydrogel scaffolding material properties over various time and length scales. By characterizing gel material properties at the molecular and micron length scales, and comparing to modeled viscoelastic modulus, we may better interpret tunability of genipin/fibroin gels. Herein, we characterize how tunability of genipin/fibroin hydrogel frequency response and viscoelastic moduli are dependent on the order of crosslinking treatments.

4.1 Materials and Methods

4.1.1   Materials

Bombyx mori polyhybrid silkworms were bred and selected by Centro Sperimentale di Gelsibachicoltura (Como, Italy). Silk cocoons were kindly supplied by Cooperativa Sociolario (Como, Italy). Lithium Bromide salt (LiBr) was purchased from Fluka Chemicals (Buchs, Switzerland) and Genipin was obtained from Waco Chemicals (Neuss, Germany). Other reagents, buffers and salts were purchased from Sigma-Aldrich (St. Louis, MO, U.S.A.) and used without further purifications.

4.1.2   Preparation of Silk Fibroin Solution.

Silk fibroin solutions in water were prepared according to Kim et al.,(Kim et al., 2005) with limited modifications. First, *Bombyx mori* cocoons were degummed to remove sericin proteins; silk cocoons were

treated twice in alkaline water baths at 98°C for 1.5 hr with concentrations of 1.1 g/L and 0.4 g/L Na_2CO_3, respectively. Degummed silk was then washed several times in de-ionized (DI) water and dried at room temperature (RT) to obtain pure silk fibroin fibers. Fibroin fibers were then dissolved in 9.3M LiBr (2 g of fibroin in 10 mL of LiBr solution) at 65°C for 2.5 h. The solution was then dialyzed against DI water for 3 days at RT in a Slide-A-Lyzer dialysis cassette (3.5K MWCO, Pierce, Rockford, IL, USA) to remove the LiBr salt and then filtered through a ceramic filter foam (porosity <5 μm) to eliminate impurities. Protein concentration was determined using a NanoDrop ND-1000 spectrophotometer (Nanodrop Tech Wilmington, DE, USA), and concentration was adjusted to 4 %w/v. Fibroin solution was then frozen in liquid nitrogen and stored at -80 °C until use. Frozen solution was later thawed at RT, re-filtered to remove any aggregate formation, and concentration was adjusted to 3% to obtain working fibroin solutions. For all solutions except control, genipin was added to obtain a 1mM concentration within the 3% fibroin solution.

4.1.3   Hydrogel Formation

4.1.3.1 High Pressure CO_2 reactor

Fixed volumes (240 μL) of initial fibroin solution were pipetted into custom-made polytetrafluoroethylene (Teflon) cylindrical molds (8mm Diameter x 5 mm Depth) and placed within a stainless steel high pressure reaction vessel (BR-300, Berghof Products + Instruments, Eningen, Germany). The temperature of the reactor was controlled through an electrical heating jacket run by a BDL-3000 temperature controller (Berghof). CO_2 gas was introduced in the reactor and pressurized at a working pressure of 60 bar through a high-performance liquid chromatography (HPLC) pump (Model 426, Alltech, Deerfield, IL, USA).

4.1.3.2 Fibroin gelation

Genipin was activated to chemically crosslink neighboring fibroin molecules by heat-treating samples at 37^OC for a minimum of 24 hours. To prevent GCX reactions during PCT, temperature during the treatment was held at room temperature, unless otherwise noted. Control samples were fabricated at 37^oC during PCT, consistent with previous work.(Floren et al., 2012) Co-crosslinked (CCX) samples were treated at 37^OC during PCT, allowing for maximum genipin activation during the physical crosslinking process. All other gels underwent heat treatment for 24 or 48 hours, before (Pre24CX, Pre48CX) or after (Post24CX) PCT. After gel formation, samples were immediately submerged in 5 mL DI water, and stored at 4^OC. DI was changed after 24 hours to remove any free genipin residual diffused out of gels. Any samples visibly fractured or damaged during the gel removal process from the mold were removed from mechanical testing.

4.1.3.3 Modeling CO_2 Diffusion

Diffusion of CO_2 into the fibroin solution and the resulting pH was modeled using coefficient values determined by Duan et al.(Duan and Sun, 2003; Duan et al., 1992, 2006), and the pH model of CO_2 in fibroin solution derived by Floren, et. al.(Floren et al., 2012) Resulting concentrations were discerned for 60 bar and temperatures of 20°C, 22°C, 25°C, and 37°C. Modeling shows higher concentration equilibrium at lower temperatures, and therefore faster diffusion of CO_2 into the fibroin solution. These values concur with tables listed in Duan et al.(Duan and Sun, 2003; Duan et al., 2006) Resulting pH was between 1.5 and 4, where gelation occurs through fibroin approaching the isoelectric point, and a plateau region in gelation times.(Ayub Haider et al., 1993)

4.1.4   Molecular Structure

4.1.4.1 Determination of amino acid composition by RP-HPLC

The amino acid content of frozen fibroin samples was determined with Waters AccQ-Fluor™ Reagent Kit using the AccQ-Tag™ amino acid analysis method (WatersCorp., Milford, MA, USA). Briefly, fibroin-based hydrogels and solutions, without genipin, were frozen in liquid nitrogen and freeze-dried using a Lio-5P lyophilizer (5Pascal, Milan, Italy). About 5 mg of lyophilized fibroin were hydrolyzed with 6 N HCl at 114 ± 2 °C in a silicone oil bath for 24 h. Air-dried hydrolysates were later reconstituted with 20 mM HCl to obtain a solution at a concentration in the range 4-200 pmol and then derivatized with Water AccQ Flour Reagent to obtain stable amino acid. The amino acid content was determined by reverse phases high performance liquid chromatography (RP-HPLC) using a AccQ-Tag™ column (Waters Corp) with a gradient of Waters AccQ-Tag™ Eluent A, Milli-Q water and Acetonitrile (HPLC grade) at a flow rate of 1 ml/min. The amino acids were detected with Jasco UV-1570 detector set (Jasco, Bouguenais, France) at 254 nm. The chromatograms obtained were compared with waters amino acid hydrolysate standards to identify single amino acid residues.

4.1.4.2 Molecular weight measurement by GPC

Gel permeation chromatography (GPC) analysis of the fibroin samples was conducted with a Shodex SB-805HQ column (Shodex OH pak®, Showa Denko, Munich, Germany). Freeze-dried fibroin-based hydrogels and solutions were re-dissolved in 9.3 M LiBr at 65°C for 0.5 h. The obtained fibroin solutions were dialyzed against DI water at RT and diluted with eluent solution (3 M Urea, 0.02 M Tris HCl, 0.15 M NaCl, pH 7.5) to obtain a protein concentration in the range of 0.5-0.8 mg/ml. The chromatography system was operated with a flow rate of 1 ml/min at 27 ± 1 °C and elution was detected with a Jasco UV-1570 detector set (Jasco, Bouguenais, France) at 224 nm. Calibration curve was obtained with Low/High Molecular Weight Gel Filtration Calibration Kit (GE Healthcare Europe, Freiburg, Germany).

4.1.4.3   Determination of genipin crosslinking activity by confocal microscopy

Previous literature shows GCX content is fluorescent with the excitation peak at 590 nm and emission peak at 630 nm.(Sundararaghavan et al., 2008) Increased fluorescence from GCX formation occurs due to increased π-bonding within the genipin bicyclic fused ring structure after opening of the dihydropyran ring.(Butler et al., 2003; Mi et al., 2005; Sundararaghavan et al., 2008; Wang et al., 2013a) Further increase in π-bonding and genipin concentration may occur in genipin dimerization during cross-linking, and is a commonly proposed mechanism of genipin crosslinking,(Mi et al., 2005; Sundararaghavan et al., 2008) including to fibroin.(Wang et al., 2013a)

Lyophilized gels were rehydrated using DI for 24 hours. Maximum GCX efficiency was measured by Control gels immersed in 15 mM glycine solution and 1 mM genipin for 24 hours at 37°C. Samples were removed from DI and separated on a single chamber slide, partitions removed, and a second glass slide placed over the samples to ensure homogeneous surface depth. Samples were then imaged using confocal microscopy (Nikon Corporation, Chiyoda, Tokyo, Japan). Genipin was excited by means of a diode pumped solid state laser (561±0.5 nm, Melles Griot). Emission band collected ranged from 616-658 nm, with the gain set to maximize emission intensity without saturation for the gel with the highest emission intensity, and kept constant for all the others. Images where collected using a 20x Plan Flu objective with 2x scanning zoom (40x total, 4.97 μm/pixel resolution). Microscope pinhole was opened maximally to permit high PMT sensitivity, even with low emitting samples, and from the thickest optical section possible (7.83 μm), with a dwell time of the laser equal to 12.6 μs/voxel. After maximum emission intensity was determined within the sample set, program settings were maintained as a method of comparing between samples. Max GCX allows the determination of the overall GCX efficiency. Summation of emission intensity over the given area was recorded and converted to numerical byte values for each pixel in a 64 x 64 matrix. Images were analyzed using NIS-Elements Viewer (Nikon Corporation), and emission intensities were determined with ImageJ (NIH, Bethesda, MD, USA).

4.1.4.4 Determination of chemical crosslinking density by ninhydrin assay

Ninhydrin assay was used determine active genipin content(Foss et al., 2013). Ninhydrin reacts with active NH_2 groups, producing a visible purple color, detectable at 570 nm wavelength by spectrophotometer. By comparing ninhydrin content between control and variable gel samples, genipin bonding conditions may be determined. To ensure protein primary structures in samples were preserved, samples were first flash frozen by submerged in liquid Nitrogen and subsequently lyophilized at temperature of -50^OC and pressure of 5 mmHg for no less than 24 hrs. Ninhydrin (Sigma-Aldrich) solution of 0.35% w/v in ethanol (>96%) was added to lyophilized samples to a concentration of approximately 5 mg/mL, and heated at 90°C for 30 minutes under mild shaking. Each solution was made in triplicate; blank and glycine control solutions underwent the same treatment. After cooling down, optical absorbance of each solution was measured at 570 nm using a microplate reader (Tecan Group AG, Männendorf, Switzerland). Change in primary amine available was calculated as:

$$\Delta Primary\ Amine = \frac{NHN_{Sample}}{NHN_{Cntrl}}\ (1)$$

Where NHN_{Sample} is the color intensity presented by ninhydrin assay performed on the variable sample, and NHN_{Cntrl} is the color intensity presented by the control gel.

4.1.4.5 Determination of physical crosslinking density by Fourier Transform Infrared Spectroscopy

Protein secondary structures were determined through Fourier transform infrared spectroscopy (FTIR) Spectrum One (Perking Elmer, Waltham, MA, U.S.A.) with Zinc Selenide crystal. Two additional samples were compared with Control samples: Amorphous is fibroin solution which has not undergone PCT, and Genipin is 3% fibroin which has undergone 1mM genipin crosslinking for 48 hours without undergoing PCT. To preserve protein secondary structure, samples were lyophilized, then placed in FTIR sampling surface and compressed until a minimum force of 100N was reached. Sample spectra were averaged over 4 scans, ranging from 650 cm^{-1} to 4000 cm^{-1} at a resolution of 4 cm^{-1}.

4.1.5   Microstructure Visualization

4.1.5.1   Scanning electron microscopy imaging

Imaging of samples was obtained using a scanning electron microscope (Quanta 200 FESEM). Prior to imaging, lyophilized cross sections were sputter coated (Biorad SC500, Hemel Hempstead, U.K.) with a thin layer of gold or platinum/palladium mixture.

4.1.5.2   Confocal microscopy imaging

It is difficult to image hydrogel microstructure without altering gel structure using lyophilization or environmental SEM. Therefore, wet gel samples were stained with Rho 123, a fluorescent small molecule capable of penetrating bulk gel material, and then imaged with confocal microscopy. Samples were placed in Rho 123 solution at 4^OC for 24 hours for staining, and then put in DI at 4^OC for 72 hours to remove the dye from pores. Gels were then placed on glass slides for confocal imaging.

4.1.5.3   Image Analysis

Images were analyzed both quantitatively and qualitatively. Pore dimension was determined using ImageJ. Results were compared across gel sample sets, and between same sample sets across different imaging modes (Confocal vs SEM). Qualitative analysis was done by comparing morphology and gel structure across gel sample types.

4.1.6   Mechanical Properties

4.1.6.1 Swelling Ratio

Gels were submerged in DI for a minimum of 24 hours and stored at 4^OC. Before mass measurement, samples were brought to room temperature and weighed. Subsequently, samples were submerged in liquid nitrogen and lyophilized. Dried samples were then weighed, and the swelling ratio was determined with the equation below:

$$Swelling\ Ratio\ = \frac{(m_{wet} - m_{dry})}{m_{dry}} \qquad (2)$$

Where m_{wet} is the mas of the fully hydrated sample, and m_{dry} is the mass of the lyophilized sample.

4.1.6.2 Mechanical Response

Large amplitude oscillatory strain (LAOS) in compression was performed to establish the viscous and elastic properties of the material. Frequency sweep of cyclic, uniaxial compression testing was used to determine approximate location of the transition frequency (ω), first harmonic storage modulus (E_1'), and first harmonic loss modulus (E_1'') of samples. Samples were placed between horizontal, quartz slides attached to both the base fixture and driving piston of a mechanical testing machine. (Bose, Eden Prairie, MN, U.S.A.) The driving plate was brought into contact with the gel, and DI was placed around the gel, with surface tension allowing DI to maintain its integrity for the duration of the test. Subsequently, an average strain of 25% was applied in compression and the system allowed to reach equilibrium. Dynamic strain was then oscillated at peak-to-peak amplitude of 20% strain, chosen from previous studies,(Howard et al., 1997; Kim et al., 1999; Lee and Bader, 1997; Park et al., 2004) and *in vivo* examples.(Fung and Liu, 1992; Kalath et al., 1986) Oscillation frequencies ranged from 2.202E-3 to 1 Hz, where plateau in response was reached. Data was recorded after 4 seconds of pre-conditioning of the sample for each frequency.

Data was analyzed using Wolfram Mathematica (Wolfram Research, Champaign, Illinois, USA). Discrete Fourier-Transform was taken of both strain and stress data. Complex modulus (E_1*) of the first harmonic was discerned from stress and strain response at the dominant frequency. Stress data curves were additionally smoothed through convolution with the normalized Gaussian kernel. Bandwidth varied with data frequency. Resulting smoothed curves were plotted against strain data to measure and visualize hysteresis curves, as well as overall stiffness response (E).

4.2 Results and Discussions

Results from the study have shown significant changes in the material structure and gel property among all the silk fibroin gels, with the presence of genipin as well as the order of crosslinking treatment.

4.2.1   *Physical appearance of gels*

Because genipin is known to produce a distinct blue coloration after GCX occurs while fibroin aggregation produces a white and/or cloudy liquid, the physical appearance of the gels suggests the status of protein aggregation and crosslinking. Thus, we first studied the physical appearances of both the solution and the gels of the genipin/fibroin solution. All the fibroin and genipin/fibroin solutions were initially transparent with no coloration. The minimal primary amine content in fibroin, and genipin concentration in solution would necessitate increased reaction kinetics to have significant GCX formation between fibroin molecules. To test this, fibroin and genipin/fibroin solutions were compared after 24, 36, and 48 hours at both $20^{O}C$ (room temperature or RT) and $37^{O}C$. Genipin/fibroin solutions held at RT after a period of 24 hours indicated no color changes or noticeable increases in solution turbidity. After a period of 36 and 48 hours at RT, they showed a faint blue coloration, with minimal aggregation or no visible increases in turbidity. Minimal aggregation and coloration ensured chemical crosslinking is confined to the heat treatment (at $37^{O}C$) step. Fibroin and genipin/fibroin solutions held at $37^{O}C$ still did not exhibit visible turbidity and remained a liquid after 24 or 48 hours. But the genipin/fibroin solutions showed a medium blue color after 24 hours, and turned into a darker blue coloration after 48 hours. The color changes in the solutions correlated well with the corresponding gel samples: Pre48CX and Pre24CX gels both showed blue coloration, with darker color in Pre48CX, while the Control, CCX, and Post24CX gels did not exhibit color changes, all showing white and translucent. Figure 4.3.1.1 summarizes the results with preparation protocols and representative pictures of the gels.
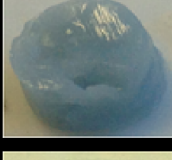
Figure 4.3.1.1- Preparation protocols and physical appearances of the gel samples. All samples were prepared from 3% w/v concentration of silk fibroin. The protocols show the order and degree of genipin crosslinking (GCX) with shaded blocks. Processing temperature during each 24 hour block is listed, along with the cumulative time of processing. Herein, the control gels were from pure fibroin solution with 24hr PCT-induced crystallization, while all the other samples contained 1mM concentration of genipin. Representative pictures of gels illustrating sample coloration and shape are shown on the right.

4.2.2   Molecular Structure

Results from RP-HPLC did not show significant alterations in the protein amino acid composition and therefore minimal difference in protein primary structure, among different gels.(Marsh et al., 1955) The

protein secondary and quaternary structures showed no difference when compared to the control. All the gels showed high concentration of intermolecular β-sheet crosslinking, with no variation in the peak locations or intensities.

Results from GPC showed significant increases in both number-average and weight-average molecular weights (M_N and M_W, respectively) for Pre48CX, when compared to control gels. As illustrated with the Pre48CX curve, the GCX formation presented a distribution more skewed towards higher molecular weights, with both M_W and M_N higher than control gels. (Figure 4.3.2.1)
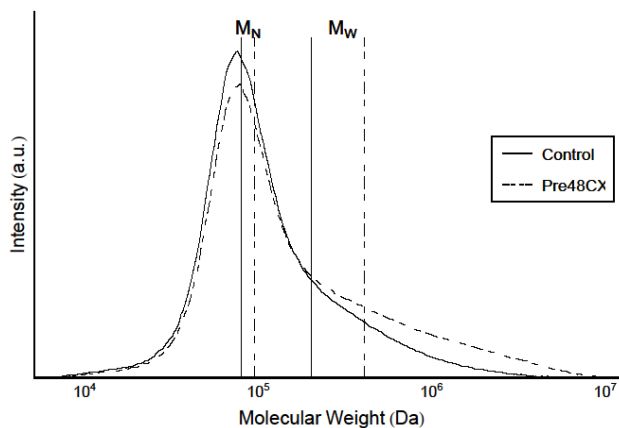
Figure 4.3.2.1- Gel permeation chromatography results, showing an increase in both M_N and M_W for gels with genipin crosslinking before gelation.

To further understand GCX mechanism in changing the molecular structure, confocal microscopy was used to image GCX fluorescent signals. Results demonstrate significant increases of fluorescence emission in all GCX gels, when compared to control gels. (Figure 4.3.2.2) The GCX concentration in Pre48CX and Pre24CX correlates with the crosslinking time.
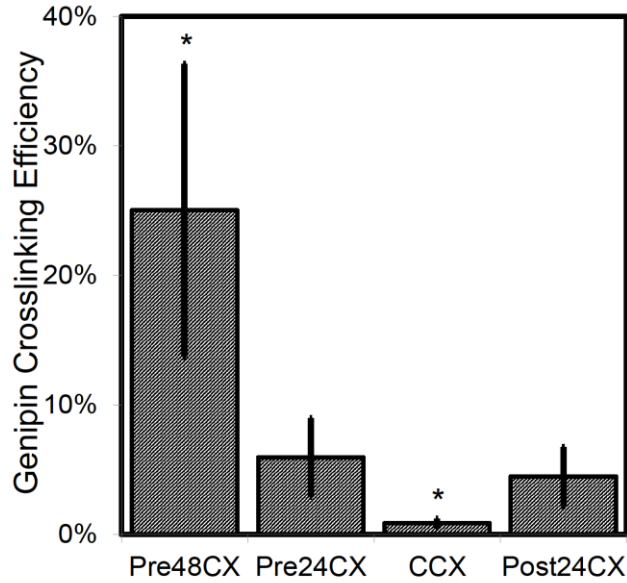
Figure 4.3.2.2- Genipin fluorescence emission results. Lyophilized and rehydrated samples were examined for genipin crosslinking (GCX) efficiencies, illustrated with the average intensities from confocal images. Results show the fluorescent signals from all the crosslinked gels are statistically ($p<0.10$) different from control. Also, Pre48CX and CCX show statistically significant ($p<0.10$) differences from all other crosslinked gels (labeled with "*").

To examine the genipin activity along single fibroin chains, ninhydrin assay was used. Results demonstrate significant decreases in primary amine groups for all GCX samples compared to the control. (Figure 4.3.2.3) Results do not correlate with confocal fluorescence data.
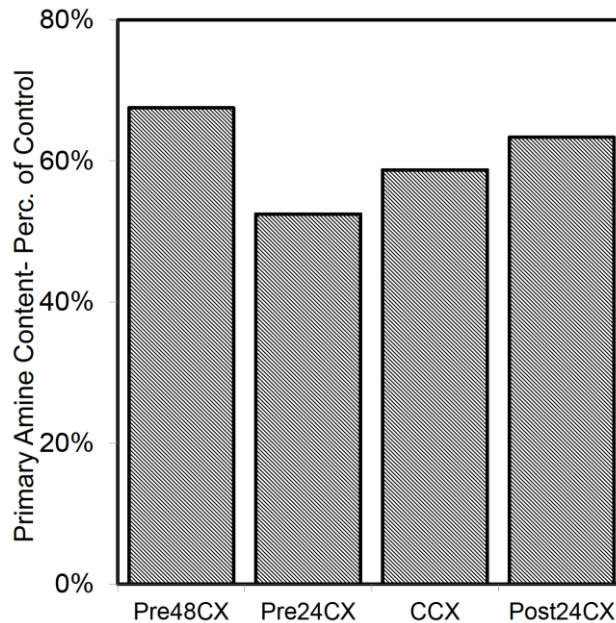
Figure 4.3.2.3- Primary amine sites quantified by ninhydrin assay. Results show the fraction of primary amine quantity in GCX gels (y-axis), when compared to control gels. All gels show decreased fraction in primary amine groups. Higher reduction in primary amine groups suggests increased genipin reactivity at bonding sites along single fibroin chains, rather than reaction between two fibroin molecules.

To characterize changes in major functional groups among gels, FTIR was used. Infrared spectroscopy results show that the presence of genipin or the order of crosslinking treatment did not induce any changes in peak locations or intensities. (Figure 4.3.2.4A) Resulting peaks were typical for fibroin hydrogels, as previously shown by our lab.(Floren et al., 2012; Sun et al., 2014) Specifically, all results showed the peaks representing strong, intermolecular β-sheet structures (1622 cm^{-1}, amide I(Hu et al., 2006)), weak β-sheet structures (1700 cm^{-1}, amide I(Hu et al., 2006)) and peak shift for tyrosine side chains (1516 cm^{-1}, amide II(Hu et al., 2011)), while peaks representing α-helix structures (1656-1662 cm^{-1}, amide I(Hu et al., 2006)), random coils (1640-1655 cm^{-1}, amide I;(Hu et al., 2006) 1540 cm^{-1}, amide II(Hu et al., 2011)), turns (1663-1696 cm^{-1}, amide I(Hu et al., 2006)), or side chain residues (1605-1615 cm^{-1}, amide I(Hu et al., 2006)) were not present. In comparison, FTIR results of amorphous fibroin which

82

did not undergo PCT with or without GCX (Figure 4.3.2.4B) showed peaks at 1645 cm^{-1} (random coil) and 1516 cm^{-1} (Tyr side chains). Amorphous fibroin after GCX showed an additional peak at 1532 cm^{-1}, which may result from in-plane deformation of genipin bicyclic, fused ring structure.(Suryani and Liu, 2009) In summary, lyophilized silk solution without PCT-induced crystallization indicated no β-sheet formation, even after 48 hours of GCX.
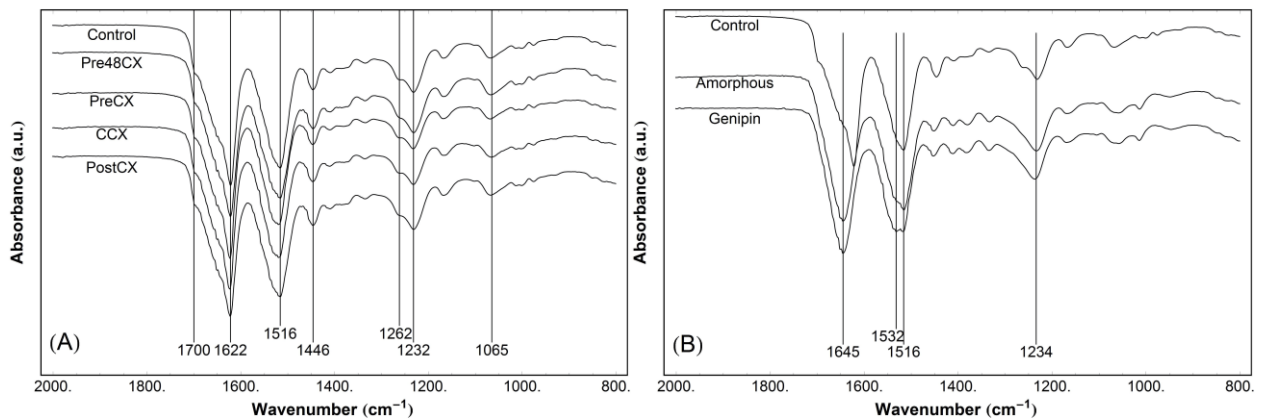
Figure 4.3.2.4- Infrared Spectra (FTIR) showing similar peak patterns among gel samples treated with PCT. (A) All gels presented high similarity in all major peaks of FTIR spectra, which showed the tight, intermolecular β-sheet crystals (1622 cm^{-1}) and weaker β-sheet structures (1700 cm^{-1}) of fibroin. (B) Lyophilized fibroin solutions without or with genipin crosslinking, undergoing no PCT gelation, are compared to the Control with PCT gelation. Both fibroin solutions present random coil (1645 cm^{-1}) and Tyrosine side chain peak shift (1516 cm^{-1}), common in amorphous fibroin. Additionally, there is a peak at 1532 cm^{-1} in fibroin with genipin crosslinking, possibly resulting from in-plane deformation of the genipin bicyclic, fused ring structure."

4.2.3   *Microstructure from SEM and confocal imaging*

SEM images show that the gel microstructure changes with the crosslinking order. Two types of morphology were found in SEM images (Figure 4.3.3.1). Control gels and gels with GCX during or after PCT (CCX and Post24CX) exhibit porous microstructure with limited connectivity between pores. Low connectivity between pores is determined by decreased concentration of connected perforations, as illustrated with blue circles in Figure 4.3.3.2. Contrarily, gels with GCX before PCT show more fibrous morphology and higher pore connectivity. Morphology changes were more drastic in Pre48CX.

Confocal imaging results supported SEM findings by showing evenly distributed pores of uniform size within the saturated, wet gel. (Figure 4.3.3.3) No changes were found along the depth of the gel, indicating homogeneous gel formation.
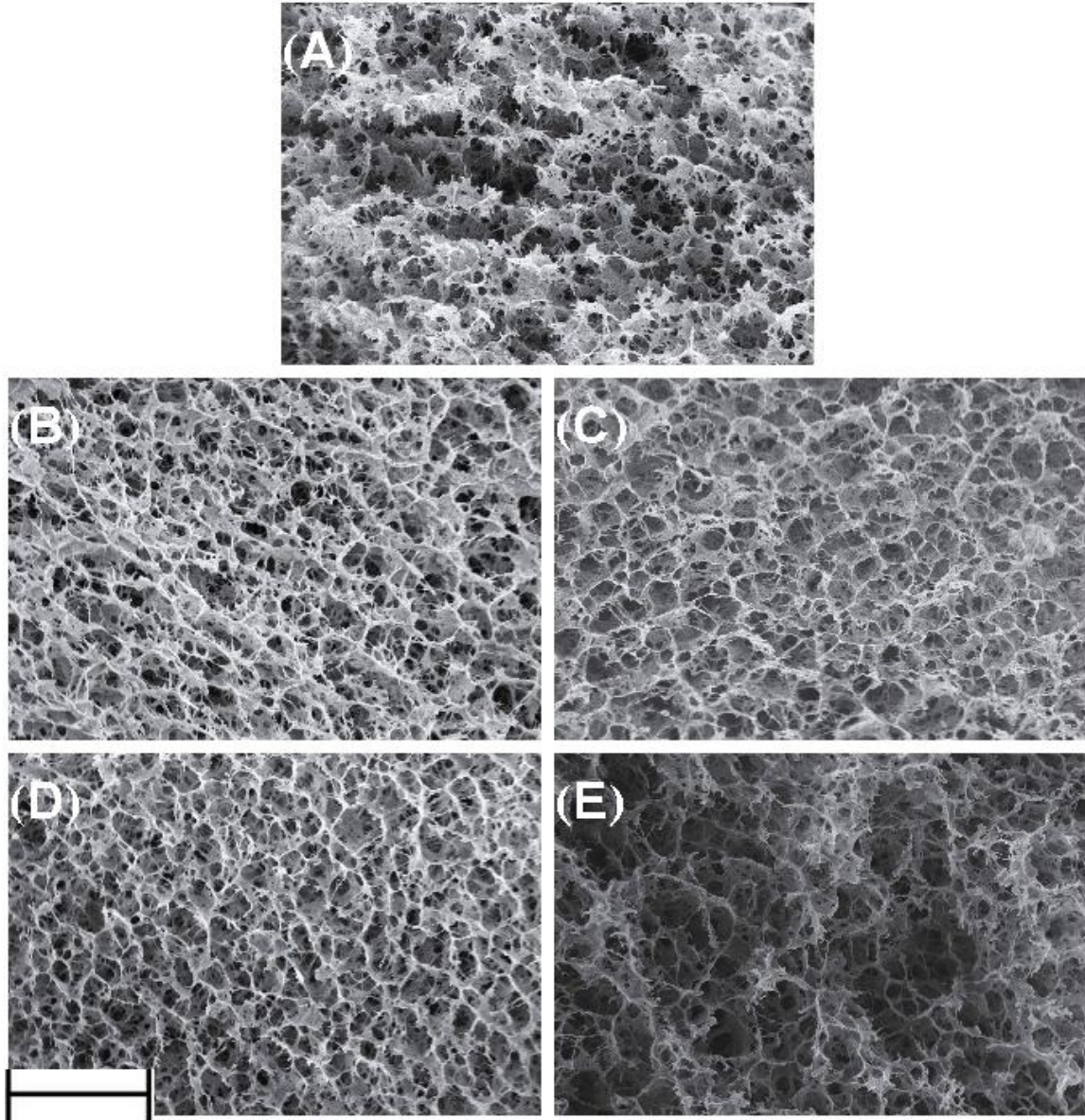
Figure 4.3.3.1- SEM micrographs showing the gel microstructure and morphology. (A) Control gel showed uniform pores with limited connectivity. (B) Pre48CX gels presented greater average pore size and more fibrous structure with high connectivity. (C) Pre24CX gels presented even larger pores with connectivity lower than Pre48CX. (D) CCX gels slightly increased pore size and connectivity when compared to the Control. (E) Post24CX gels presented little change in morphology from the Control. *Scale bar equals 10μm.*
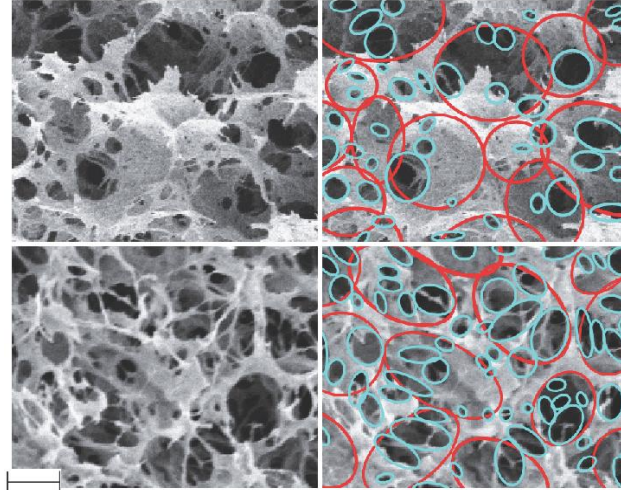
Figure 4.3.3.2- Comparison of Control (Top) and Pre48CX (Bottom) microstructures. The images on the right panel illustrate analysis of pore changes in the pore structure (red) and connecting perforation (blue). *Scale bar equals 3 μm*
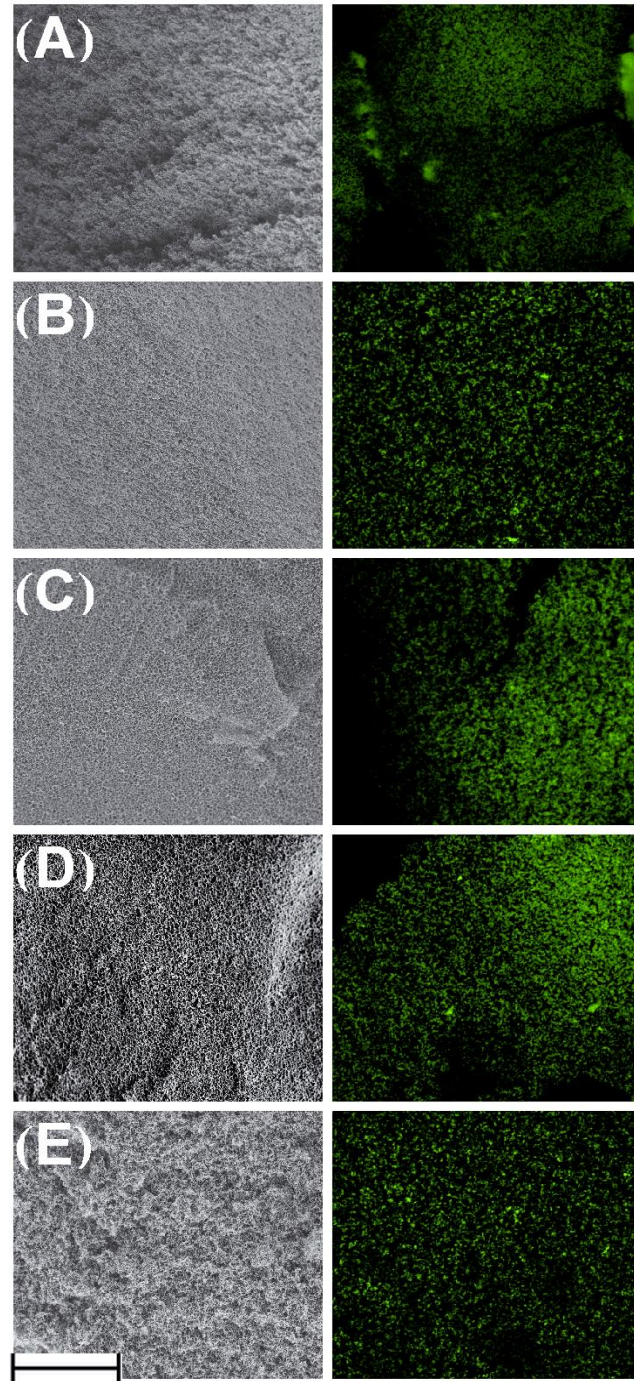
Figure 4.3.3.3. SEM (left) and confocal microscopy (right) images, showing the gels in dry and wet environments, respectively. These correlated images demonstrate that the gel microstructure retained after hydration. Confocal imaging was performed by illuminating pores with Rhodamine 123. *A: Control; B: Pre48CX; C: Pre24CX; D: CCX; E: Post24CX. Scale bar equals 100μm*

4.2.4   *Mechanical Properties*

Mechanical testing results showed significant differences among all the gels (Figure 4.3.4.1). Gel stiffness was inversely correlated with pore connectivity visualized from SEM images. It was found that gels with GCX occurring during or after PCT (CCX and Post24CX) augmented stiffness while Pre48CX and Pre24CX gels showed decreased stiffness.

Gel mechanical behaviors show significant changes in storage and loss modulus. Low frequency response indicated decreased stiffness with pre-PCT gelation GCX formation (Pre48CX, Pre24CX), and greater stiffness with GCX after PCT- induced gelation (Post24CX), when compared to control. (Figure 4.3.4.1)
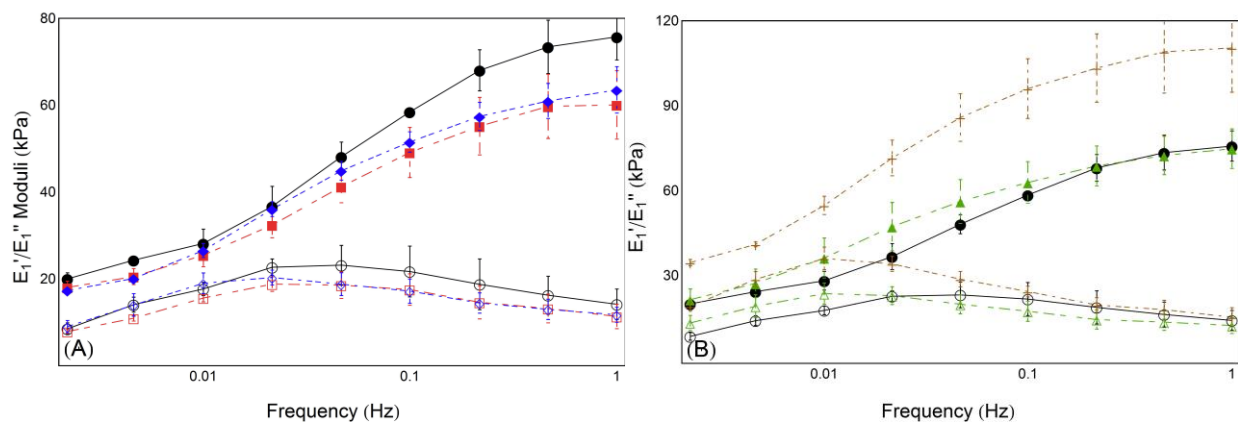
Figure 4.3.4.1- Storage (E_1') and loss ($E1$'') moduli as functions of frequency. Results in control gels indicate decreased overall stiffness at lower frequencies. Additionally, E_1'' appears lower than E_1' for all frequency values, and appears decreasing at similar or faster rate than E_1'. (A) Comparison of Control (n=3), Pre48CX (n=3) and Pre24CX (n=3) show decreased stiffness for both E_1' and E_1'' at all frequencies. (B) Post24CX (n=2) shows increased stiffness compared to Control, while CCX (n=4) shows lower transition frequency.

E_1' and E_1'' reveal typical viscoelastic response of gels, with lower and upper plateau regions at lower and higher frequencies, respectively, separated by a transition region. Values for E_1'' show similar results to E_1' across all samples when compared to control. Interestingly, E_1'' decreases with lower frequencies at a rate equal to or greater than that of E_1', which indicate that the material always acts as an elastic solid within the environmental constraints placed on the material.
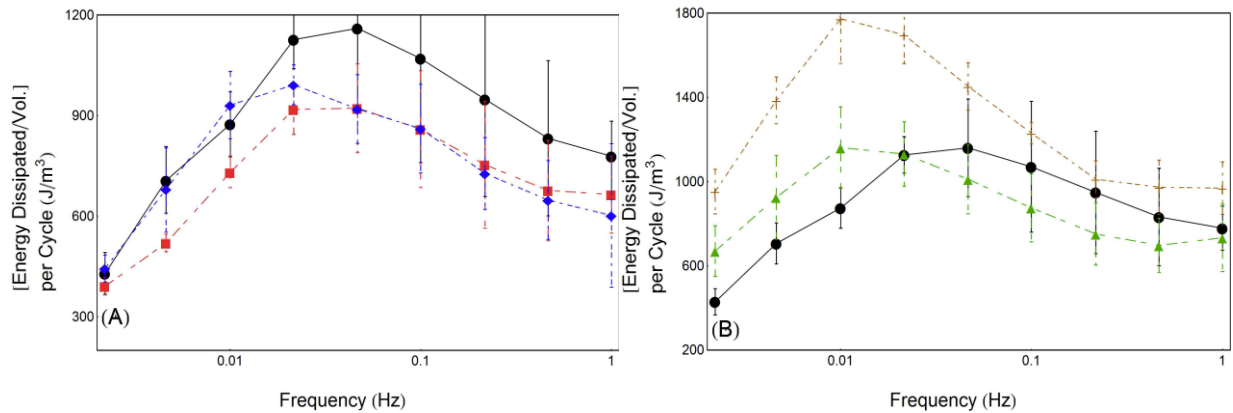
Figure 4.3.4.2- Energy dissipation per cycle was calculated from hysteresis curves, and plotted against frequency. (A) Comparisons of Control (n=3), Pre48CX (n=3), Pre24CX (n=3) show decreased energy dissipation in GCX crosslinked gels. (B) Comparisons of Control, CCX (n=4), and Post24CX (n=2) show increased energy dissipation from Post24CX gels, and peak shift to lower transition frequency.

Key: ●- Control; ■- Pre48CX; ◆- Pre24CX; ▲- CCX; + - Post24CX;"

Energy dissipation curves indicate significant energy loss at all frequencies for all gels. Gels with GCX pre-PCT gelation show decreased energy dissipation, while GCX after PCT shows much greater energy dissipation values. All energy dissipation values correspond well with E_1'' values (Figure 10).

Both Post24CX and CCX gels showed a distinct peak shift to lower transition frequency, also corresponding to shifts seen in E_1'.

4.3 Discussion

Herein, we show order of GCX formation with PCT-induced gelation through β-sheet crystallization affects SF hydrogel morphology, and resulting material properties with physiologic, high amplitude dynamic loading. Significant differences between sample loss and storage moduli are shown, which become greater at higher frequencies. GCX occurrence pre-PCT presents more fibrous morphology and decreased stiffness at higher frequencies. Occurrence of GCX during the PCT phase showed minimal effect. Alternately, GCX after PCT shows similar morphology, with increased stiffness at all frequencies. Furthermore, this stiffness response approximates gel response in different applications.

Silk fibroin which undergoes PCT-induced gelation forms highly hydrated, porous hydrogels,(Floren et al., 2012) through induction of β-sheet crystallization. All samples within this study correspond with this previous data, with stable, homogeneous, porous gels forming as seen in SEM and confocal microscopy data (Figures 4.3.3.2 & 4.3.4.1). Reported stiffness data ranges from 15-60 kPa for low applied strain rates (~0.3%/s), which corresponds with similar strain rates in our study (f=0.015 Hz). Additionally, FTIR spectra shows no significant changes between gels (Figure 4.3.2.4), indicating high levels of gel crystallinity between samples.(Floren et al., 2012; Hu et al., 2006, 2011) Covalent crosslinking before PCT leads to more fibrous morphology, and decreased stiffness response. The microstructure changes, taken in conjunction with changes in M_W distributions by GCX formation, suggest differences in nucleation rates among the gels. Previous studies in polymer formation indicate decreased nucleation times,(Krumme et al., 2004; Song et al., 2008) and changed morphology,(Emri and von Bernstorff, 2006; Krumme et al., 2004; Song et al., 2008) in bimodal polymer distributions. While previous studies most frequently indicate chemical crosslinking increases material stiffness,(Bi et al., 2011; Madhavan et al., 2010; Sundararaghavan et al., 2008) and morphology change,(Bi et al., 2011)

testing is performed in the linear range. The fibrous morphology and greater pore connectivity may be responsible for decreased E_1' values.(Hollister, 2005; Mak, 1986) This decreased stiffness would also account for decreased energy dissipation, due to minimal elastic storage, and corresponds with decreased E_1'' values.

Covalent crosslinking after PCT (PostCX) leads to much greater stiffness response, while maintaining similar morphology to Control. While GCX occurring post-gelation has been shown previously, molecular structure during GCX treatment was not fully crystallized,(Xiao et al., 2012) possibly allowing more amorphous chain movement. Furthermore, β-sheet content was increased after GCX formation,(Xiao et al., 2012) confusing mechanical response between GCX and higher crystallinity.

Taken together, results from ninhydrin assay, fluorescence emission, and physical appearance of gels suggest that genipin bonding to fibroin molecules occurs at low efficiency. After PCT-induced crystallization, amorphous chain groups are immobile, making primary amines less available for bonding, thereby diminishing GCX formation. Genipin bonding to a single fibroin molecule would decrease primary amine content as measured by ninhydrin (Figure 4.3.2.3),(Butler et al., 2003; Foss et al., 2013; Silva et al., 2008b) while fluorescence (Figure 4.3.2.2) would most greatly increase with genipin dimer bridge formation due to additional π-bonds within the bicyclic fused ring structure.(Mi et al., 2005; Sundararaghavan et al., 2008; Wang et al., 2013a) Therefore, mismatch between these two data sets indicates partial, but not complete, GCX formation in Post24CX gels. The first reaction to occur in genipin bonding to a primary amine group is the opening of the dihydropyran ring within the fused ring structure, thereby causing one additional π-bond to form.(Butler et al., 2003) Therefore, fluorescence would increase without creating blue pigmentation of full GCX formation. Of the two-part genipin reaction, this was shown to occur first,(Butler et al., 2003) and would increase fluorescence, thereby creating a disparity between fluorescence and pigmentation. This may explain the similarity in fluorescence, but disparity in coloration between Pre24CX and Post24CX gels.

Stiffness response in Post24CX samples showed significant differences. GCX formation after gelation would cause partial formation of a polymer network within the amorphous region, reducing molecular motion, and increasing stiffness response. This increased stiffness response may also be seen in increased E_1'' values, and corresponding increased energy dissipation as seen in Figure 10. Peak shifts towards longer relaxation times (1/f), present in both CCX and Post24CX energy dissipation and first harmonic moduli plots, may result from amorphous network crosslinking.(Glatz-Reichenbach et al., 1994)

Previously, genipin crosslinking has been studied with fibroin, though order between GCX and gelation was not examined.(Motta et al., 2011; Silva et al., 2008b; Sun et al., 2014; Wang et al., 2013a; Xiao et al., 2012) Dynamic mechanical response with physiologic, nonlinear strain was also not examined within these previous studies. Large compressive strain deformation amplifies stiffness response from morphological structure(Hyun et al., 2011; Lockett, 1972) and permeability within poroviscoelastic solids.(Mak, 1986) This may be derived from Poisson's ratio causing volumetric changes between the solid and fluid phases of the material, resulting in fluid flux, and corresponding pressure from fluid drag (Supporting Material S1). Application of nonlinear strain would therefore highlight morphological changes resulting in higher permeability, and material response under physiologic strains.

Material tunability allows broader application, and may improve scaffold design. Morphology plays an important role in cell activity through cell attachment(Arnold et al., 2004) and nutrient transport.(Drury and Mooney, 2003; Peppas et al., 2000; Vepari and Kaplan, 2007) Additionally, both micro-structure(Discher, 2005; Hollister, 2005; Saha et al., 2008) and connectivity(Hollister, 2005; Mak, 1986) affect matrix stiffness, an important contributor to cell interaction and activity.(Guo et al., 2006; Ingber, 2003; Wang et al., 2000) Material stiffness and its response to applied strain additionally play a role in cell differentiation.(Engler et al., 2006; Guilak et al., 2009; Sen et al., 2008; Simmons et al., 2003; Wingate et al., 2012) Herein, we show that stiffness response within the frequency spectrum may be controlled by changing order of GCX formation and PCT-induced gelation in SF hydrogels.

4.4 Conclusions

Order of GCX and PCT during formation of SF hydrogels have significant effects, and are capable of 'tuning' gel microstructure. Through alteration of both chemical (GCX) and physical (PCT) crosslinking, we may affect either the viscoelastic range, or overall stiffness of the material.

GCX formation before PCT results in decreased stiffness response at higher frequencies due to greater pore connectivity.(Hollister, 2005; Mak, 1986) (figure 4.3.3.3) Underlying cause is probably greater skewing and spread of SF molecular weight distribution (figure 4.3.2.1) before PCT, leading to morphological changes.(Emri and von Bernstorff, 2006; Krumme et al., 2004; Song et al., 2008) In comparison to Control, microstructure is most responsible for hydrogel stiffness response, with both Pre48CX and Pre24CX gels showing decreased E_1' and E_1'' values. Here we illustrate GCX pre-PCT gelation alters microstructure, with minimal molecular structure changes.

GCX formation after PCT causes anchoring of amorphous SF entanglements, causing much greater stiffness response at all loading frequencies. Increased stiffness occurred in Post24CX gels compared to control, (Figure 4.3.4.2) across all frequency values, for both E_1' and E_1''. Visually, SEM images of Post24CX indicated the greatest similarity with control gels, indicating that GCX augments stiffness of the control molecular and morphology structures. Though gels with GCX formation pre-PCT show much higher crosslinking concentration, GCX after entanglement would create polymer networks within the amorphous region of the fibroin. Here we see that microstructure is similarly formed compared to Control, but with major changes to molecular mechanics within the material.

ACKNOWLEDGMENT

ABBREVIATIONS

CCX, Gels with concurrent genipin crosslinking with gelation; DI, Deionized Water; LAOS, Large Amplitude Oscillatory Strain; E_1', First Harmonic Storage Modulus; E_1'', First Harmonic Loss Modulus; E^*, Complex Modulus; FTIR, Fourier-Transform Infrared Spectroscopy; GCX, Genipin crosslink; GPC, Gel Permeation Chromatography; PCT, High Pressure Carbon Dioxide Treatment; Pre48CX, Gels with genipin crosslinking 48 hours pre-gelation; Pre24CX, Gels with genipin crosslinking 24 hours pre-gelation; Post24CX, Gels with 24 hours of genipin crosslinking after gelation; RP-HPLC, Reverse Phases- High Performance Liquid Chromatography; SEM, Scanning Electron Microscopy;

5 Effect of Arterial Viscoelasticity and Stiffness on Hemodynamics

Time-dependent arterial wall property is an important but difficult topic in vascular mechanics and health. Arterial hysteresis curves formed through the cardiac cycle have been associated with arterial health. However, the cause-effect relationship between time-dependent mechanical properties of the arterial wall and hemodynamics, in particular the viscous contribution alone to arterial hemodynamics, remain elusive and challenging. Herein, we have shown comparisons between elastic (E''/E' <0.06) and highly viscoelastic (E''/E' = 0.45) tube conduits, in terms of their capability of altering pulsatile flow profile, wall shear and energy level. The tube conduits were made from varying ratio of vinyl-terminated and methyl-terminated poly(dimethylsiloxane), and were fit in a mimetic circulatory system with high accuracy measurements of waveform changes in flow, pressure and strain. Results indicated that attenuated distension waveforms in viscoelastic conduits, when compared to elastic conduits, resulted in 11% greater cross-sectional area throughout a mimetic cardiac cycle. In response to changing wall mechanics in viscoelastic conduits, pressure and volumetric flow waves respectively decreased by 3.9% and 6% in the peak-to-peak amplitude. The change in conduit strain might result from frequency-dependence of the viscoelastic materials. More importantly, diameter strain and volumetric flow showed greater waveform temporal alignment in viscoelastic conduits due to attenuation of both waveforms, resulting in 25% decrease in detrimental oscillation of wall shear stress. These changes in flow dynamics, due to the viscous component of viscoelastic conduit, might have beneficial influence to cell mechanotransduction to promote healthy arterial response.

The importance of viscoelasticity in blood vessels may be best illustrated by comparison of healthy to diseased states and to treated states. Viscoelastic properties of arteries started to become a metric of health,(Liu et al., 2015; Wang et al., 2013c), coincided with application of time-dependent materials in arterial replacements,(Zhao, 2014; Zhao et al., 2014) such as vascular graft.(Nagiah et al., 2015; Neufurth et al., 2015) During the progression of arterial disease, a well-known phenomenon is increased pressure modulus (E_P) of the artery.(Beaussier et al., 2011; Huynh et al., 2011) What remains unclear is the importance of viscoelastic changes in arterial properties to the disease progression, though recent studies showed significant decrease in hysteresis loops during arterial diseases.(Wang et al., 2013c) A similar question also applies to arterial disease treatments such as arterial grafting. In studies comparing the human femoral artery to graft materials including cryogenically preserved artery, saphenous vein, and ePTFE graft that lacks arterial-like viscoelasticity, the viscoelastic response of arterial grafts correlated with the success rate. (Bia et al., 2006; Deutsch et al., 2009; Owens, 2010) While viscoelastic, tough biomaterials are now being explored in vascular grafting, the question on whether increasing viscous response of the material could improve mechanical and biological responses remain largely unexplored.(Neufurth et al., 2015). Therefore, the interaction between viscoelastic properties of blood vessels and flow dynamics is important to understanding of vascular physiology and design of vascular implant, but remains largely unexplored.

Effects of arterial wall time-dependent properties on hemodynamics have been a difficult question for the past 60 years. Branching of the arterial tree, arterial integration into surrounding tissues, and hierarchical tissue structure of the arterial wall contribute to the complexity of measuring such effects *in situ* or *ex vivo*. Arterial tissue consists of multiple, anisotropic layers, with varying time-dependent stiffness responses, and differing roles in arterial loading.(Holzapfel, 2004, 2005; Wagenseil and Mecham, 2009) Stress and strain of the layers additionally changes with arterial geometry,(Hunter et al., 2010) as well as boundary conditions created by tethering of the arterial adventitia to the surrounding tissue.(O'Rourke et al., 2011) Additionally, healthy, native arteries express a frequency-dependent

viscoelastic response, with measurable hysteresis, and a viscoelastic ratio (E''/E') of approximately 0.1-0.15. (Bergel, 1961; Bia et al., 2006). Muscular arteries such as femoral and carotid were shown to provide protective damping for the circulatory system, through significant strain and hysteresis.(Armentano et al., 2014; Bia et al., 2006; Giannattasio et al., 2008; Wang et al., 2013b) Though important, measurements taken *in situ* or *ex vivo* do not provide the cause-effect relationship between time-dependent mechanical properties of the arterial wall and hemodynamics.

In computational and experimental models, viscoelasticity has been shown to attenuate pulsatile flow waves over long distances and during exercise.(Alastruey et al., 2011, 2012; Bessems et al., 2008; Raghu et al., 2011; Taylor, 1959; Wang et al., 2013b, 2016) Of the previous works that experimentally validated flow models, most did not independently characterize the tube material properties, (Bessems et al., 2008; Taylor, 1959) and all used materials with viscous responses that were only a slight fraction (tanδ ~ 0.02) of the overall stiffness response. (Bessems et al., 2008; Taylor, 1959; Wang et al., 2016) These studies also failed to experimentally separate the contributions of viscous and elastic components to hemodynamics. Additionally, though pressure wave attenuation was studied previously, the time-lag of the wall strain due to viscoelastic material properties, as well as its coupling with the flow waveforms has not been well studied.(Bessems et al., 2008; Taylor, 1959; Wang et al., 2016) As the wall shear stress, a primary signal to vascular endothelial cells and vascular health, (Chien, 2006; Chiu and Chien, 2011; Elliott et al., 2015; Scott et al., 2013), is determined by volumetric flow and cross-sectional area, the phasic alignment of material strain and volumetric flow is important to determine impact of viscoelastic materials on maintaining healthy hemodynamics. However, previous studies have seldom examined that aspect.

The present study has examined the effects of lumen viscoelasticity on flow dynamics, including flow and pressure waveforms as well as wall shear stress at both upstream and downstream. Different from previous studies that illustrated wave attenuation within elastic tubes relying on the use of computational methods for the solid-fluid interaction, we have constructed tube materials with arterial-like compliance

and varying viscoelasticity, which allow for greater insight into the fluid/structure interface and materials-induced flow alterations in our experimental model that incorporates high-performance flow and pressure sensors. The viscous and elastic material properties may be separated and compared, with the advent of materials in which overall stiffness and ratio of viscous to elastic response (E''/E') may be controlled,(Kalcioglu et al., 2013; Mrozek et al., 2011). Understanding the interplay between flow dynamics and viscoelastic tubing may aid in establishing viscous wall response of arterial tissue as an important signal in arterial health, and as an important parameter in graft design and development.

5.1   Material design overview

Understanding the importance of viscoelasticity in vascular grafting may be best illustrated by comparison of healthy to disease states. In comparison to disease states, clinical measures such as pressure modulus (E_P), distensibility, and compliance, indicate increased arterial stiffness associated with arterial disease.(Beaussier et al., 2011; Huynh et al., 2011; Wang et al., 2013c)

	Elastic	Viscoelastic	Citations
Non-Compliant	E_P*=800-1200 mmHg; tan(δ)=0 (Perfectly Elastic)	E_P*=800-1200 mmHg; tan(δ)> 0.5 (Highly Viscoelastic)	(Farrar et al. 1982; Buntin and Silver 1990; Nagai et al. 1999; Beaussier et al. 2011; Tan et al. 2014)

Table 5.1- Material parameters guidelines for proposed conduit design. Carotid artery stiffness ranges are listed above with sources cited. Proposed viscoelasticity of the fabricated conduits are listed as tan(δ) relating directly to viscoelastic to elastic ratios.

Viscoelasticity, as measured by the ratio of viscous to elastic response (tan(δ)=E''/E'), was measured in healthy femoral, carotid, and coronary arteries, ranging between 0.1-0.15, within the frequency range of 1-10 Hz.(Bergel, 1961; Bia et al., 2006; Gow and Taylor, 1968; Gow et al., 1974) In the aged and diseased, hysteresis area has shown a marked decline,(Giannattasio et al., 2008; Wang et al., 2013c) supported by decreased tan(δ). Additionally, comparison of graft viscoelasticity in the few examples available indicates materials such as ePTFE, PCL, and PLA have negligible wall damping capabilities. Therefore, vascular health dependence on viscoelasticity may be compared to importance of compliance by varying tan(δ) with graft stiffness. Proposed graft models may be seen in table 5.1. Additionally, flow parameters will be measured to compare more clinical values, such as E_P dynamic compliance, inlet and outlet pressures, mean volumetric flow, and pulsatility index (PI). This will aid in providing a mechanism for cell response to the disease state, (IH and vascular fibrosis) and a mechanism for reduced disease response. Reduction in PI or pressure wave attenuation may then be attributed to wall damping through the mechanical energy of flow equation.

5.1   Materials and Methods

Material used to cater both stiffness (E*) and viscoelasticity ($\tan(\delta)$)) is poly(dimethyl siloxane) (PDMS) swollen gels, previously described in the literature.(Kalcioglu et al., 2013; Mrozek et al., 2011) Different termination groups within PDMS are separated into the elastic network (vinyl-terminated) and swelling solvent (methyl-terminated). Vinyl-terminated PDMS (v-PDMS) is crosslinked through a tetrafunctional vinyl crosslinker, which additionally prevents methyl-terminated PDMS (m-PDMS) from bonding to the network. The elastic network stiffness may be catered both through crosslink density, and chain entanglements (see fig. 5.2.1). Solvent (m-PDMS) increases viscous dissipation within the material, which may be controlled by m-PDMS molecular weight, and additionally contributes to stiffness through entanglements. A diagram of the material molecular structure may be seen in figure below.
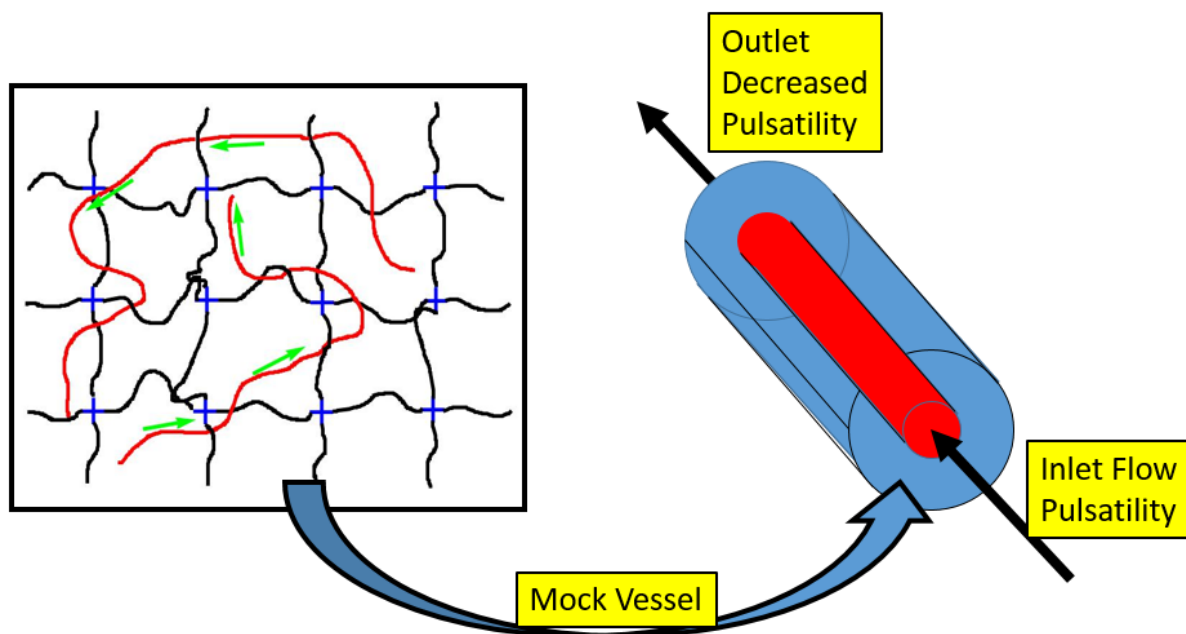
Figure 5.2.1– Diagram of the molecular structure of swollen poly(dimethylsiloxane). Molecular structures are color-coded: tetrafunctional crosslinker (blue), elastic v-PDMS (black), solvent m-PDMS (red). Viscous flow due to molecular movement is indicated by the green arrows.

5.1.1 Material Fabrication

Swollen gels were fabricated through methods outlined previously in the literature. (Kalcioglu et al., 2013; Mrozek et al., 2011) Briefly, vinyl-terminated PDMS (M_W : 108 kDa) were donated by Siltech Corporation (Toronto, ON, Canada). Methyl-terminated PDMS (Viscosity: 500 CSt and 1M CSt) was purchased from Clearco (Clearco Products Company Incorporated, Willow Grove, PA). Tetrakis(dimethylsiloxy)silane and platinum catalyst (Pt(0)-2,4,6,8-tetramethyl-2,4,6,8-tetravinylcyclotetrasiloxane) were both also purchased from Sigma-Aldrich. First, v-PDMS and m-PDMS were mixed by differing weight percentage at room temperature. Crosslinker was then added at a stoichiometric ratio of 4:1 crosslinker functional group to vinyl chain termination, and mechanically mixed for 15 minutes. Lastly, platinum catalyst was added at a concentration of 800 ppm, and mechanically mixed for ten minutes. PDMS was placed in vacuum and degassed until all visible gas bubbles were removed. Material was then crosslinked in vacuum at 80°C for 72 hours.

Two groups of samples were created, elastic (58.8% 500 CSt m-PDMS: 108 kDa v-PDMS) and viscoelastic (70% 1M CSt m-PDMS: 108 kDa v-PDMS). Because low molecular weight solvent is below the entanglement weight of PDMS, it has little contribution to the stiffness or viscous response. It may also be treated as a simple theta solvent within the swollen gel, (Kalcioglu et al., 2013; Mrozek et al., 2011) which will have a low viscous effect. This additionally allows v-PDMS/m-PDMS fraction (φ) to be used in determining the material stiffness ($|G^*| \propto \varphi^{2.3}$). Elastic material stiffness may be easily catered to match viscoelastic PDMS material stiffness response.

5.1.2 Material Characterization

Material mechanical properties were evaluated using the ARES TA rheometer (TA Instruments, New Castle, DE). Contact force was brought to 0.5 N, and material tested at room temperature, in ambient conditions. Three tests were completed: strain sweep, stress relaxation, and frequency sweep. Strain sweep was performed at a frequency of 1 Hz, with increasing strain over the range of 0.1%-50% strain,

indicating strain softening occurrence at approximately 10%. Based on strain sweep results, stress relaxation was measured at 1%, 5%, and 10% strain, and final modulus values recorded as steady-state moduli. Frequency sweep tests were also performed over the range 0.1 Hz-40 Hz, and complex modulus recorded.

Elastic PDMS was further evaluated using the TA Q800 rheometer (TA Instruments, New Castle, DE) dynamic mechanical analysis (DMA). Briefly, samples were placed in 0.01 newtons of tension within the DMA, and cycled at 1% strain at 1 Hz for six minutes. Final modulus was recorded as the average over this time period.

5.2   Flow dynamics

5.2.1   Fluid/Material Coupling

Coupling of the fluid pressure and the material frequency response may be accomplished through the assumption of a mathematically linear relationship within the frequency domain. Complex waves may be separated through Fourier Transform of the given waveform, and application to known material frequency dependence. This separates the complex waveform into a summation of sine waves, with discrete amplitude and phase shift, represented by a complex number. This may then be coupled to material data consisting of a complex modulus, and reverted to the time domain:

$$\boldsymbol{\varepsilon(t) = \mathcal{F}^{-1}\left\{\frac{\mathcal{F}\{P\}}{3\,G^*}\right\} = \mathcal{F}^{-1}\left\{\frac{\mathcal{F}\{P\}}{3|G^*|exp(-i\theta)}\right\}} \qquad (5.2.1)$$

This allows us to examine the dominant frequency range in considering material testing. Below is the frequency spectrum of the waveform created by the pulsatile pump. As can be seen, the dominant frequency is 1 Hz, and the harmonics created by the wave extend out to 9 Hz, which is typical of cardiac waveforms.(O'Rourke et al., 2011) This is again within the range measured by the frequency sweep of the material (0.1-40 Hz).

102
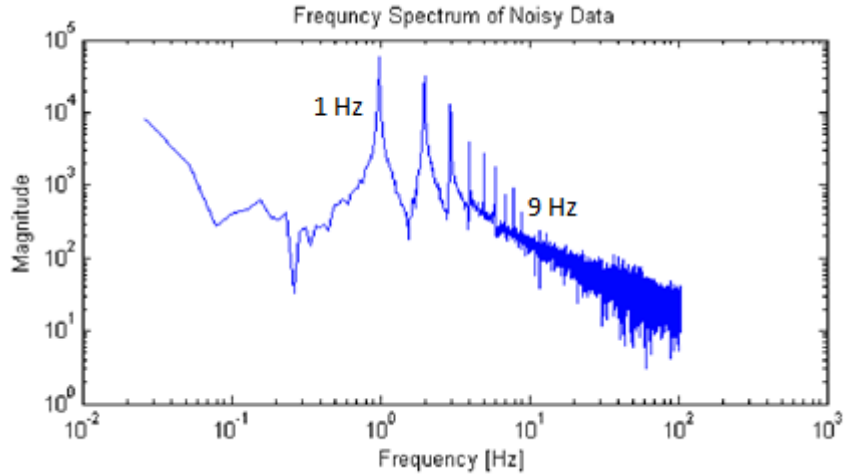
Figure 5.3.1.1- Frequency spectrum of Harvard Apparatus pump. The largest peak is the dominant

frequency of 1 Hz, with harmonics up to 9 Hz. This is well within the range of measurements seen in

figure 5.2.2.3.

5.2.2   Conduit Design

To test flow dynamics, the fluid body must be recreated, and therefore only the vessel lumen

mechanics must be mimicked. Due to the constraints in section 4.1, a simple design is necessary to

maintain material viscosity, while also controlling stiffness. This becomes simpler in designing a rigid

sheath which prevents radial strain. Therefore, conduit design incorporates rigid exterior wall of

polypropylene (PP). Strain response to this can be modeled through the equation for wall motion in thick-

walled cylinders:

$$\mathbf{u_r}(r) = \frac{1-v}{3\,G^*}\frac{(r_i^2 p_i - r_o^2 p_o)r}{r_o^2 - r_i^2} + \frac{1+v}{3\,G^*}\frac{(p_i - p_o)r_i^2 r_o^2}{(r_o^2 - r_i^2)r} \qquad (5.2.2)$$

Where r_i and r_o are the inner and outer radii, respectively, r is the radial coordinate, and p_i and p_o are

the inner and outer pressures, respectively. Material properties are both the shear modulus G^* and the

103

Poisson's ratio v. By setting $u_r(r_o) = 0$ and v to 0.5 (for PDMS), we may then solve for p_o in terms of p_i, r_i, and r_o, and subsequently solve for $u_r(r_i)$:

$$u_r(P) = \mathcal{F}^{-1}\left\{\frac{\mathcal{F}\{P\}}{3\,G^*}\right\}\frac{r_i(r_i^2-r_o^2)^2}{2(r_o^2-r_i^2)(r_o^2+3r_i^2)} \qquad (5.2.2.1)$$

We then have a geometric factor as a relationship between the inner (r_i) and outer (r_o) radii on the right side of the equation, as well as our pressure/modulus relationship ($\mathcal{F}^{-1}\left\{\frac{\mathcal{F}\{P\}}{3\,G^*}\right\}$). We may then use target material properties (as described in Table 5.1) to project diameter strain from a pressure wave cycle. In the projected diameter strain from our relationship, we can see a more gradual return to the strain minimum, while maintaining similar peak-to-peak amplitude. Increasing the total cross-sectional area throughout the cycle would decrease peak pressure and flow velocity, due to decreased impedance.
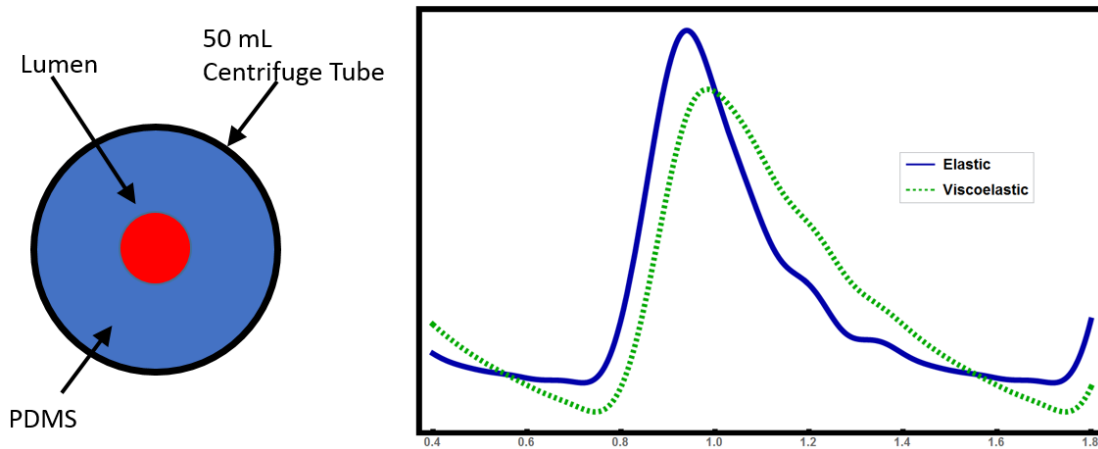
Figure 5.3.2- Mock vessel design diagrammed on the left, with modeled lumen radius response on the right. The lumen radius was modeled by coupling pressure and material properties for both viscoelastic materials (PDMS-70%(108k-1M CSt): green, dashed) and elastic materials (PDMS-58.8%(108k-500 CSt): blue, solid).

5.2.3   Fabrication of the Tube Conduit

To fabricate the tube conduit, an inner lumen was necessary to create within the material structure to allow the passage of flow. Therefore, a polymethylmethacrylate (PMMA) rod was inserted into the material before curing to allow the PDMS material to form around a lumen structure. To prevent collapse of the material upon removing the PMMA rod, an inner elastic layer was created to reduce viscous shear on the rod during removal. To create this elastic layer, pure v-PDMS material was mixed, as described in section 5.2.1, with the change of a stoichiometric ratio of vinyl cross-linker to v-PDMS end group of 3:1. This v-PDMS material was mixed in a 1:1 ratio by volume of n-Heptane to decrease solution viscosity. Rods were then drip-coated and hung to dry in vacuum for one hour to allow n-Heptane evaporation. After adequate evaporation time, v-PDMS was then cured for one hour at 50 °C, creating a fully cured elastic layer approximately 70-100 microns in thickness.

Viscoelastic (PDMS-70%(108k-1M CSt)) and elastic (PDMS-58.8%(108k-500 CSt)) conduit material was fabricated as described previously in section 5.2.1. Material was placed into PP 50 mL tubes, with material added equaling 45 grams. Remaining air was removed from the material by centrifugation of the tubes for 20 minutes. Coated PMMA rods were then inserted into the material, and centered using a PDMS washer. Conduits were then cured at 70 °C for 72 hours, and removed to allow cooling at room-temperature. Bottom PP material was removed, and PDMS was capped using v-PDMS material. Rods were then removed using ethanol as a lubricant, and lumens were left intact.

To finalize conduit construction, 3/8" PP luer connections were inserted in lumen ends, and again sealed using v-PDMS material. Rigid outer diameter material of the PP centrifuge tube was then sectioned along the outer circumference, and remaining rigid material at the conduit terminals were removed to allow longitudinal travel of the PDMS material while undergoing radial strain.

5.2.4   Applied Flow

5.2.4.1   Fluid Parameters

Flow was tested using deionized water within a benchtop flow circuit, with fluid viscosity assumed to be equivalent to water (8.9×10^{-4} Pa•s). Pulsatile flow was applied through a pulsatile flow pump (Harvard Apparatus, Holliston, MA), which controls volumetric flow rate through applying a driving piston. Complex, pulsatile pressure and flow are then applied and controlled through connecting silicone tubing of 3/8" inner diameter. Pulsatile pressure range and flow pulsatility are controlled through the introduction of a compliance chamber before the mock vessel, introducing a Windkessel pressure damping, as described previously.(Scott-Drechsel et al., 2012) Flow response under two pressure ranges were recorded: 30 mmHg (LPF) and 70 mmHg (HPF). Pressure ranges were changed through altering compliance chamber levels. Compliance chamber levels were normalized for each pressure range using Tygon B-44-4X tubing (Saint Gobain S.A., Courbevoie, France) as an effectively rigid conduit, applying 4.67 cc/s flow rate at a frequency of 1 Hz. Compliance chamber levels were maintained as a control variable during testing to examine conduit effect on pressure.

Volumetric flow rate was calculated through the intended applied wall shear stress (*WSS*) of 1.0 Pa, using the equation for laminar shear at the wall of a pipe:

$$\boldsymbol{WSS} = -\boldsymbol{\mu}\frac{\partial \vec{\boldsymbol{u}}}{\partial \boldsymbol{r}} = \boldsymbol{\mu}\frac{3\,\vec{\boldsymbol{Q}}}{\boldsymbol{\pi}\,\boldsymbol{R^3}} \rightarrow \vec{\boldsymbol{Q}} = \frac{\boldsymbol{WSS}\,\boldsymbol{\pi}\,\boldsymbol{R^3}}{3\,\boldsymbol{\mu}} \qquad\qquad (5.2.4.1\ )$$

Here, μ is the dynamic viscosity, u is the velocity, r is the location along the radial axis, Q is the volumetric flow, and R is the lumen radius. Therefore, assuming laminar, fully developed flow, a radius of 2.65 mm, and viscosity of 4×10^{-3} Pa•s (viscosity of blood), resulting volumetric flow (Q) is 4.67 cc/s at a frequency of 1 Hz. Flow rate, frequency, and *WSS* all match physiological levels as measured in large animal models of common carotid arteries (CCA) described in the literature.(Byrom et al., 2010) This is lower than previously reported *WSS* in EC mechanotransduction studies,(Elliott et al., 2015; Tan et al.,

2014) but reduces strain on the flow system while more closely matching large animal studies.(Byrom et al., 2010)

5.2.4.2 *Fluid Measurement*

The test bench fluid circuit was designed to reduce wave reflection and allow for pressure and volumetric flow measures through multiple cycles. Pressure sensors were purchased from Omega Engineering (PX209-015G15V, Omega Engineering Inc., Norwalk, CT) and fitted with nylon (polyamine) tee-joints. Pressure (P) sensors were placed nearest to conduit terminals to reduce head loss from connector tubing. Volumetric flow rate was measured concurrently with pressure (Sonoflow CO 55/060, Sonotec USA, Islandia, NY).

Due to constraints of the flow meter, smaller connective tubing diameter was required at the point of measurement, with inner diameter of 1/16". To avoid wave reflection and increased impedance volumetric flow was measured in parallel to the conduit, connected through nylon tee-junctions of 3/8" diameter. The measured flow waveform perpendicular to the flow is not directly proportional to the flow in line with the conduit, due to the tee-junction head loss, and impedance change resulting from different diameter of the connection tubing and Q-sensor.(O'Rourke et al., 2011; Paritosh and others, 2007) Measured variation in flow change due to the tee is discussed further in appendix A2. Volumetric flow rate is minimally affected by head pressures, but is most greatly reduced and attenuated by viscous energy loss, therefore inlet Q-sensor was placed before the inlet P-sensor and the outlet Q-sensor was placed after the outlet *P*-sensor.

Pressure and volumetric flow data was sampled at 225 Hz and recorded on a real-time target (RT-Target) board (sb-RIO 9392, National Instruments, Austin, TX), which then packaged and sent data to a personal computer central processing unit (CPU) (Dell Inc., Round Rock, TX). Volumetric flow signal passed through a resistor/capacitor low-pass signal filter, with a cutoff frequency of 22 Hz. Upon startup,

the RT-Target internal clock was synchronized with the CPU clock. Resulting data was time-stamped during recording on the RT-Target before being transferred to the CPU and recorded in a text file.

5.2.4.3 *Conduit Strain Measurement*

Due to the optical transparency of the conduit material, PDMS, conduit distension was measured by color, high speed CCD camera (Basler Ace, Ahrensburg, Germany). Video imaging occurred concurrently with pressure and flow recording. Images were captured at length resolution of 17.6 microns/pixel and time resolution of 80 Hz, recorded by PXI board (National Instruments, Austin, TX). Frames were then time-stamped by the CPU, and packaged into audio video interleave (AVI) files.

Fluid used was DI with red food coloring, and backlit using a white LED array. This combination of red fluid coloration backlit to prevent light reflections within the conduit allowed for defined conduit edges within the images.

5.2.5 *Data Analysis*

5.2.5.1 *Image Analysis*

Recorded AVI files were converted into graphics interchange format (GIF), imported into image analysis software written in-house in Mathematica (Wolfram Research, Champaign, IL). Analysis software filtered images by red coloration, binarized these images to clearly define lumen edge, and then measured diameter perpendicular to the lumen axis. Average lumen diameter within a single frame was then paired with the corresponding time-stamp and recorded.

5.2.5.2 *Data Smoothing and Combination*

All recorded waveforms underwent discrete Fourier transforms (DFT), and magnitude and phases were recorded. To remove time disparities from different sampling frequencies within a single data set of P_{In}, P_{Out}, Q_{In}, Q_{Out}, and diameter (D), and further error from irregularities in recording intervals, linear interpolation between points was performed to create regular time intervals before DFT. Resulting Fourier

harmonic phase values were normalized to their corresponding P_{In} phase, to allow for comparison between waveforms. Resulting harmonic moduli and phases were averaged and combined into 1-dimensional functions for comparison of the form:

$$g(x,t) = C_0 + \sum_{f=1}^{N}|C_f|Exp\left[-i\left(2\pi f\left(t - \frac{x}{c_f}\right) - \varphi_f\right)\right] \qquad (5.2.5.1)$$

Where C_f is the modulus of the complex Fourier harmonic constant, c_f is the wave speed of the harmonic, and φ_f is the phase shift of the corresponding harmonic.

Before DFT, area under Q curves were determined to estimate total volume during the recorded data cycle. Both Q_{In} and Q_{Out} values were normalized to the area to reduce variance from the sensor between data recordings. This maintained the conservation of mass within the system between inlet and outlet.

5.2.5.3 *System Metrics*

Previous metrics have been discussed in earlier sections. To clarify we will repeat the method of these clinical metrics in this section. Conduit stiffness is initially characterized by the pressure modulus (E_P), a clinical measure in the body to determine arterial stiffness. Here we refer E_P as the quotient of peak-to-peak pressure range (ΔP) and strain range ($\Delta\varepsilon_R$) over the loading cycle, using the mean value between pressure inlet (ΔP_{In}) and pressure outlet (ΔP_{Out}) to account for head loss:

$$E_P = \frac{\Delta P}{\Delta\varepsilon_R} = \frac{Mean(\Delta P_{In},\Delta P_{Out})}{\Delta\varepsilon_R} \qquad (5.2.5.2)$$

Additionally, wave speeds were calculated from locating the wave foot by locating the maximum of the double derivative of the waveform with respect to time. This locates the acceleration of the waveform,

and initial base of the recorded waveform. Wave speed (c) was then calculated as the length (x) between

sensors divided by the time (t) between inlet and outlet waveforms for each harmonic:

$$c = \frac{\Delta x}{\Delta t} = \frac{x_{Out} - x_{In}}{t_{Out} - t_{In}} = \omega \frac{x_{Out} - x_{In}}{\varphi_{Out} - \varphi_{In}} \qquad (\,5.2.5.3\,)$$

Wave speed values become necessary for the governing equations listed in the subsequent section.

5.2.5.4   *Governing Equations*

To examine relationships between the conduit material properties and hemodynamics, previously

established mathematical relationships must be defined. These relationships range from clinically

measured values such as the pulsatility index (PI) and wave speed (c), to values such as the mechanical

energy of flow and impedance (Z) of the conduit.

Coupling material strain to pressure and flow in the system begins with determining the relationship

between conduit strain and conduit impedance. A simple theoretical relationship of impedance without

wave reflections will be quantified to better highlight coupling of diameter to upstream waveforms.

Impedance is defined as the summation of resistance (R) and inductance (L):

$$Z = R + i\omega L = \frac{i\omega\rho}{\pi R^2}\left(1 - \frac{2J_1\!\left(\alpha\, i^{\frac{3}{2}}\right)}{\alpha\, i^{\frac{3}{2}} J_0\!\left(\alpha\, i^{\frac{3}{2}}\right)}\right)^{-1} \qquad (\,5.2.5.4\,)$$

Where ω is the frequency, ρ is the density, R is the lumen radius, α is the Womersley number, and J_0 are

zero order Bessel functions of the first kind. The Bessel functions are simply mathematical relationships

derived by Womersley (Womersley, 1955) for pulsatile flow in a conduit, and will not change between

conduit types or applied waveforms. Additionally, fluid density and frequency will not change between

conduit material types, therefore Womersley number and $i\omega\rho$ term may be dropped. This may therefore be simplified to relate impedence only to radius:

$$Z \propto \frac{1}{R_0^2 \lambda(t)^2} \propto \frac{1}{\varepsilon_R(t)^2} \qquad (5.2.5.5)$$

Where R_0 is the initial radius, λ is the stretch ratio, and ε_R is the radial strain. From this we may further compare conduit strain with upstream pressure and flow through the relation of conduit radius and frequency.

Average cross-sectional area (ε_r^2) value was estimated through integrating radial strain over the cycle using a Riemann sum, using time intervals below the image sampling frequency. This allows a comparison between impedances over the flow cycle.

To couple the material strain to the flow, it is necessary to reduce the relationship through the mechanical energy of flow equation. This is specifically examined because the mechanical energy directly relates to PI, as previously specified in section 3.2.7.

$$\frac{\rho}{2}\frac{D}{Dt}(u^2) = \rho gh + \nabla(u \cdot \sigma) + (\nabla \cdot u)P - \varphi \qquad (5.2.5.6)$$

Where the material derivative of the kinetic energy (u^2) may be equated with the gravitational potential (g), volumetric potential (P), viscous loss (φ), and applied stress (σ) on the fluid. Within the experiment test bench neither height nor fluid viscosity changes, and we may therefore eliminate the gravitational potential g. The equation may then be simplified to:

$$\frac{\rho}{2}\left[\frac{\partial}{\partial t}(u^2) + (u \cdot \nabla)u^2\right] = \nabla(u \cdot \sigma) + (\nabla \cdot u)P - \varphi \qquad (5.2.5.7)$$

Here we can see that time and spatial derivatives of the kinetic energy may be directly related to the applied stress on the system (σ), potential energy (P) within the volume, and a summation of viscous loss throughout the volume (φ). Therefore, hysteresis resulting from the material strain would reduce applied stress and returned energy as the lumen contracts. Energy loss from hysteresis of the material would therefore reduce kinetic energy on the left side of equation 5.3, as well as reducing pressure on the right side of the equation.

By isolating both the time-derivative and spatial-derivative in the mechanical energy of flow, we may directly relate this to PI and wave speed, respectively:

$$\int_0^{t_{max}} \frac{\partial}{\partial t}(u(0,t)^2) = u(t_{max})^2 - u(0)^2 \propto \frac{u_{max}-u_0}{\bar{u}} = PI \qquad (5.2.5.8)$$

Where the kinetic energy measured is located at fixed location ($x = 0$), therefore simplifying the equation. Where the summation of the mechanical energy from the beginning of the cycle until the maximum flow velocity is directly correlated with the PI. Clinically, PI is measured to determine pathological flow states within the arterial tree, and is a simplified measure of the mechanical energy of flow. Therefore, by comparing mechanical energy between elastic and viscoelastic conduits, we may relate viscoelastic damping to the decrease in PI.

Additionally, we may see how energy dissipation is related to both frequency and wave speed by examining the spatial derivative of the Fourier transform function.

$$\frac{\partial}{\partial x}(u(x,t)^2) = \frac{\partial}{\partial x}\left(C_N^2 Exp\left[i2\omega\left(t - \frac{x}{c_Q}\right)\right]\right) = -\frac{i2\omega}{c_Q}u(x,t)^2 \qquad (5.2.5.9)$$

Where u is the particle velocity, ω is the frequency, C_N is the harmonic constant, t is time, x is the axial location along the conduit, c_Q is the Q-wave speed. Here we may additionally see how increased wave speed due to viscoelasticity as described above would decrease mechanical energy of the system.

These equations will not necessarily be fully solved, as mathematically coupling the relationship between wall properties and steady state upstream and downstream waveforms may not converge. But by listing these equations here, we may refer to them in the discussion of the results.

5.2.5.5   *Statistical Methods*

Measured response variables were compared using multi-factor analysis of variance (ANOVA). Sample size for each measure was limited to three for each group, and all groups passed the Anderson-Darling test for normality. Main effects were determined to be conduit type (E and VE), applied flow type (LPF and HPF), and point of measurement (Inlet and Outlet), and subsequently compared in three-way ANOVA. In cases where there was not separation between Inlet and Outlet, such as diameter strain and pressure modulus (E_P), two-way ANOVA was performed. Additionally, four-way ANOVA was performed on wave speed analysis, separating groups conduit type, applied flow type, wave measurement (P and Q), and by Fourier harmonic (f). Main (single-factor) and interactive (two-factor) effects were examined, with special focus on conduit material type and inlet/outlet comparison, with significance of $\alpha < 0.05$, unless otherwise noted.

5.3   Results

5.3.1   *Material Properties*

Frequency sweep measurements correspond well with those from the literature,(Kalcioglu et al., 2013; Mrozek et al., 2011) indicating direct relationship between viscous loss and m-PDMS weight percentage. Specifically, values for viscoelastic materials (70% 1M CSt m-PDMS: 108 kDa v-PDMS) show shear modulus values of 25 kPa and tan(δ) of 0.5 at 1 Hz, while elastic material (58.8% 500 CSt m-PDMS: 108 kDa v-PDMS) has similar stiffness with tan (δ) of 0.06.These values may then be incorporated into mock

113

blood vessel design by converting to the elastic modulus using the Poisson's Ratio of PDMS, which is 0.5.(Takeuchi and Cohen, 1999) Results are shown in Table 5.4.1, below:

	Elastic (58.8% 500 CSt : 108 kDa PDMS)	Viscoelastic (70% 1M CSt : 108 kDa PDMS)
Material Properties at 1 Hz	**E' = 68.9 kPa**	**E'= 67.1 kPa**
	E''= 4.09 kPa	**E''= 32.3 kPa**
	$\tan(\delta) = 0.06$	**$\tan(\delta) = 0.482$**

Table A.1.1.1- Frequency dependent material properties of poly(dimethylsiloxane) (PDMS).

Strain sweep results indicate strain softening at approximately 10% for all samples, well within the healthy physiological strain of 5%.(Bia et al., 2006; Nagai et al., 1999) Results are further shown in Appendix A1.

5.3.2   Comparison of Conduit Stiffness and Wave Speed

When pressure wave velocity (c_Q) and flow wave velocity (c_P) were compared between the different conduits, results showed no significant differences between elastic and viscoelastic conduits. Also, the conduit stiffness, as described by the pressure modulus (E_P) in equation 5.3.5.3.1, showed no significant differences between the groups, with pressure moduli of approximately 1200 mmHg, which matched the values to less compliant arteries (figure 5.4.2.1).(Bia et al., 2006; Buntin and Silver, 1990; Nagai et al., 1999; Tan et al., 2014)
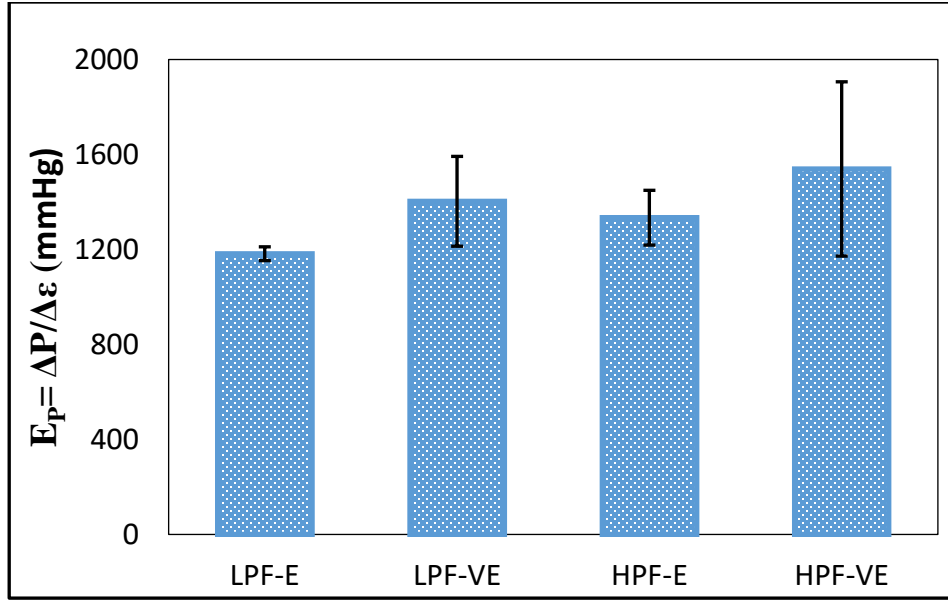
Figure 5.4.2.1- Pressure Modulus. Measured pressure modulus values (E_P) indicate slight increase in viscoelastic samples, though significant differences between tests were not found.

Pulse wave speeds show no significant changes with viscoelastic wall properties (figure 5.4.2.2). Pressure pulse wave velocity in viscous media with viscoelastic wall properties was initially outlined initially by Womersley, and continued by MacDonald:

$$c_0 = \sqrt{\frac{|E^*|h}{2R_0\rho}} \rightarrow c = c_0 / \left(1 - i\frac{\tan(\delta)}{2}\right) \qquad (5.3.2.1)$$

Theoretical descriptions of wave speed show decreased viscoelasticity represented by $\tan(\delta)$ in equation 5.4.2.1, results in decreased wave velocity. This value is illustrated by a red line in figure 5.4.2.2. Results show viscoelastic conduit properties have no discernable effect on *P* or *Q* wave speeds.

We additionally see significant changes between pressure wave velocities and their corresponding volumetric flow velocities, indicating c_Q and c_P response are not directly coupled. This differs from

theoretical pressure driven flow, which directly couples pressure and volumetric flow pulse wave velocities.
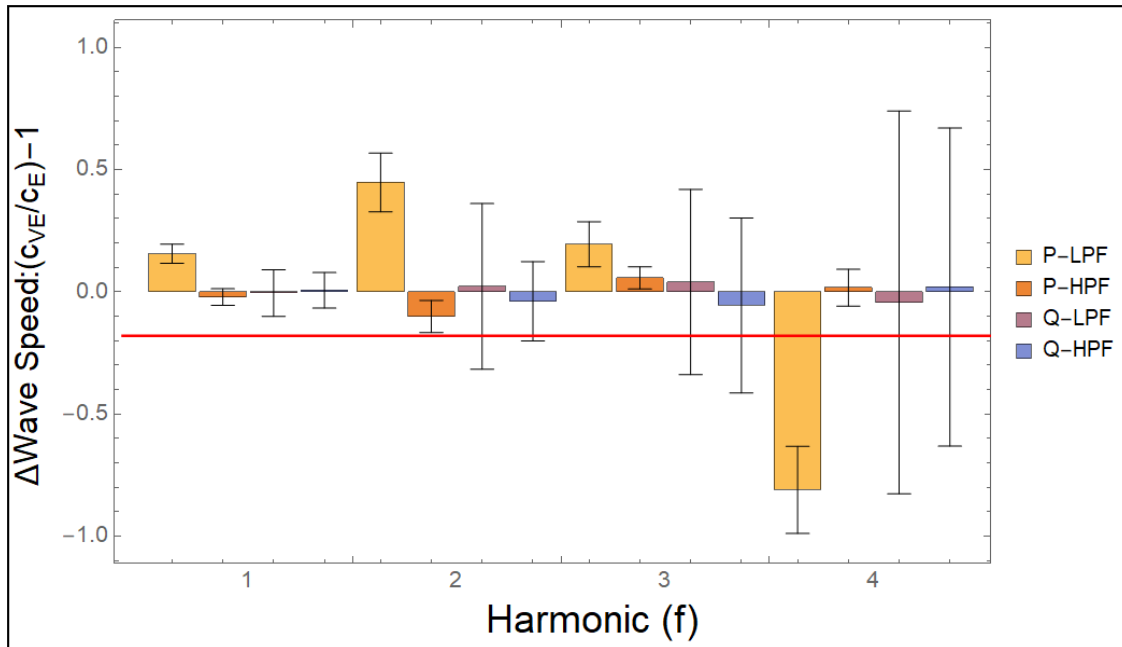
Figure 5.4.2.2- Fractional change in harmonic wave speed values of both pressure (P) and volumetric flow (Q). The red line indicates theoretical values for decreased wave speed from viscoelastic wall properties. Results indicate no significant change in single-factor comparison between elastic and viscoelastic wave speeds in four-way ANOVA.

5.3.3 *Pressure and Diameter Waveforms are Attenuated in Viscoelastic Conduits*

The pulsatile pressure waveforms at the inlet and outlet as well as the diameter strain curves during the cycle of mimetic cardiac output were determined to evaluate the contributions of material property to the changes in pressure waveforms and to the correlation between pressure waveforms and diameter strains (figure 5.4.3.1). Compared to elastic conduits, the attenuation and smoothing of the diameter curve in viscoelastic conduits were found for both flow pressures. This result indicated viscoelastic conduits increased cross-sectional area throughout the pressure cycle, which in turn decreased the impedance within the circulation, according to equation 5.3.5.5. We additionally found a slight phase lag for

viscoelastic conduits when compared to elastic conduits. This is in agreement with previous studies of artery responses using hysteresis of pressure-strain relationship for viscoelastic characterizations. (Armentano et al., 2014; Bia et al., 2006; Wang et al., 2013c)

Statistical analysis of the pressure wave results, using three-way ANOVA comparisons on three independent variables, i.e. conduit material type (E vs. VE), flow pressure range (LPF vs. HPF), and measurement location (inlet vs. outlet), showed a difference in the main effect of material property between elastic and viscoelastic conduits ($p = 0.083$). Importantly, viscoelastic conduits showed an average decrease of 3.9% in pressures compared to elastic ones. Also, the outlet pressures were significantly reduced compared to the inlet. Statistical analysis of diameter strain curves, using two-way ANOVA comparisons on conduit material type and flow pressure range showed ~11.3% decrease in the area change ($\varepsilon^2_{Max} - \varepsilon^2_{Min}$) over the cycle. No significant interactions were found between conduit material (E vs. VE) and either applied flow type (LPF vs. HPF), or measurement location (Inlet vs. Outlet).
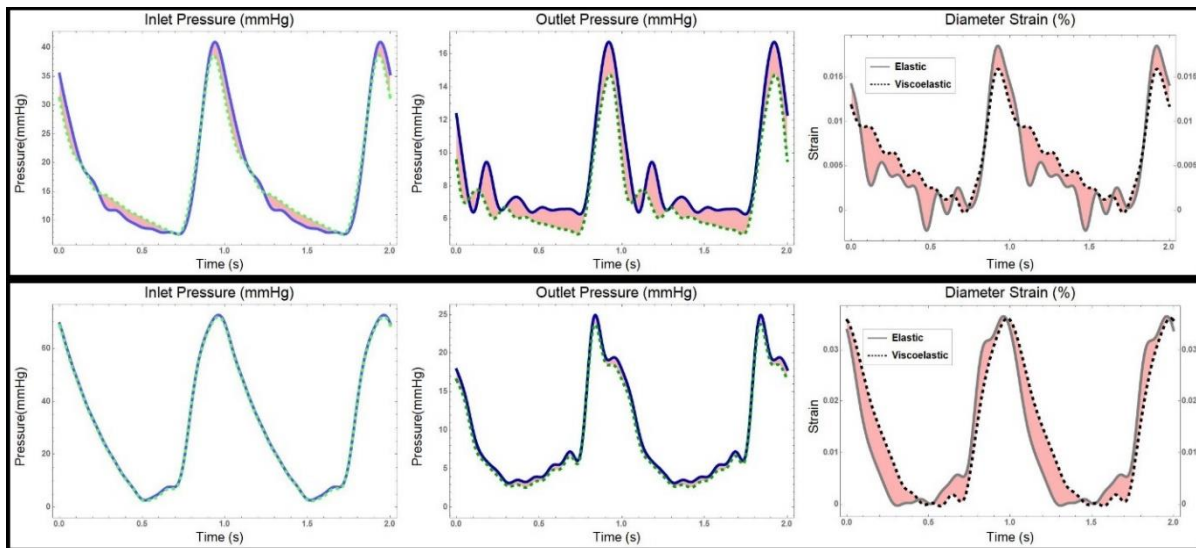
Figure 5.4.3.1- Representative pressure waveforms at inlet and outlet and corresponding diameter strain curves. Elastic conduit waveforms are illustrated with solid lines, while viscoelastic waveforms are dashed lines. Differences between elastic and viscoelastic waveforms are shown with red shading. Low

pressure waves (top, LPF) are shown to change between elastic and viscoelastic conduits, with both upstream and downstream pressure waves attenuated with viscoelastic conduit walls. Viscoelasticity of conduits showed less influences on pressure waves for high pressure waves (bottom, HPF). Diameter strain curves indicated greater smoothing in viscoelastic conduits over the cycle, with increased diameter strain later in the wave cycle (black, dashed line).

5.3.4   Wall Shear Stress Waveforms are Attenuated with Viscoelastic Wall Properties

Results on volumetric flow (*Q*) waveforms over the cycle (figure 5.4.4.1) showed attenuation of Q waves in viscoelastic conduits, which exhibited decreased peak-to-peak amplitude indicating decreased pulsatility or PI. This decreased PI value corresponded well with attenuated distension and pressure waveforms. Importantly, results also showed greater peak alignment between diameter strain curves and *Q* waves in viscoelastic conduits compared to elastic ones. The diameter increase during peak *Q* values for both inlet and outlet can contribute to the reduction in *WSS* oscillation (equation 5.4.4.1).

Similar to changes in the quantitative index of pulsatility (PI) for *Q* waves (*Q-PI*), statistically significant decreases in the PI for *WSS* (*WSS-PI*) were found in viscoelastic conduits when compared to elastic ones (figure 5.4.4.2). In addition to the reduced WSS oscillation, the average WSS significantly decreased in viscoelastic conduits when compared to elastic ones.

Main effect comparisons of volumetric flow waveforms showed a decrease of peak-to-peak amplitude in viscoelastic conduits compared to elastic ones, with 6% decrease in the pulsatility index (PI), and 9.1% decrease in PI from inlet to outlet. More importantly, resulting measures of WSS indicate significant decreases of 22.8% (figure 5.4.4.2). Within the ANOVA comparison, we see no interactive effect of conduit material (E vs. VE) with either applied flow type (LPF vs. HPF), or measurement location (Inlet vs. Outlet).

In the case of LPF, viscoelastic conduits caused a decrease in *Q-PI* by ~15.9%, but decrease in *WSS-PI* by 29.1%. These results were also found in HPF flow, though less drastic, with decreases of 2.0% in

Q-PI, and 20.0 % decrease in *WSS-PI*. This indicated is that phase alignment between diameter and Q-waves had a significant effect on WSS. Greater phase alignment in viscoelastic conduits, as shown in figure 5.4.4.2, reduced WSS-PI response. Increased WSS-PI at the outlet in elastic conduits indicates that resulting phase misalignment exacerbates high pulsatility in flow. Therefore, phase lag due to viscoelastic material properties has significant effects on improving fluid shear stress mechanical signaling.
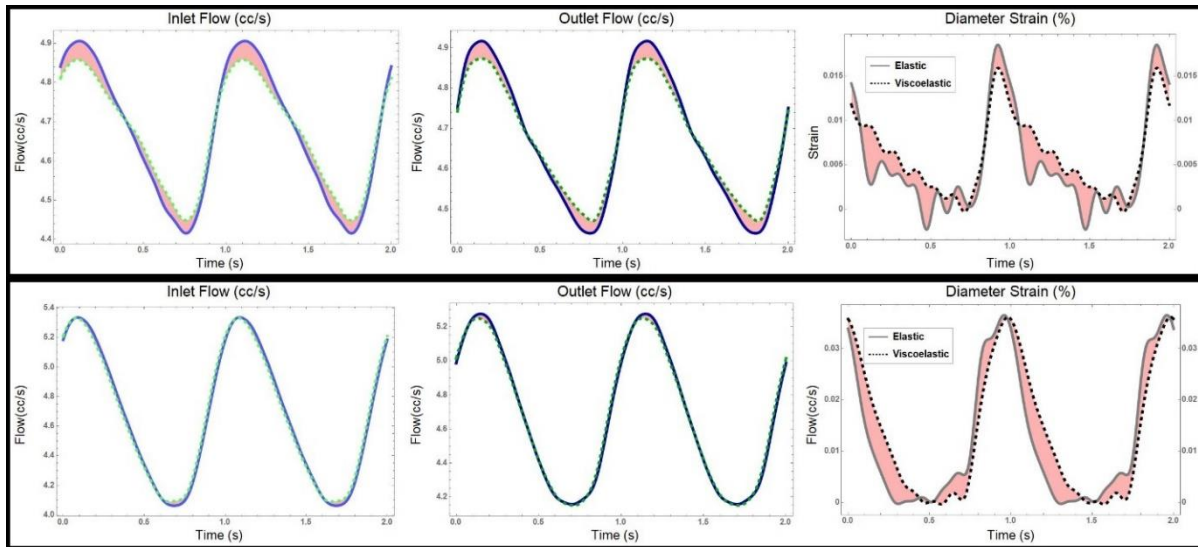
Figure 5.4.4.1- Representative volumetric flow (*Q*) waveforms at inlet and outlet and corresponding diameter strain curves. Elastic conduit waveforms are illustrated with solid lines, while viscoelastic waveforms are dashed lines. Low pressure waves (top, LPF) are shown to change between elastic and viscoelastic conduits, with both upstream and downstream *Q* waves attenuated with viscoelastic conduit walls. Viscoelasticity of conduits showed less influences on *Q* waves p for high pressure (bottom, HPF) . Diameter waveforms of viscoelastic conduits showed better peak phase alignment with *Q* (black, dashed line).

Wall shear stress was determined through applying the formula relating volumetric flow rate as shown in the below equation:

$$WSS = -\mu \frac{\partial \vec{u}}{\partial r} = \mu \frac{3\,\vec{Q}(t)}{\pi\,R_0^3 \lambda(t)^3} \qquad (5.3.4.1)$$

Where Q is the volumetric flow, R_0 is the initial radius, μ is the fluid viscosity, and λ is the stretch ratio of the diameter change. The use of this equation assumes fully developed, laminar flow.
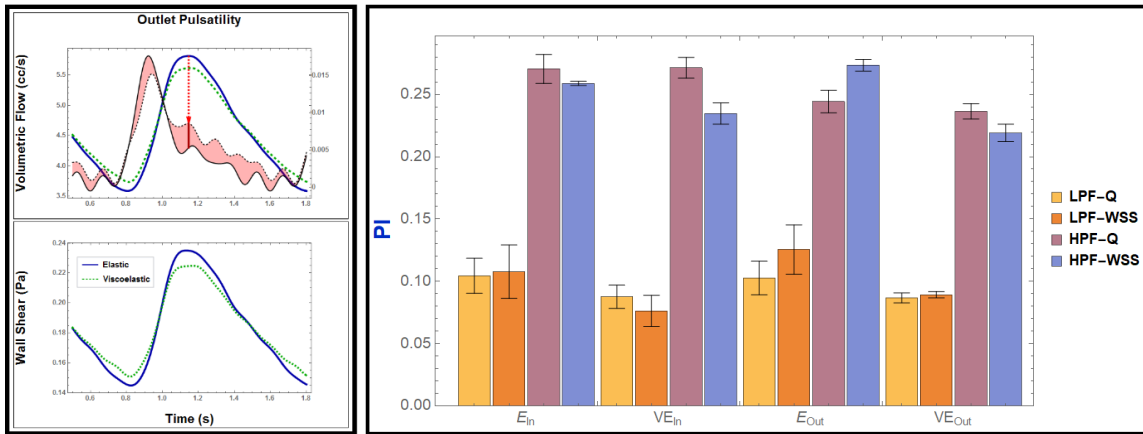
Figure 5.4.4.2- Comparison of PI as measured by flow rate (Q) and wall shear stress (WSS). Differences in waveform shapes and pulsatility (PI) present in comparison of elastic (E) to viscoelastic (VE) conduits. LPF-Q at the outlet is shown above left (Q-E: blue, solid line, Q-VE: green, dashed) matched with respective diameter values (E-diameter: black, solid line, VE-diameter: black, dashed line), with LPF-WSS shown bottom left. WSS waveforms show greater difference between elastic (E) and viscoelastic (VE) conduit, shown in the bar graph at right. Significant differences were seen between E and VE conduits for WSS measured PI using Bonferroni post-test analysis ($\alpha < 0.05$, labeled with +).

5.3.5   Mechanical Energy of Flow

120

The peak mechanical energy decreased by 4.9% (p=0.060) in viscoelastic conduits, when compared to elastic conduits. Mechanical energy also showed significant decreases of 5.9% occurred at the outlet compared to the inlet, following a similar trend as Q-wave comparisons. Additionally, interaction effects of conduit material type (E vs. VE) and flow type (LPF vs. HPF) indicate that there might be more decrease (p = 0.063) of mechanical energy in viscoelastic compared to elastic conduits for applied LPF than HPF (figure 5.4.5.1). Importantly, no significant changes were found in interactive effects of conduit material (E vs. VE) and upstream or downstream location (inlet vs. outlet). The energy results exhibited a similar trend as Q-PI, which can be supported by the relationship between mechanical energy and PI described in equation 5.3.5.8.

The mechanical energy of flow was solved for by using equation 5.3.5.7 listed above in section 5.3.5.4. Briefly, this is the material derivative of the kinetic energy:

$$\frac{D}{Dt}\left(\frac{\rho}{2}\boldsymbol{u}^2\right) = \frac{\partial}{\partial t}\left(\frac{\rho}{2}\boldsymbol{u}^2\right) + (\boldsymbol{u}\cdot\boldsymbol{\nabla})\left(\frac{\rho}{2}\boldsymbol{u}^2\right) \qquad (\,5.3.5.1\,)$$

This data was then plotted against time to indicate differences seen during the wave cycle. This equation again assumes fully developed, laminar flow. Mechanical energy was quantified at each of the inlet and outlet sensors, using the static cross-sectional area of the connective tubing at the point of measurement.
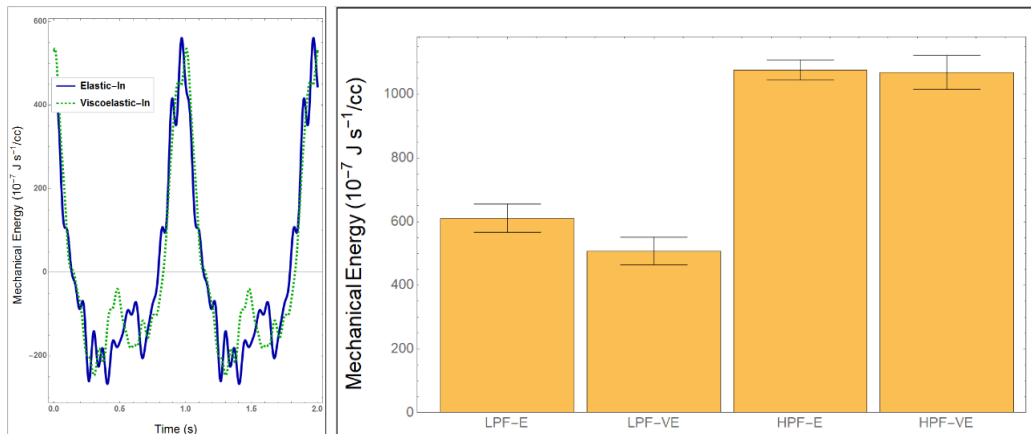
Figure 5.4.5.1- Mechanical energy of flow was calculated as the material derivative of the kinetic energy, referred to in section 5.4.4.3. This required time derivative and divergence of the kinetic energy. Sample mechanical energy curves are shown to the left, specifically physiologic applied pressure (LPF). Peak mechanical energy aligns with peak volumetric flow, but waveforms do not match. The bar graph on the right shows decreased mechanical energy with viscoelastic conduits (VE) compared to elastic conduits. Significant differences were seen comparing LPF-E and LPF-VE in a t-test ($\alpha < 0.05$).

5.4   Discussion

Our results have demonstrated several unique findings: (1) viscoelastic conduit properties attenuated WSS over the cycle, as well as pressure and flow waves upstream and downstream of the VE-conduit; (2) decreased peak-to-peak waveform amplitudes corresponded with the attenuation of diameter distension wave, extending strain through the end of the cycle; (3) such extension of strain through the cycle created greater phase alignment of diameter with *Q*-waveforms, thereby decreasing *WSS* pulsatility through increased cross-sectional area, as shown in figure 5.5.1. Additionally, attenuated strain waves indicated greater mean area over the cycle, thereby decreasing impedance, affecting upstream and downstream flow (figure 5.4.3.1). Finally, energy damping from viscous energy loss within the viscoelastic material would contribute to decreased PI over the length of the conduit. While greater *Q*-wave attenuation occurs with viscoelastic conduits, no relation is evident between PI decrease over the conduit length and conduit material properties. Therefore, the effects of impedance change may be the greater contributing factor to flow attenuation, though a longer conduit may show greater effects.

Shape of the strain curve was predicted in projected mechanics of the lumen (Figure 5.3.2), resulting from changing δ-values across the frequency spectra of the material interacting with harmonics of the pressure wave. Resulting WSS attenuation is supported by previous computational methods,(Raghu et al., 2011) but has not been discussed experimentally with direct comparison between viscoelastic and elastic conduits.
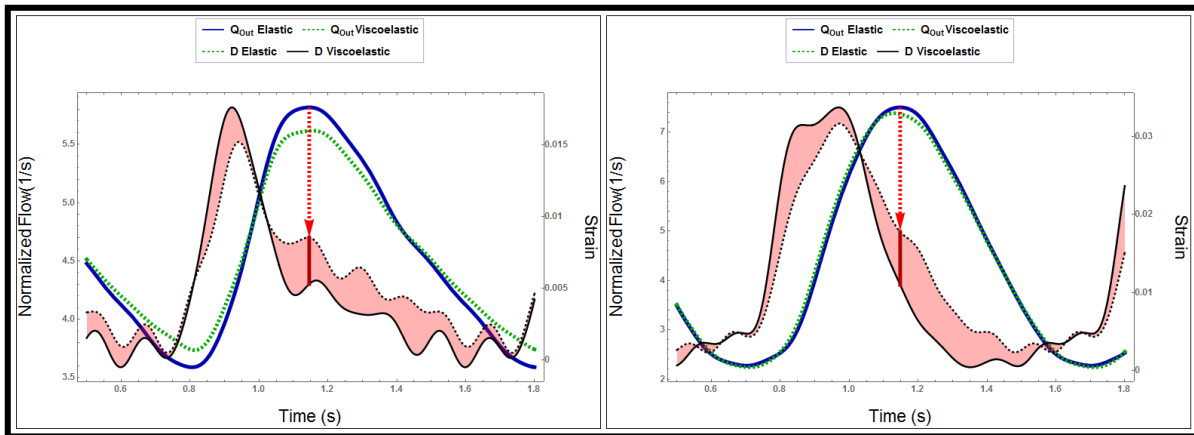
Figure 5.5.1- Phase alignment of the volumetric flow with the conduit distension for both low

pressure (left) and high pressure (right) conditions. Viscoelastic conduits exhibit a phase shift and

increased strain later in the pressure cycle, shown by the red coloration. This results in greater cross-

sectional area during peak volumetric flow (Q), decreasing shear stress at the wall, indicated by the red

arrows.

This study has provided evidence showing that phase alignment is a major contributing factor in

altering an important mechanical signal, WSS, whose influences on vascular endothelial and smooth

muscle cells and on vascular inflammation have been well known . (Elliott et al., 2015; Scott et al., 2013;

Tan et al., 2014) This is a new finding, given that existing studies have not examined the alignment of

area and flow phase. Previously, Q-waveforms were computationally shown to attenuate due to

viscoelastic wall properties,(Raghu et al., 2011) effects are more drastic when WSS is coupled to conduit

distension.

Mechanical energy of flow decreased with viscoelastic wall properties, which may be directly related

to several clinical measures. Mechanical energy of flow is characterized with the immediate change in

kinetic energy within the volume. While mechanical energy relates to clinical and experimental metrics

within the literature, it has been rarely associated to cell response or disease progression. Nevertheless,

increased mechanical energy would directly relate to many parameters important to cardiovascular diseases, as illustrated by the equation below:

$$u(x,t) = AExp\left[-i\,\omega\left(t - \frac{x}{c}\right)\right] \rightarrow \frac{\partial u(x,t)^2}{\partial t} + u(x,t)\frac{\partial u(x,t)^2}{\partial x} =$$

$$-i2\omega\left(1 - \frac{1}{c}AExp\left[-i\omega\left(t - \frac{x}{c}\right)\right]\right)A^2Exp\left[-i\,2\omega\left(t - \frac{x}{c}\right)\right] \quad (5.3.5.1)$$

Where u is the flow velocity, t is time, c is wave speed, x is distance along the artery, and ω is the angular frequency, which would be equivalent to the heart rate. This suggests that the mechanical energy is directly proportional to the heart rate (ω), flow amplitude (A), and wave speed (c), all of which are clinical indicators of cardiovascular disease.

The present study, through comparing fluid responses of viscoelasticity conduit materials with elastic materials of similar stiffness, highlights time-dependent wall effects on pulse wave responses. This study differs from previous studies in the area (Kalcioglu et al., 2013; Mrozek et al., 2011) by providing experimental comparisons of viscoelastic to elastic conduits, with well-defined material properties and flow wave parameters within physiological conditions. The majority of previous studies have focused on computational modeling, with minimal material characterization for experimental validation.(Bessems et al., 2008; Raghu et al., 2011; Taylor, 1959; Wang et al., 2016) Also, in the experimental validation of these studies, flow consisted of single harmonic waveform perturbations of the system, which could not show multifactorial effects on pulse pressure and flow waves, as demonstrated here. Effects of viscoelastic wall properties on wave travel and attenuation have been a subject of interest over the past 40 years, with some debate over the contribution to pulse wave attenuation. Previous measurements of frequency-dependent arterial material properties showed tan(δ) of approximately 0.15-0.25 (Bergel, 1961; Bia et al., 2006; Gow and Taylor, 1968; Gow et al., 1974; Learoyd and Taylor, 1966). These values might

be irrelevant to the cardiovascular system,(Hoeks et al., 2000) and highly dependent upon smooth muscle contraction within the cycle. (Armentano et al., 2006; Haga et al., 2007)

Interestingly, the study results suggest that viscoelastic wall properties could have beneficial damping properties on flow pulsatility. Greater viscoelasticity may reduce the detrimental pulsatility in the upstream as well as downstream by smoothing out high pulse waves, which could improve mechanotransductive signals in the arterial lumen. Because healthy vasculature is often characterized by higher viscoelasticity than diseased states, this finding can have significant implications to vascular physiology and vascular graft development. Decreased viscoelasticity may therefore be a significant contribution to cardiovascular disease progression, supporting previous studies examining changes in hysteresis with disease.(Wang et al., 2013c) Results herein additionally introduce catering frequency-dependent, viscoelastic material properties towards improved hemodynamics, as a novel direction in vascular grafting.(Armentano et al., 2014; Neufurth et al., 2015) Further work should be done to fully develop these concepts as a metric for disease progression and vascular grafting design criteria.

6 Future Directions

Future directions of the work may expand upon the coupling of the material properties to the flow, as well as the effects of changed hemodynamics on vascular cells. These two aspects are important in establishing viscoelasticity as an important tissue property within the vasculature, improving *in vivo* measurements of arterial properties and flow, as well as providing guidance in vascular graft design.

6.1 Coupling Material Properties and Hemodynamics

Currently, our work indicates viscoelastic wall properties affect both upstream and downstream waves within a steady-state system. This complicates analysis as the radial strain of the conduit is coupled to the pressure wave and vice versa. Time-dependent materials are complicated by the material history, preventing direct comparison to immediate stresses. While previous work focused on single perturbations and material/fluid response after start time,(Bessems et al., 2008; Wang et al., 2016) viscoelastic systems have not been examined approaching steady-state response. By recording pulse waves and diameter change from the system at rest towards its approach to steady-state would provide some insight into conduit diameter and waveform interdependence.

Experimental setup would be maintained, with the system beginning at rest with cyclic pulse waves applied until steady-state is reached. Data may then be analyzed through convolution of the PDMS material function with the measured strain and pressure:

$$\sigma = \int_0^t E(t-s)\varepsilon(s)\,ds$$

Resulting data would aid in coupling frequency-dependent material properties to steady-state response of the conduit.

6.2   Application of Cells

Applying cells to the inner surface of the lumen is the logical next step for understanding fluid effects on improving cell response. This may be done through functionalization of the PDMS lumen surface, and covalently attaching polypeptides capable of cell attachment, such as RGD. Due to the three-dimensional nature of the PDMS lumen, functionalization would require chemical treatment using hydrochloric acid and hydrogen peroxide,(Llobera et al., 2011) followed by APTES attachment. Poly(ethylene glycol) (PEG) with N-hydroxysuccinimide ester (NHS-ester) functional end groups may be used to bridge amine groups on both APTES and YRGDS while providing increased surface hydrophilicity, thereby providing an ideal surface for cell attachment. Preliminary work has been completed, indicating PEG and fibronectin (FN) protein binding to the PDMS surface (figure 6.2.1).
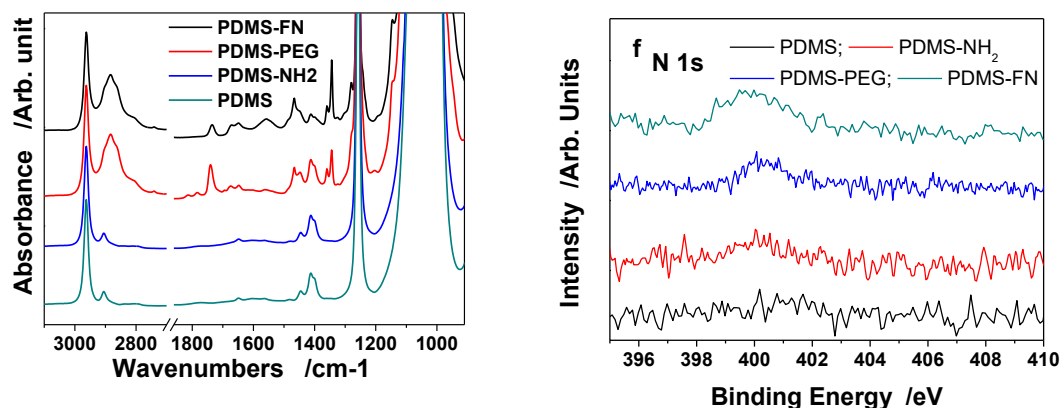
Figure 6.2.1- Fourier transform infra-red spectroscopy (FTIR) measurements (Left) and x-ray photoelectric spectroscopy (XPS) sweep (Right) of surface chemistry on treated PDMS. FTIR data shows characteristic NHS-Ester (triplet band at 1744 cm^{-1}, 1788 cm^{-1}, and 1816 cm^{-1}) and PEG peaks (shift towards 2900 cm^{-1}). Additionally, xps survey data (Right) shows greater concentrations of Nitrogen, indicating binding of greater Nitrogen amounts with APTES, NHS-ester groups, and finally fibronectin (FN).

As introduced in chapter 2, and shown in chapter 3, pulsatile fluid shear applied to endothelial cells may induce pathological responses, inducing inflammatory response. Mechanical signaling resulting from wall shear stress (WSS) may act in concert, or contrast to other signals, such as wall stretch and pressure mechanical signaling, reducing or exacerbating inflammatory response. While previous work has examined mechanotransduction of single signals,(Elliott et al., 2015; Haga et al., 2007; Scott et al., 2013) they have not been examined in concert, except in the body. Therefore, by attaching cells to the inner surface of the lumen, signal combinations may be examined to establish cellular response to multiple additive or subtractive signals.

References

Abbott, W.M., Megerman, J., Hasson, J.E., L'Italien, G., and Warnock, D.F. (1987). Effect of compliance mismatch on vascular graft patency. J. Vasc. Surg. *5*, 376–382.

Acharya, P.S., Majumdar, S., Jacob, M., Hayden, J., Mrass, P., Weninger, W., Assoian, R.K., and Pure, E. (2008). Fibroblast migration is mediated by CD44-dependent TGF activation. J. Cell Sci. *121*, 1393–1402.

Alastruey, J., Khir, A.W., Matthys, K.S., Segers, P., Sherwin, S.J., Verdonck, P.R., Parker, K.H., and Peiró, J. (2011). Pulse wave propagation in a model human arterial network: Assessment of 1-D visco-elastic simulations against in vitro measurements. J. Biomech. *44*, 2250–2258.

Alastruey, J., Passerini, T., Formaggia, L., and Peiró, J. (2012). Physical determining factors of the arterial pulse waveform: theoretical analysis and calculation using the 1-D formulation. J. Eng. Math. *77*, 19–37.

Alenghat, F.J., and Ingber, D.E. (2002). Mechanotransduction: All Signals Point to Cytoskeleton, Matrix, and Integrins. Sci. Signal. *2002*, pe6-pe6.

Anderson, R.N., (US), N.C. for H.S., and others (2003). Deaths: leading causes for 2001.

Ando, J., and Yamamoto, K. (2009). Vascular mechanobiology endothelial cell responses to fluid shear stress. Circ. J. *73*, 1983–1992.

Angelini, G.D., and Newby, A.C. (1989). The future of saphenous vein as a coronary artery bypass conduit. Eur. Heart J. *10*, 273–280.

Archie, J.P., Hyun, S., Kleinstreuer, C., Longest, P.W., Truskey, G.A., and Buchanan, J.R. (2001). Hemodynamic parameters and early intimal thickening in branching blood vessels. Crit. Rev. Biomed. Eng. *29*, 1–64.

Arciniegas, E., Sutton, A.B., Allen, T.D., and Schor, A.M. (1992). Transforming growth factor beta 1 promotes the differentiation of endothelial cells into smooth muscle-like cells in vitro. J. Cell Sci. *103*, 521–529.

Arciniegas, E., Ponce, L., Hartt, Y., Graterol, A., and Carlini, R.G. (2000). Intimal thickening involves transdifferentiation of embryonic endothelial cells. Anat. Rec. *258*, 47–57.

Armentano, R.L., Barra, J.G., Levenson, J., Simon, A., and Pichel, R.H. (1995). Arterial wall mechanics in conscious dogs. Assessment of viscous, inertial, and elastic moduli to characterize aortic wall behavior. Circ. Res. *76*, 468–478.

Armentano, R.L., Graf, S., Barra, J.G., Velikovsky, G., Baglivo, H., Sánchez, R., Simon, A., Pichel, R.H., and Levenson, J. (1998). Carotid Wall Viscosity Increase Is Related to Intima-Media Thickening in Hypertensive Patients. Hypertension *31*, 534–539.

Armentano, R.L., Barra, J.G., Santana, D.B., Pessana, F.M., Graf, S., Craiem, D., Brandani, L.M., Baglivo, H.P., and Sanchez, R.A. (2006). Smart Damping Modulation of Carotid Wall Energetics in Human Hypertension: Effects of Angiotensin-Converting Enzyme Inhibition. Hypertension *47*, 384–390.

Armentano, R.L., Cymberknop, L.J., Suarez Bagnasco, D., Montini Ballarin, F., Balay, G., Negreira, C., Abraham, G., and others (2014). Similarities of arterial collagen pressure-diameter relationship in ovine femoral arteries and PLLA vascular grafts. In Engineering in Medicine and Biology Society (EMBC), 2014 36th Annual International Conference of the IEEE, (IEEE), pp. 2302–2305.

Arnold, M., Cavalcanti-Adam, E.A., Glass, R., Blümmel, J., Eck, W., Kantlehner, M., Kessler, H., and Spatz, J.P. (2004). Activation of Integrin Function by Nanopatterned Adhesive Interfaces. ChemPhysChem *5*, 383–388.

Arribas, S.M., Hinek, A., and González, M.C. (2006). Elastic fibres and vascular structure in hypertension. Pharmacol. Ther. *111*, 771–791.

Asakura, T., and Karino, T. (1990). Flow patterns and spatial distribution of atherosclerotic lesions in human coronary arteries. Circ. Res. *66*, 1045–1066.

Aumailley, M., and Timpl, R. (1986). Attachment of cells to basement membrane collagen type IV. J. Cell Biol. *103*, 1569–1575.

Ayub Haider, Z., Arai, M., and Hirabayashi, K. (1993). Mechanism of the Gelation of Fibroin Solution. Biosci. Biotechnol. Biochem. *57*, 1910–1912.

Badylak, S.F., and Nerem, R.M. (2010). Progress in tissue engineering and regenerative medicine. Proc. Natl. Acad. Sci. *107*, 3285–3286.

Bao, G., and Suresh, S. (2003). Cell and molecular mechanics of biological materials. Nat. Mater. *2*, 715–725.

Bartels, H.L., and Lei, B. van der (1988). Small-calibre vascular grafting into the rat abdominal aorta with biodegradable prostheses. Lab. Anim. *22*, 122–126.

Battegay, E.J., Raines, E.W., Seifert, R.A., Bowen-Pope, D.F., and Ross, R. (1990). TGF-beta induces bimodal proliferation of connective tissue cells via complex control of an autocrine PDGF loop. Cell *63*, 515–524.

Beaussier, H., Naggara, O., Calvet, D., Joannides, R., Guegan-Massardier, E., Gerardin, E., Iacob, M., LaLoux, B., Bozec, E., Bellien, J., et al. (2011). Mechanical and Structural Characteristics of Carotid Plaques by Combined Analysis With Echotracking System and MR Imaging. JACC Cardiovasc. Imaging *4*, 468–477.

Berard, X., Déglise, S., Alonso, F., Saucy, F., Meda, P., Bordenave, L., Corpataux, J.-M., and Haefliger, J.-A. (2013). Role of hemodynamic forces in the ex vivo arterialization of human saphenous veins. J. Vasc. Surg. *57*, 1371–1382.

Bergel, D.H. (1961). The dynamic elastic properties of the arterial wall. J. Physiol. *156*, 458–469.

Bergh, N., Ulfhammer, E., Glise, K., Jern, S., and Karlsson, L. (2009). Influence of TNF-α and biomechanical stress on endothelial anti- and prothrombotic genes. Biochem. Biophys. Res. Commun. *385*, 314–318.

Berk, B.C. (2008). Atheroprotective Signaling Mechanisms Activated by Steady Laminar Flow in Endothelial Cells. Circulation *117*, 1082–1089.

Bessems, D., Giannopapa, C.G., Rutten, M.C.M., and van de Vosse, F.N. (2008). Experimental validation of a time-domain-based wave propagation model of blood flow in viscoelastic vessels. J. Biomech. Kidlington *41*, 284–291.

Bi, L., Cao, Z., Hu, Y., Song, Y., Yu, L., Yang, B., Mu, J., Huang, Z., and Han, Y. (2011). Effects of different cross-linking conditions on the properties of genipin-cross-linked chitosan/collagen scaffolds for cartilage tissue engineering. J. Mater. Sci. Mater. Med. *22*, 51–62.

Bia, D., Zócalo, Y., Pessana, F., Armentano, R., Pérez, H., Cabrera, E., Saldías, M., and Álvarez, I. (2006). Viscoelastic and functional similarities between native femoral arteries and fresh or cryopreserved arterial and venous homografts. Rev. Esp. Cardiol. Engl. Ed. *59*, 679–687.

Bini, E., Knight, D.P., and Kaplan, D.L. (2004). Mapping Domain Structures in Silks from Insects and Spiders Related to Protein Assembly. J. Mol. Biol. *335*, 27–40.

Birukov, K.G. (2009). Cyclic Stretch, Reactive Oxygen Species, and Vascular Remodeling. Antioxid. Redox Signal. *11*, 1651–1667.

Birukov, K.G., Shirinsky, V.P., Stepanova, O.V., Tkachuk, V.A., Hahn, A.W.A., Resink, T.J., and Smirnov, V.N. (1995). Stretch affects phenotype and proliferation of vascular smooth muscle cells. Mol. Cell. Biochem. *144*, 131–139.

Birukova, A.A., Moldobaeva, N., Xing, J., and Birukov, K.G. (2008). Magnitude-dependent effects of cyclic stretch on HGF- and VEGF-induced pulmonary endothelial remodeling and barrier regulation. Am. J. Physiol. - Lung Cell. Mol. Physiol. *295*, L612–L623.

Bryan, A.J., and Angelini, G.D. (1994). The biology of saphenous vein graft occlusion: Etiology and strategies for prevention. Curr. Opin. Cardiol. *9*, 641–649.

Buchanan, J.R., Kleinstreuer, C., Hyun, S., and Truskey, G.A. (2003). Hemodynamics simulation and identification of susceptible sites of atherosclerotic lesion formation in a model abdominal aorta. J. Biomech. *36*, 1185–1196.

Buntin, C.M., and Silver, F.H. (1990). Noninvasive assessment of mechanical properties of peripheral arteries. Ann. Biomed. Eng. *18*, 549–566.

Butler, M.F., Ng, Y.-F., and Pudney, P.D. (2003). Mechanism and kinetics of the crosslinking reaction between biopolymers containing primary amine groups and genipin. J. Polym. Sci. Part Polym. Chem. *41*, 3941–3953.

Byrom, M.J., Bannon, P.G., White, G.H., and Ng, M.K.C. (2010). Animal models for the assessment of novel vascular conduits. J. Vasc. Surg. *52*, 176–195.

Cameron, A., Davis, K.B., Green, G., and Schaff, H. V (1996). Coronary bypass surgery with internal-thoracic-artery grafts--effects on survival over a 15-year period. N. Engl. J. Med. *334*, 216–219.

Caro, C.G., Doorly, O.J., Tarnawski, M., Scott, K.T., Long, Q., Dumoulin, C.L., and Doorly, D.J. (1996). Non-planar curvature and branching of arteries and non-planar-type flow. Proc. R. Soc. Math. Phys. Eng. Sci. *452*, 185–197.

Caro, C.G., Cheshire, N.J., and Watkins, N. (2005). Preliminary comparative study of small amplitude helical and conventional ePTFE arteriovenous shunts in pigs. J. R. Soc. Interface R. Soc. *2*, 261–266.

Caterina, R.D. (2000). Endothelial dysfunctions: common denominators in vascular disease. Curr. Opin. Lipidol. *11*, 9–23.

Chaudhuri, O., Gu, L., Darnell, M., Klumpers, D., Bencherif, S.A., Weaver, J.C., Huebsch, N., and Mooney, D.J. (2015). Substrate stress relaxation regulates cell spreading. Nat. Commun. *6*, 6365.

Chen, X., Knight, D.P., Shao, Z., and Vollrath, F. (2001). Regenerated Bombyx silk solutions studied with rheometry and FTIR. Polymer *42*, 09969–09974.

Chien, S. (2006). Mechanotransduction and endothelial cell homeostasis: the wisdom of the cell. AJP Heart Circ. Physiol. *292*, H1209–H1224.

Chien, S., Li, S., and Shyy, J.Y. (1998). Effects of mechanical forces on signal transduction and gene expression in endothelial cells. Hypertension *31*, 162–169.

Chiu, J.-J., and Chien, S. (2011). Effects of disturbed flow on vascular endothelium: pathophysiological basis and clinical perspectives. Physiol. Rev. *91*, 327–387.

Chiu, J.-J., Chen, C.-N., Lee, P.-L., Tsair Yang, C., Sheng Chuang, H., Chien, S., and Usami, S. (2003). Analysis of the effect of disturbed flow on monocytic adhesion to endothelial cells. J. Biomech. *36*, 1883–1895.

Claridge, M.W., Bate, G.R., Hoskins, P.R., Adam, D.J., Bradbury, A.W., and Wilmink, A.B. (2009). Measurement of arterial stiffness in subjects with vascular disease: Are vessel wall changes more sensitive than increase in intima–media thickness? Atherosclerosis *205*, 477–480.

Clark, E.A., and Brugge, J.S. (1995). Integrins and signal transduction pathways: the road taken. Science *268*, 233–239.

Cookson, A.N., Doorly, D.J., and Sherwin, S.J. (2009). Mixing through stirring of steady flow in small amplitude helical tubes. Ann. Biomed. Eng. *37*, 710–721.

Cucina, A., Sterpetti, A.V., Borrelli, V., Pagliei, S., Cavallaro, A., and D'Angelo, L.S. (1998). Shear stress induces transforming growth factor–beta< sub> 1</sub> release by arterial endothelial cells. Surgery *123*, 212–217.

Dahl, S.L.M., Kypson, A.P., Lawson, J.H., Blum, J.L., Strader, J.T., Li, Y., Manson, R.J., Tente, W.E., DiBernardo, L., Hensley, M.T., et al. (2011). Readily Available Tissue-Engineered Vascular Grafts. Sci. Transl. Med. *3*, 68ra9-68ra9.

Davis, G.E., and Senger, D.R. (2005). Endothelial Extracellular Matrix: Biosynthesis, Remodeling, and Functions During Vascular Morphogenesis and Neovessel Stabilization. [Review]. Circ. Res. *97*, 1093–1107.

DePaola, N., Gimbrone, M.A., Davies, P.F., and Dewey, C.F. (1992). Vascular endothelium responds to fluid shear stress gradients. Arter. Thromb Vasc Biol *12*, 1254–1257.

Desai, M., Seifalian, A.M., and Hamilton, G. (2011). Role of prosthetic conduits in coronary artery bypass grafting. Eur. J. Cardio-Thorac. Surg. Off. J. Eur. Assoc. Cardio-Thorac. Surg. *40*, 394–398.

Deutsch, M., Meinhart, J., Zilla, P., Howanietz, N., Gorlitzer, M., Froeschl, A., Stuempflen, A., Bezuidenhout, D., and Grabenwoeger, M. (2009). Long-term experience in autologous in vitro endothelialization of infrainguinal ePTFE grafts. J. Vasc. Surg. *49*, 352–362.

Dilley RJ, McGeachie JK, and Prendergast FJ (1988). A review of the histologic changes in vein-to-artery grafts, with particular reference to intimal hyperplasia. Arch. Surg. *123*, 691–696.

Discher, D.E. (2005). Tissue Cells Feel and Respond to the Stiffness of Their Substrate. Science *310*, 1139–1143.

Dobrin, P.B. (1978). Mechanical properties of arterises. Physiol. Rev. *58*, 397–460.

Drury, J.L., and Mooney, D.J. (2003). Hydrogels for tissue engineering: scaffold design variables and applications. Biomaterials *24*, 4337–4351.

Duan, Z., and Sun, R. (2003). An improved model calculating CO_2 solubility in pure water and aqueous NaCl solutions from 273 to 533 K and from 0 to 2000 bar. Chem. Geol. *193*, 257–271.

Duan, Z., Møller, N., and Weare, J.H. (1992). An equation of state for the CH_4-CO_2-H_2O system: I. Pure systems from 0 to 1000° C and 0 to 8000 bar. Geochim. Cosmochim. Acta *56*, 2605–2617.

Duan, Z., Sun, R., Zhu, C., and Chou, I.-M. (2006). An improved model for the calculation of CO_2 solubility in aqueous solutions containing $Na+$, $K+$, $Ca2+$, $Mg2+$, $Cl-$, and $SO42-$. Mar. Chem. *98*, 131–139.

Ebenstein, D.M., Coughlin, D., Chapman, J., Li, C., and Pruitt, L.A. (2009). Nanomechanical properties of calcification, fibrous tissue, and hematoma from atherosclerotic plaques. J. Biomed. Mater. Res. A *91A*, 1028–1037.

Egorova, A.D., Van der Heiden, K., Van de Pas, S., Vennemann, P., Poelma, C., DeRuiter, M.C., Goumans, M.-J.T.H., Gittenberger-de Groot, A.C., ten Dijke, P., Poelmann, R.E., et al. (2011a). Tgfβ/Alk5 signaling is required for shear stress induced klf2 expression in embryonic endothelial cells. Dev. Dyn. *240*, 1670–1680.

Egorova, A.D., Khedoe, P.P.S.J., Goumans, M.-J.T.H., Yoder, B.K., Nauli, S.M., ten Dijke, P., Poelmann, R.E., and Hierck, B.P. (2011b). Lack of Primary Cilia Primes Shear-Induced Endothelial-to-Mesenchymal Transition. Circ. Res. *108*, 1093–1101.

Egorova, A.D., van der Heiden, K., Poelmann, R.E., and Hierck, B.P. (2012a). Primary cilia as biomechanical sensors in regulating endothelial function. Differentiation *83*, S56–S61.

Egorova, A.D., DeRuiter, M.C., de Boer, H.C., van de Pas, S., Gittenberger-de Groot, A.C., van Zonneveld, A.J., Poelmann, R.E., and Hierck, B.P. (2012b). Endothelial colony-forming cells show a mature transcriptional response to shear stress. Vitro Cell. Dev. Biol. - Anim. *48*, 21–29.

Eichenbaum, J.W. (1992). Trends in cataract surgery. Bull. N. Y. Acad. Med. *68*, 367.

Elliott, W.H., Tan, Y., Li, M., and Tan, W. (2015). High Pulsatility Flow Promotes Vascular Fibrosis by Triggering Endothelial EndMT and Fibroblast Activation. Cell. Mol. Bioeng. *8*, 285–295.

Emri, I., and von Bernstorff, B.S. (2006). The Effect of Molecular Mass Distribution on Time-Dependent Behavior of Polyamides. J. Appl. Mech. *73*, 752.

Engler, A.J., Sen, S., Sweeney, H.L., and Discher, D.E. (2006). Matrix Elasticity Directs Stem Cell Lineage Specification. Cell *126*, 677–689.

Floren, M.L., Spilimbergo, S., Motta, A., and Migliaresi, C. (2012). Carbon Dioxide Induced Silk Protein Gelation for Biomedical Applications. Biomacromolecules *13*, 2060–2072.

Fontaine, A.B., Spigos, D.G., Eaton, G., Dos Passos, S., Christoforidis, G., Khabiri, H., and Jung, S. (1994). Stent-induced Intimal Hyperplasia: Are There Fundamental Differences between Flexible and Rigid Stent Designs? J. Vasc. Interv. Radiol. *5*, 739–744.

Foss, C., Merzari, E., Migliaresi, C., and Motta, A. (2013). Silk Fibroin/Hyaluronic Acid 3D Matrices for Cartilage Tissue Engineering. Biomacromolecules *14*, 38–47.

Frid, M.G. (2002). Mature Vascular Endothelium Can Give Rise to Smooth Muscle Cells via Endothelial-Mesenchymal Transdifferentiation: In Vitro Analysis. Circ. Res. *90*, 1189–1196.

Friedman, M.H., Bargeron, C.B., Duncan, D.D., Hutchins, G.M., and Mark, F.F. (1992). Effects of arterial compliance and non-Newtonian rheology on correlations between intimal thickness and wall shear. J. Biomech. Eng. *114*, 317–320.

Fung, Y.C. (1967). Elasticity of soft tissues in simple elongation. Am. J. Physiol. Content *213*, 1532–1544.

Fung, Y.C., and Liu, S.Q. (1992). Strain distribution in small blood vessels with zero-stress state taken into consideration. Am. J. Physiol. - Heart Circ. Physiol. *262*, H544–H552.

Gan, C.T.-J., Lankhaar, J.-W., Westerhof, N., Marcus, J.T., Becker, A., Twisk, J.W., Boonstra, A., Postmus, P.E., and Vonk-Noordegraaf, A. (2007). Noninvasively assessed pulmonary artery stiffness predicts mortality in pulmonary arterial hypertension. CHEST J. *132*, 1906–1912.

Garanich, J.S. (2005). Shear stress inhibits smooth muscle cell migration via nitric oxide-mediated downregulation of matrix metalloproteinase-2 activity. AJP Heart Circ. Physiol. *288*, H2244–H2252.

Garanich, J.S., Mathura, R.A., Shi, Z.-D., and Tarbell, J.M. (2007). Effects of fluid shear stress on adventitial fibroblast migration: implications for flow-mediated mechanisms of arterialization and intimal hyperplasia. AJP Heart Circ. Physiol. *292*, H3128–H3135.

García-Cardeña, G., Comander, J., Anderson, K.R., Blackman, B.R., and Gimbrone, M.A. (2001). Biomechanical activation of vascular endothelium as a determinant of its functional phenotype. Proc. Natl. Acad. Sci. *98*, 4478–4485.

Gessaroli, M., Bombardi, C., Giunti, M., and Bacci, M.L. (2012). Prevention of neointimal hyperplasia associated with modified stretch expanded polytetrafluoroethylene hemodialysis grafts (Gore) in an experimental preclinical study in swine. J. Vasc. Surg. *55*, 192–202.

Ghista, D.N., and Kabinejadian, F. (2013). Coronary artery bypass grafting hemodynamics and anastomosis design: a biomedical engineering review. Biomed. Eng. Online *12*, 129.

Giannattasio, C., Salvi, P., Valbusa, F., Kearney-Schwartz, A., Capra, A., Amigoni, M., Failla, M., Boffi, L., Madotto, F., Benetos, A., et al. (2008). Simultaneous Measurement of Beat-to-Beat Carotid Diameter and Pressure Changes to Assess Arterial Mechanical Properties. Hypertension *52*, 896–902.

Gimbrone, M.A., Nagel, T., and Topper, J.N. (1997). Biomechanical activation: an emerging paradigm in endothelial adhesion biology. J. Clin. Invest. *99*, 1809–1813.

Glatz-Reichenbach, J.K., Sorriero, L., and Fitzgerald, J.J. (1994). Influence of crosslinking on the molecular relaxation of an amorphous copolymer near its glass-transition temperature. Macromolecules *27*, 1338–1343.

Gow, B.S., and Taylor, M.G. (1968). Measurement of Viscoelastic Properties of Arteries in the Living Dog. Circ. Res. *23*, 111–122.

Gow, B.S., Schonfeld, D., and Patel, D.J. (1974). The dynamic elastic properties of the canine left circumflex coronary artery. J. Biomech. *7*, 389–395.

Greenwald, S.E., and Berry, C.L. (2000). Improving vascular grafts: the importance of mechanical and haemodynamic properties. J. Pathol. *190*, 292–299.

Greil, O., Pflugbeil, G., Weigand, K., Wei\s s, W., Liepsch, D., Maurer, P.C., and Berger, H. (2003). Changes in carotid artery flow velocities after stent implantation: a fluid dynamics study with laser Doppler anemometry. J. Endovasc. Ther. *10*, 275–284.

Guan, J., Porter, D., and Vollrath, F. (2013). Thermally Induced Changes in Dynamic Mechanical Properties of Native Silks. Biomacromolecules *14*, 930–937.

Guilak, F., Cohen, D.M., Estes, B.T., Gimble, J.M., Liedtke, W., and Chen, C.S. (2009). Control of Stem Cell Fate by Physical Interactions with the Extracellular Matrix. Cell Stem Cell *5*, 17–26.

Guo, W., Frey, M.T., Burnham, N.A., and Wang, Y. (2006). Substrate Rigidity Regulates the Formation and Maintenance of Tissues. Biophys. J. *90*, 2213–2220.

Haga, J.H., Li, Y.-S.J., and Chien, S. (2007). Molecular basis of the effects of mechanical stretch on vascular smooth muscle cells. J. Biomech. *40*, 947–960.

Hamel, E., Del Campo, A.A., Lowe, M.C., and Lin, C.M. (1981). Interactions of taxol, microtubule-associated proteins, and guanine nucleotides in tubulin polymerization. J. Biol. Chem. *256*, 11887–11894.

Haruguchi, H., and Teraoka, S. (2003). Intimal hyperplasia and hemodynamic factors in arterial bypass and arteriovenous grafts: a review. J. Artif. Organs Off. J. Jpn. Soc. Artif. Organs *6*, 227–235.

Hasan, A., Memic, A., Annabi, N., Hossain, M., Paul, A., Dokmeci, M.R., Dehghani, F., and Khademhosseini, A. (2014). Electrospun scaffolds for tissue engineering of vascular grafts. Acta Biomater. *10*, 11–25.

Hashimoto, N., Phan, S.H., Imaizumi, K., Matsuo, M., Nakashima, H., Kawabe, T., Shimokata, K., and Hasegawa, Y. (2010). Endothelial–mesenchymal transition in bleomycin-induced pulmonary fibrosis. Am. J. Respir. Cell Mol. Biol. *43*, 161–172.

He, X., and Ku, D.N. (1996). Pulsatile flow in the human left coronary artery bifurcation: Average conditions. J. Biomech. Eng. *118*, 74–82.

Health, D. of (2007). Improving diabetes services: the NSF four years on.

Hellums, J.D. (1993). Whitaker lecture: Biorheology in thrombosis research. Annals of Biomedical Engineering. Ann. Biomed. Eng. *22*, 445–455.

Herbst, T.J., McCarthy, J.B., Tsilibary, E.C., and Furcht, L.T. (1988). Differential effects of laminin, intact type IV collagen, and specific domains of type IV collagen on endothelial cell adhesion and migration. J. Cell Biol. *106*, 1365–1373.

Hierck, B.P., Van der Heiden, K., Alkemade, F.E., Van de Pas, S., Van Thienen, J.V., Groenendijk, B.C.W., Bax, W.H., Van der Laarse, A., Deruiter, M.C., Horrevoets, A.J.G., et al. (2008). Primary cilia sensitize endothelial cells for fluid shear stress. Dev. Dyn. Off. Publ. Am. Assoc. Anat. *237*, 725–735.

Hoeks, A.P.G., Willigers, J.M., and Reneman, R.S. (2000). Effects of Assessment and Processing Techniques on the Shape of Arterial Pressure-Distension Loops. J. Vasc. Res. *37*, 494–500.

Holenstein, R., Niederer, P., and Anliker, M. (1980). A viscoelastic model for use in predicting arterial pulse waves. J. Biomech. Eng. *102*, 318–325.

Hollister, S.J. (2005). Porous scaffold design for tissue engineering. Nat. Mater. *4*, 518–524.

Holzapfel, G.A. (2004). Comparison of a Multi-Layer Structural Model for Arterial Walls With a Fung-Type Model, and Issues of Material Stability. J. Biomech. Eng. *126*, 264.

Holzapfel, G.A. (2005). Determination of layer-specific mechanical properties of human coronary arteries with nonatherosclerotic intimal thickening and related constitutive modeling. AJP Heart Circ. Physiol. *289*, H2048–H2058.

Howard, A.B., Alexander, R.W., Nerem, R.M., Griendling, K.K., and Taylor, W.R. (1997). Cyclic strain induces an oxidative stress in endothelial cells. Am. J. Physiol. - Cell Physiol. *272*, C421–C427.

Hsu, P.-P., Li, S., Li, Y.-S., Usami, S., Ratcliffe, A., Wang, X., and Chien, S. (2001). Effects of Flow Patterns on Endothelial Cell Migration into a Zone of Mechanical Denudation. Biochem. Biophys. Res. Commun. *285*, 751–759.

Hu, X., Kaplan, D., and Cebe, P. (2006). Determining Beta-Sheet Crystallinity in Fibrous Proteins by Thermal Analysis and Infrared Spectroscopy. Macromolecules *39*, 6161–6170.

Hu, X., Shmelev, K., Sun, L., Gil, E.-S., Park, S.-H., Cebe, P., and Kaplan, D.L. (2011). Regulation of Silk Material Structure by Temperature-Controlled Water Vapor Annealing. Biomacromolecules *12*, 1686–1696.

Humphrey, J.D. (2007). Vascular Adaptation and Mechanical Homeostasis at Tissue, Cellular, and Sub-cellular Levels. Cell Biochem. Biophys. *50*, 53–78.

Hunter, K.S., Albietz, J.A., Lee, P.-F., Lanning, C.J., Lammers, S.R., Hofmeister, S.H., Kao, P.H., Qi, H.J., Stenmark, K.R., and Shandas, R. (2010). In vivo measurement of proximal pulmonary artery elastic modulus in the neonatal calf model of pulmonary hypertension: development and ex vivo validation. J. Appl. Physiol. *108*, 968–975.

Huynh, J., Nishimura, N., Rana, K., Peloquin, J.M., Califano, J.P., Montague, C.R., King, M.R., Schaffer, C.B., and Reinhart-King, C.A. (2011). Age-Related Intimal Stiffening Enhances Endothelial Permeability and Leukocyte Transmigration. Sci. Transl. Med. *3*, 112ra122-112ra122.

Hyun, K., Wilhelm, M., Klein, C.O., Cho, K.S., Nam, J.G., Ahn, K.H., Lee, S.J., Ewoldt, R.H., and McKinley, G.H. (2011). A review of nonlinear oscillatory shear tests: Analysis and application of large amplitude oscillatory shear (LAOS). Prog. Polym. Sci. *36*, 1697–1753.

Imamura, H., Ohta, T., Tsunetoshi, K., Doi, K., Nozaki, K., Takagi, Y., and Kikuta, K. (2010). Transdifferentiation of bone marrow-derived endothelial progenitor cells into the smooth muscle cell lineage mediated by tansforming growth factor-β1. Atherosclerosis *211*, 114–121.

Ingber, D. (2003). Mechanobiology and diseases of mechanotransduction. Ann. Med. *35*, 564–577.

Inoguchi, H., Kwon, I.K., Inoue, E., Takamizawa, K., Maehara, Y., and Matsuda, T. (2006). Mechanical responses of a compliant electrospun poly(l-lactide-co-ε-caprolactone) small-diameter vascular graft. Biomaterials *27*, 1470–1478.

Jiang, Z., Tao, M., Omalley, K.A., Wang, D., Ozaki, C.K., and Berceli, S.A. (2009). Established neointimal hyperplasia in vein grafts expands via TGF- -mediated progressive fibrosis. AJP Heart Circ. Physiol. *297*, H1200–H1207.

Jung, B., Markl, M., Föll, D., and Hennig, J. (2006). Investigating myocardial motion by MRI using tissue phase mapping. Eur. J. Cardio-Thorac. Surg. Off. J. Eur. Assoc. Cardio-Thorac. Surg. *29 Suppl 1*, S150-7.

Kalath, S., Tsipouras, P., and Silver, F.H. (1986). Non-invasive assessment of aortic mechanical properties. Ann. Biomed. Eng. *14*, 513–524.

Kalcioglu, Z.I., Mrozek, R.A., Mahmoodian, R., VanLandingham, M.R., Lenhart, J.L., and Van Vliet, K.J. (2013). Tunable mechanical behavior of synthetic organogels as biofidelic tissue simulants. J. Biomech. *46*, 1583–1591.

Kawasaki, M., Ito, Y., Yokoyama, H., Arai, M., Takemura, G., Hara, A., Ichiki, Y., Takatsu, H., Minatoguchi, S., and Fujiwara, H. (2005). Assessment of arterial medial characteristics in human carotid arteries using integrated backscatter ultrasound and its histological implications. Atherosclerosis *180*, 145–154.

Keten, S., Xu, Z., Ihle, B., and Buehler, M.J. (2010). Nanoconfinement controls stiffness, strength and mechanical toughness of β-sheet crystals in silk. Nat. Mater. *9*, 359–367.

Khalil, N., Xu, Y.D., O'Connor, R., and Duronio, V. (2005). Proliferation of pulmonary interstitial fibroblasts is mediated by transforming growth factor-beta1-induced release of extracellular fibroblast growth factor-2 and phosphorylation of p38 MAPK and JNK. J. Biol. Chem. *280*, 43000–43009.

Kim, B.-S., Nikolovski, J., Bonadio, J., and Mooney, D.J. (1999). Cyclic mechanical strain regulates the development of engineered smooth muscle tissue. Nat. Biotechnol. *17*, 979–983.

Kim, U.-J., Park, J., Joo Kim, H., Wada, M., and Kaplan, D.L. (2005). Three-dimensional aqueous-derived biomaterial scaffolds from silk fibroin. Biomaterials *26*, 2775–2785.

Kim, Y.H., Chandran, K.B., Bower, T.J., and Corson, J.D. (1993). Flow dynamics across end-to-end vascular bypass graft anastomoses. Ann. Biomed. Eng. *21*, 311–320.

Kladakis, S.M., and Nerem, R.M. (2004). Endothelial Cell Monolayer Formation: Effect of Substrate and Fluid Shear Stress. Endothelium *11*, 29–44.

Kokudo, T., Suzuki, Y., Yoshimatsu, Y., Yamazaki, T., Watabe, T., and Miyazono, K. (2008). Snail is required for TGF -induced endothelial-mesenchymal transition of embryonic stem cell-derived endothelial cells. J. Cell Sci. *121*, 3317–3324.

Korhonen, R.K., Laasanen, M.S., Töyräs, J., Lappalainen, R., Helminen, H.J., and Jurvelin, J.S. (2003). Fibril reinforced poroelastic model predicts specifically mechanical behavior of normal, proteoglycan depleted and collagen degraded articular cartilage. J. Biomech. *36*, 1373–1379.

Krumme, A., Lehtinen, A., and Viikna, A. (2004). Crystallisation behaviour of high density polyethylene blends with bimodal molar mass distribution 1. Basic characteristics and isothermal crystallisation. Eur. Polym. J. *40*, 359–369.

Ku, D.N., Giddens, D.P., Zarins, C.K., and Glagov, S. (1985). Pulsatile flow and atherosclerosis in the human carotid bifurcation. Positive correlation between plaque location and low and oscillating shear stress. Arteriosclerosis *5*, 293–302.

Ku, J.P., Elkins, C.J., and Taylor, C.A. (2005). Comparison of CFD and MRI Flow and Velocities in an In Vitro Large Artery Bypass Graft Model. Ann. Biomed. Eng. *33*, 257–269.

Lan, T.-H., Huang, X.-Q., and Tan, H.-M. (2013). Vascular fibrosis in atherosclerosis. Cardiovasc. Pathol. *22*, 401–407.

Lao, L.L., and Venkatraman, S.S. (2008). Adjustable paclitaxel release kinetics and its efficacy to inhibit smooth muscle cells proliferation. J. Control. Release Off. J. Control. Release Soc. *130*, 9–14.

Learoyd, B.M., and Taylor, M.G. (1966). Alterations with Age in the Viscoelastic Properties of Human Arterial Walls. Circ. Res. *18*, 278–292.

Lee, D.A., and Bader, D.L. (1997). Compressive strains at physiological frequencies influence the metabolism of chondrocytes seeded in agarose. J. Orthop. Res. *15*, 181–188.

Lee, K.E., Lee, J.S., and Yoo, J.Y. (2011). A numerical study on steady flow in helically sinuous vascular prostheses. Med. Eng. Phys. *33*, 38–46.

Lee, S.-W., Antiga, L., and Steinman, D.A. (2009). Correlations among indicators of disturbed flow at the normal carotid bifurcation. J. Biomech. Eng. *131*, 061013.

Lei, D.B. van der, Wildevuur, C.R.H., Nieuwenhuis, P., Blaauw, E.H., Dijk, F., Hulstaert, C.E., and Molenaar, I. (1985). Regeneration of the arterial wall in microporous, compliant, biodegradable vascular grafts after implantation into the rat abdominal aorta. Cell Tissue Res. *242*, 569–578.

Lemarié, C.A., Tharaux, P.-L., and Lehoux, S. (2010). Extracellular matrix alterations in hypertensive vascular remodeling. J. Mol. Cell. Cardiol. *48*, 433–439.

Leung, D.Y., Glagov, S., and Mathews, M.B. (1976). Cyclic stretching stimulates synthesis of matrix components by arterial smooth muscle cells in vitro. Science *191*, 475–477.

Levesque, M.J., Liepsch, D., Moravec, S., and Nerem, R.M. (1986). Correlation of endothelial cell shape and wall shear stress in a stenosed dog aorta. Arterioscler. Thromb. Vasc. Biol. *6*, 220–229.

Li, L., Terry, C.M., Blumenthal, D.K., Kuji, T., Masaki, T., Kwan, B.C.H., Zhuplatov, I., Leypoldt, J.K., and Cheung, A.K. (2007). Cellular and morphological changes during neointimal hyperplasia development in a porcine arteriovenous graft model. Nephrol. Dial. Transplant. *22*, 3139–3146.

Li, M., Stenmark, K.R., Shandas, R., and Tan, W. (2009). EFFECTS OF PATHOLOGIC FLOW ON PULMONARY ARTERY ENDOTHELIAL PRODUCTION OF VASOACTIVE MEDIATORS AND GROWTH FACTORS. J. Vasc. Res. *46*, 561–571.

Liu, S.Q., and Goldman, J. (2001). Role of blood shear stress in the regulation of vascular smooth muscle cell migration. Biomed. Eng. IEEE Trans. On *48*, 474–483.

Liu, A., Tian, L., Golob, M., Eickhoff, J.C., Boston, M., and Chesler, N.C. (2015). 17β-Estradiol Attenuates Conduit Pulmonary Artery Mechanical Property Changes With Pulmonary Arterial Hypertension. Hypertension *66*, 1082–1088.

Liu, F., Mih, J.D., Shea, B.S., Kho, A.T., Sharif, A.S., Tager, A.M., and Tschumperlin, D.J. (2010). Feedback amplification of fibrosis through matrix stiffening and COX-2 suppression. J. Cell Biol. *190*, 693–706.

Liu, M., Kluger, M.S., D'Alessio, A., García-Cardeña, G., and Pober, J.S. (2008). Regulation of Arterial-Venous Differences in Tumor Necrosis Factor Responsiveness of Endothelial Cells by Anatomic Context. Am. J. Pathol. *172*, 1088–1099.

Llobera, A., Ibarlucea, B., Fernández-Sánchez, C., Demming, S., Büttgenbach, S., and Llobera, A. (2011). Biofunctionalization of PDMS-based microfluidic systems. Protoc. Exch.

Lockett, F.J. (1972). Nonlinear viscoelastic solids (Academic Press).

London, G., Covic, A., Goldsmith, D., Wiecek, A., Suleymanlar, G., Ortiz, A., Massy, Z., Lindholm, B., Martinez-Castelao, A., Fliser, D., et al. (2011). Arterial aging and arterial disease: interplay between central hemodynamics, cardiac work, and organ flow—implications for CKD and cardiovascular disease. Kidney Int. Suppl. *1*, 10–12.

Lu, Q., and Rounds, S. (2012). Focal adhesion kinase and endothelial cell apoptosis. Microvasc. Res. *83*, 56–63.

Maddaluno, L., Rudini, N., Cuttano, R., Bravi, L., Giampietro, C., Corada, M., Ferrarini, L., Orsenigo, F., Papa, E., Boulday, G., et al. (2013). EndMT contributes to the onset and progression of cerebral cavernous malformations. Nature *498*, 492–496.

Madhavan, K., Belchenko, D., Motta, A., and Tan, W. (2010). Evaluation of composition and crosslinking effects on collagen-based composite constructs. Acta Biomater. *6*, 1413–1422.

Madhavan, K., Elliott, W.H., Bonani, W., Monnet, E., and Tan, W. (2013). Mechanical and biocompatible characterizations of a readily available multilayer vascular graft. J. Biomed. Mater. Res. B Appl. Biomater. *101B*, 506–519.

Mak, A.F. (1986). The Apparent Viscoelastic Behavior of Articular Cartilage—The Contributions From the Intrinsic Matrix Viscoelasticity and Interstitial Fluid Flows. J. Biomech. Eng. *108*, 123–130.

Malek, A.M., and Izumo, S. (1996). Mechanism of endothelial cell shape change and cytoskeletal remodeling in response to fluid shear stress. J. Cell Sci. *109 (Pt 4)*, 713–726.

Malek, A.M., Alper, S.L., and Izumo, S. (1999). Hemodynamic Shear Stress and Its Role in Atherosclerosis. J. Am. Med. Assoc. *282*, 2035–2042.

Marsh, R.E., Corey, R.B., and Pauling, L. (1955). An investigation of the structure of silk fibroin. Biochim. Biophys. Acta *16*, 1–34.

Mason, B.N., Starchenko, A., Williams, R.M., Bonassar, L.J., and Reinhart-King, C.A. (2013). Tuning three-dimensional collagen matrix stiffness independently of collagen concentration modulates endothelial cell behavior. Acta Biomater. *9*, 4635–4644.

Mata-Greenwood, E., Grobe, A., Kumar, S., Noskina, Y., and Black, S.M. (2005). Cyclic stretch increases VEGF expression in pulmonary arterial smooth muscle cells via TGF-β1 and reactive oxygen species: a requirement for NAD(P)H oxidase. Am. J. Physiol. - Lung Cell. Mol. Physiol. *289*, L288–L289.

Mathers, C.D., and Loncar, D. (2006). Projections of Global Mortality and Burden of Disease from 2002 to 2030. PLoS Med *3*, e442.

McArthur, C., Geddes, C.C., and Baxter, G.M. (2011). Early Measurement of Pulsatility and Resistive Indexes: Correlation with Long-term Renal Transplant Function. Radiology *259*, 278–285.

McKenna, K.A., Hinds, M.T., Sarao, R.C., Wu, P.-C., Maslen, C.L., Glanville, R.W., Babcock, D., and Gregory, K.W. (2012). Mechanical property characterization of electrospun recombinant human tropoelastin for vascular graft biomaterials. Acta Biomater. *8*, 225–233.

Medici, D., Potenta, S., and Kalluri, R. (2011). Transforming growth factor-β2 promotes Snail-mediated endothelial–mesenchymal transition through convergence of Smad-dependent and Smad-independent signalling. Biochem. J. *437*, 515–520.

Mi, F.-L., Shyu, S.-S., and Peng, C.-K. (2005). Characterization of ring-opening polymerization of genipin and pH-dependent cross-linking reactions between chitosan and genipin. J. Polym. Sci. Part Polym. Chem. *43*, 1985–2000.

Mitchell, G.F. (2008). Effects of central arterial aging on the structure and function of the peripheral vasculature: implications for end-organ damage. J. Appl. Physiol. *105*, 1652–1660.

Mitchell, G.F., Hwang, S.-J., Vasan, R.S., Larson, M.G., Pencina, M.J., Hamburg, N.M., Vita, J.A., Levy, D., and Benjamin, E.J. (2010). Arterial Stiffness and Cardiovascular Events The Framingham Heart Study. Circulation *121*, 505–511.

Mitchell, G.F., van Buchem, M.A., Sigurdsson, S., Gotal, J.D., Jonsdottir, M.K., Kjartansson, O., Garcia, M., Aspelund, T., Harris, T.B., Gudnason, V., et al. (2011). Arterial stiffness, pressure and flow pulsatility and brain structure and function: the Age, Gene/Environment Susceptibility - Reykjavik Study. Brain *134*, 3398–3407.

Morinaga, K., Eguchi, H., Miyazaki, T., Okadome, K., and Sugimachi, K. (1987). Development and regression of intimal thickening of arterially transplanted autologous vein grafts in dogs. J. Vasc. Surg. *5*, 719–730.

Motta, A., Barbato, B., Foss, C., Torricelli, P., and Migliaresi, C. (2011). Stabilization of Bombyx mori silk fibroin/sericin films by crosslinking with PEG-DE 600 and genipin. J. Bioact. Compat. Polym. *26*, 130–143.

Mrozek, R.A., Cole, P.J., Otim, K.J., Shull, K.R., and Lenhart, J.L. (2011). Influence of solvent size on the mechanical properties and rheology of polydimethylsiloxane-based polymeric gels. Polymer *52*, 3422–3430.

Murphy, E. a., and Boyle, F.J. (2012). Reducing In-Stent Restenosis Through Novel Stent Flow Field Augmentation. Cardiovasc. Eng. Technol. *3*, 353–373.

Nagai, Y., Fleg, J.L., Kemper, M.K., Rywik, T.M., Earley, C.J., and Metter, E.J. (1999). Carotid arterial stiffness as a surrogate for aortic stiffness: relationship between carotid artery pressure–strain elastic modulus and aortic pulse wave velocity. Ultrasound Med. Biol. *25*, 181–188.

Nagel, T., Resnick, N., Dewey, C.F., and Gimbrone, M.A. (1999). Vascular Endothelial Cells Respond to Spatial Gradients in Fluid Shear Stress by Enhanced Activation of Transcription Factors. Arterioscler. Thromb. Vasc. Biol. *19*, 1825–1834.

Nagiah, N., Johnson, R., Anderson, R., Elliott, W., and Tan, W. (2015). Highly Compliant Vascular Grafts with Gelatin-Sheathed Coaxially Structured Nanofibers. Langmuir *31*, 12993–13002.

Nakajima, Y., Yamagishi, T., Hokari, S., and Nakamura, H. (2000). Mechanisms involved in valvuloseptal endocardial cushion formation in early cardiogenesis: Roles of transforming growth factor (TGF)-β and bone morphogenetic protein (BMP). Anat. Rec. *258*, 119–127.

Neufurth, M., Wang, X., Tolba, E., Dorweiler, B., Schröder, H.C., Link, T., Diehl-Seifert, B., and Müller, W.E.G. (2015). Modular Small Diameter Vascular Grafts with Bioactive Functionalities. PLOS ONE *10*, e0133632.

Nickerson, M.T., Patel, J., Heyd, D.V., Rousseau, D., and Paulson, A.T. (2006). Kinetic and mechanistic considerations in the gelation of genipin-crosslinked gelatin. Int. J. Biol. Macromol. *39*, 298–302.

Noris, M., Morigi, M., Donadelli, R., Aiello, S., Foppolo, M., Todeschini, M., Orisio, S., Remuzzi, G., and Remuzzi, A. (1995). Nitric Oxide Synthesis by Cultured Endothelial Cells Is Modulated by Flow Conditions. Circ. Res. *76*, 536–543.

Ojha, M. (1994). Wall shear stress temporal gradient and anastomotic intimal hyperplasia. Circ. Res. *74*, 1227–1231.

Okuhn, S.P., Connelly, D.P., Calakos, N., Ferrell, L., Man-Xiang, P., and Goldstone, J. (1989). Does compliance mismatch alone cause neointimal hyperplasia? J. Vasc. Surg. *9*, 35–45.

O'Rourke, M.F., and Hashimoto, J. (2007). Mechanical Factors in Arterial AgingA Clinical Perspective. J. Am. Coll. Cardiol. *50*, 1–13.

O'Rourke, M.F., Nichols, W.W., and Vlachopoulos, C. (2011). McDonald's Blood Flow in Arteries, Sixth Edition: Theoretical, Experimental and Clinical Principles (London: CRC Press).

Owens, C.D. (2010). Adaptive changes in autogenous vein grafts for arterial reconstruction: Clinical implications. J. Vasc. Surg. *51*, 736–746.

Palevsky, H.I., Schloo, B.L., Pietra, G.G., Weber, K.T., Janicki, J.S., Rubin, E., and Fishman, A.P. (1989). Primary pulmonary hypertension. Vascular structure, morphometry, and responsiveness to vasodilator agents. Circulation *80*, 1207–1221.

Panaritis, V., Kyriakidis, A.V., Pyrgioti, M., Raffo, L., Anagnostopoulou, E., Gourniezaki, G., and Koukou, E. (2005). Pulsatility index of temporal and renal arteries as an early finding of arteriopathy in diabetic patients. Ann. Vasc. Surg. *19*, 80–83.

Park, S., Hung, C.T., and Ateshian, G.A. (2004). Mechanical response of bovine articular cartilage under dynamic unconfined compression loading at physiological stress levels. Osteoarthritis Cartilage *12*, 65–73.

Peiffer, V., Sherwin, S.J., and Weinberg, P.D. (2013). Computation in the rabbit aorta of a new metric - the transverse wall shear stress - to quantify the multidirectional character of disturbed blood flow. J. Biomech. *46*, 2651–2658.

Peloquin, J., Huynh, J., Williams, R.M., and Reinhart-King, C.A. (2011). Indentation measurements of the subendothelial matrix in bovine carotid arteries. J. Biomech. *44*, 815–821.

Peppas, N.A., Bures, P., Leobandung, W., and Ichikawa, H. (2000). Hydrogels in pharmaceutical formulations. Eur. J. Pharm. Biopharm. *50*, 27–46.

Perktold, K., Hofer, M., Rappitsch, G., Loew, M., Kuban, B.D., and Friedman, M.H. (1997). Validated computation of physiologic flow in a realistic coronary artery branch. J. Biomech. *31*, 217–228.

Pries, A.R., Reglin, B., and Secomb, T.W. (2005). Remodeling of Blood Vessels: Responses of Diameter and Wall Thickness to Hemodynamic and Metabolic Stimuli. Hypertension *46*, 725–731.

Pritchard, W.F., Davies, P.F., Derafshq, Z., Polacek, D.C., Tsao, R., Dull, R., Jones, S.A., and Giddens, D.P. (1995). Effects of wall shear stress and fluid recirculation on the localization of circulating monocytes in a three-dimensional flow model. *28*.

Raghu, R., and Taylor, C.A. (2011). Verification of a one-dimensional finite element method for modeling blood flow in the cardiovascular system incorporating a viscoelastic wall model. Finite Elem. Anal. Des. *47*, 586–592.

Raghu, R., Vignon-Clementel, I.E., Figueroa, C.A., and Taylor, C.A. (2011). Comparative study of viscoelastic arterial wall models in nonlinear one-dimensional finite element simulations of blood flow. J. Biomech. Eng. *133*, 081003.

Ramstack, J.M., Zuckerman, L., and Mockros, L.F. (1979). Shear-induced activation of platelets. J. Biomech. *12*, 113–125.

Redheuil, A., Yu, W.-C., Wu, C.O., Mousseaux, E., de Cesare, A., Yan, R., Kachenoura, N., Bluemke, D., and Lima, J.A.C. (2010). Reduced Ascending Aortic Strain and Distensibility Earliest Manifestations of Vascular Aging in Humans. Hypertension *55*, 319–326.

Rekhter, M., Nicholls, S., Ferguson, M., and Gordon, D. (1993). Cell proliferation in human arteriovenous fistulas used for hemodialysis. Arterioscler. Thromb. Vasc. Biol. *13*, 609–617.

Resnick, N., and Gimbrone, M.A. (1995). Hemodynamic forces are complex regulators of endothelial gene expression. FASEB J. *9*, 874–882.

Ross Ethier, C., Steinman, D.A., Zhang, X., Karpik, S.R., and Ojha, M. (1998). Flow waveform effects on end-to-side anastomotic flow patterns. J. Biomech. *31*, 609–617.

Saha, K., Keung, A.J., Irwin, E.F., Li, Y., Little, L., Schaffer, D.V., and Healy, K.E. (2008). Substrate Modulus Directs Neural Stem Cell Behavior. Biophys. J. *95*, 4426–4438.

Sakamoto, N., Ohashi, T., and Sato, M. (2006). Effect of Fluid Shear Stress on Migration of Vascular Smooth Muscle Cells in Cocultured Model. Ann. Biomed. Eng. *34*, 408–415.

Sakao, S. (2006). Apoptosis of pulmonary microvascular endothelial cells stimulates vascular smooth muscle cell growth. AJP Lung Cell. Mol. Physiol. *291*, L362–L368.

Sakao, S., Taraseviciene-Stewart, L., Lee, J.D., Wood, K., Cool, C.D., and Voelkel, N.F. (2005). Initial apoptosis is followed by increased proliferation of apoptosis-resistant endothelial cells. FASEB J. *19*, 1178–1180.

Sakao, S., Taraseviciene-Stewart, L., Cool, C.D., Tada, Y., Kasahara, Y., Kurosu, K., Tanabe, N., Takiguchi, Y., Tatsumi, K., Kuriyama, T., et al. (2007). VEGF-R blockade causes endothelial cell apoptosis, expansion of surviving CD34+ precursor cells and transdifferentiation to smooth muscle-like and neuronal-like cells. FASEB J. *21*, 3640–3652.

Sakao, S., Tatsumi, K., and Voelkel, N.F. (2009). Endothelial cells and pulmonary arterial hypertension: apoptosis, proliferation, interaction and transdifferentiation. Respir. Res. *10*, 95.

Salacinski, H.J., Goldner, S., Giudiceandrea, A., Hamilton, G., Seifalian, A.M., Edwards, A., and Carson, R.J. (2001). The Mechanical Behavior of Vascular Grafts: A Review. J. Biomater. Appl. *15*, 241–278.

Sankaran, K.K., Subramanian, A., Krishnan, U.M., and Sethuraman, S. (2015). Nanoarchitecture of scaffolds and endothelial cells in engineering small diameter vascular grafts. Biotechnol. J. *10*, 96–108.

Sarkar, S., Salacinski, H.J., Hamilton, G., and Seifalian, A.M. (2006). The Mechanical Properties of Infrainguinal Vascular Bypass Grafts: Their Role in Influencing Patency. Eur. J. Vasc. Endovasc. Surg. *31*, 627–636.

Sarkar, S., Schmitz-Rixen, T., Hamilton, G., and Seifalian, A.M. (2007). Achieving the ideal properties for vascular bypass grafts using a tissue engineered approach: a review. Med. Biol. Eng. Comput. *45*, 327–336.

Scott, D., Tan, Y., Shandas, R., Stenmark, K.R., and Tan, W. (2013). High pulsatility flow stimulates smooth muscle cell hypertrophy and contractile protein expression. AJP Lung Cell. Mol. Physiol. *304*, L70–L81.

Scott-Drechsel, D., Su, Z., Hunter, K., Li, M., Shandas, R., and Tan, W. (2012). A new flow co-culture system for studying mechanobiology effects of pulse flow waves. Cytotechnology *64*, 649–666.

Seifalian, A.M., Tiwari, A., Hamilton, G., and Salacinski, H.J. (2002). Improving the clinical patency of prosthetic vascular and coronary bypass grafts: the role of seeding and tissue engineering. Artif. Organs *26*, 307–320.

Sen, B., Xie, Z., Case, N., Ma, M., Rubin, C., and Rubin, J. (2008). Mechanical Strain Inhibits Adipogenesis in Mesenchymal Stem Cells by Stimulating a Durable β-Catenin Signal. Endocrinology *149*, 6065–6075.

Shadwick, R.E. (1999). Mechanical design in arteries. J. Exp. Biol. *202*, 3305–3313.

Shav, D., Gotlieb, R., Zaretsky, U., Elad, D., and Einav, S. (2014). Wall Shear Stress Effects on Endothelial-Endothelial and Endothelial-Smooth Muscle Cell Interactions in Tissue Engineered Models of the Vascular Wall. PLoS ONE *9*, e88304.

Shi, Z.-D., Ji, X.-Y., Qazi, H., and Tarbell, J.M. (2009). Interstitial flow promotes vascular fibroblast, myofibroblast, and smooth muscle cell motility in 3-D collagen I via upregulation of MMP-1. AJP Heart Circ. Physiol. *297*, H1225–H1234.

Shin, H.Y., Gerritsen, M.E., and Bizios, R. (2002). Regulation of Endothelial Cell Proliferation and Apoptosis by Cyclic Pressure. Ann. Biomed. Eng. *30*, 297–304.

Sho, E., Sho, M., Singh, T.M., Nanjo, H., Komatsu, M., Xu, C., Masuda, H., and Zarins, C.K. (2002a). Arterial Enlargement in Response to High Flow Requires Early Expression of Matrix Metalloproteinases to Degrade Extracellular Matrix. Exp. Mol. Pathol. *73*, 142–153.

Sho, M., Sho, E., Singh, T.M., Komatsu, M., Sugita, A., Xu, C., Nanjo, H., Zarins, C.K., and Masuda, H. (2002b). Subnormal Shear Stress-Induced Intimal Thickening Requires Medial Smooth Muscle Cell Proliferation and Migration. Exp. Mol. Pathol. *72*, 150–160.

Silva, S.S., Maniglio, D., Motta, A., Mano, J.F., Reis, R.L., and Migliaresi, C. (2008a). Genipin-Modified Silk-Fibroin Nanometric Nets. Macromol. Biosci. *8*, 766–774.

Silva, S.S., Motta, A., Rodrigues, M.T., Pinheiro, A.F.M., Gomes, M.E., Mano, J.F., Reis, R.L., and Migliaresi, C. (2008b). Novel Genipin-Cross-Linked Chitosan/Silk Fibroin Sponges for Cartilage Engineering Strategies. Biomacromolecules *9*, 2764–2774.

Simmons, C.A., Matlis, S., Thornton, A.J., Chen, S., Wang, C.-Y., and Mooney, D.J. (2003). Cyclic strain enhances matrix mineralization by adult human mesenchymal stem cells via the extracellular signal-regulated kinase (ERK1/2) signaling pathway. J. Biomech. *36*, 1087–1096.

Soletti, L., Hong, Y., Guan, J., Stankus, J.J., El-Kurdi, M.S., Wagner, W.R., and Vorp, D.A. (2010). A bilayered elastomeric scaffold for tissue engineering of small diameter vascular grafts. Acta Biomater. *6*, 110–122.

Solovyan, V.T., and Keski-Oja, J. (2005). Apoptosis of human endothelial cells is accompanied by proteolytic processing of latent TGF-β binding proteins and activation of TGF-β. Cell Death Differ. *12*, 815–826.

Song, S., Wu, P., Ye, M., Feng, J., and Yang, Y. (2008). Effect of small amount of ultra high molecular weight component on the crystallization behaviors of bimodal high density polyethylene. Polymer *49*, 2964–2973.

Sottiurai, V.S., Yao, J.S.T., Flinn, W.R., and Batson, R.C. (1983). Intimal hyperplasia and neointima: An ultrastructural analysis of thrombosed grafts in humans. Surgery *93*, 809–817.

Stewart, S.F., and Lyman, D.J. (1992). Effects of a vascular graft/natural artery compliance mismatch on pulsatile flow. J. Biomech. *25*, 297–310.

Stonebridge, P.A. (2011). Three-dimensional blood flow dynamics: spiral/helical laminar flow. Methodist DeBakey Cardiovasc. J. *7*, 21–26.

Stonebridge, P.A., and Brophy, C.M. (1991). Spiral laminar flow in arteries? The Lancet *338*, 1360–1361.

Stonebridge, P.A., Hoskins, P.R., Allan, P.L., and Belch, J.F.F. (1996). Spiral laminar flow in vivo. Clin. Sci. *91*, 17–21.

Stonebridge, P.A., Vermassen, F., Dick, J., Belch, J.J.F., and Houston, G. (2012). Spiral laminar flow prosthetic bypass graft: medium-term results from a first-in-man structured registry study. Ann. Vasc. Surg. *26*, 1093–1099.

Sun, A., Fan, Y., and Deng, X. (2010). Numerical Comparative Study on the Hemodynamic Performance of a New Helical Graft With Noncircular Cross Section and SwirlGraft. Artif. Organs *34*, 22–27.

Sun, W., Incitti, T., Migliaresi, C., Quattrone, A., Casarosa, S., and Motta, A. (2014). Genipin-crosslinked gelatin-silk fibroin hydrogels for modulating the behaviour of pluripotent cells: Modulating the behaviour of pluripotent cells. J. Tissue Eng. Regen. Med. n/a-n/a.

Sunamura, M., Ishibashi, H., and Karino, T. (2007). Flow patterns and preferred sites of intimal thickening in diameter-mismatched vein graft interpositions. Surgery *141*, 764–776.

Sundararaghavan, H.G., Monteiro, G.A., Lapin, N.A., Chabal, Y.J., Miksan, J.R., and Shreiber, D.I. (2008). Genipin-induced changes in collagen gels: Correlation of mechanical properties to fluorescence. J. Biomed. Mater. Res. A *87A*, 308–320.

Suryani, and Liu, Y.-L. (2009). Preparation and properties of nanocomposite membranes of polybenzimidazole/sulfonated silica nanoparticles for proton exchange membranes. J. Membr. Sci. *332*, 121–128.

Suwanabol, P.A., Seedial, S.M., Shi, X., Zhang, F., Yamanouchi, D., Roenneburg, D., Liu, B., and Kent, K.C. (2012). Transforming growth factor-β increases vascular smooth muscle cell proliferation through the Smad3 and extracellular signal-regulated kinase mitogen-activated protein kinases pathways. J. Vasc. Surg. *56*, 446–454.e1.

Takada, Y., Shinkai, F., Kondo, S., Yamamoto, S., Tsuboi, H., Korenaga, R., and Ando, J. (1994). Fluid shear stress increases the expression of thrombomodulin by cultured human endothelial cells. Biochem. Biophys. Res. Commun. *205*, 1345–1352.

Takeuchi, H., and Cohen, C. (1999). Reinforcement of Poly(dimethylsiloxane) Elastomers by Chain-End Anchoring to Clay Particles. Macromolecules *32*, 6792–6799.

Tan, Y., Tseng, P.-O., Wang, D., Zhang, H., Hunter, K., Hertzberg, J., Stenmark, K.R., and Tan, W. (2014). Stiffening-Induced High Pulsatility Flow Activates Endothelial Inflammation via a TLR2/NF-κB Pathway. PLoS ONE *9*, e102195.

Tanaka, T.T., and Fung, Y.-C. (1974). Elastic and inelastic properties of the canine aorta and their variation along the aortic tree. J. Biomech. *7*, 357–370.

Taylor, M.G. (1959). An Experimental Determination of the Propagation of Fluid Oscillations in a Tube with a Visco-elastic Wall; together with an Analysis of the Characteristics Required in an Electrical Analogue. Phys. Med. Biol. *4*, 63.

Ten Dijke, P., Egorova, A.D., Goumans, M.-J.T.H., Poelmann, R.E., and Hierck, B.P. (2012). TGF-β signaling in endothelial-to-mesenchymal transition: the role of shear stress and primary cilia. Sci. Signal. *5*, pt2.

Traub, O., and Berk, B.C. (1998). Laminar Shear Stress : Mechanisms by Which Endothelial Cells Transduce an Atheroprotective Force. Arterioscler. Thromb. Vasc. Biol. *18*, 677–685.

Tsai, S., Hollenbeck, S.T., Ryer, E.J., Edlin, R., Yamanouchi, D., Kundi, R., Wang, C., Liu, B., and Kent, K.C. (2009). TGF-β through Smad3 signaling stimulates vascular smooth muscle cell proliferation and neointimal formation. Am. J. Physiol. - Heart Circ. Physiol. *297*, H540–H549.

Uematsu, M., Ohara, Y., Navas, J.P., Nishida, K., Murphy, T.J., Alexander, R.W., Nerem, R.M., and Harrison, D.G. (1995). Regulation of endothelial cell nitric oxide synthase mRNA expression by shear stress. Am. J. Physiol. - Cell Physiol. *269*, C1371–C1378.

Urbich, C. (2002). Shear Stress-Induced Endothelial Cell Migration Involves Integrin Signaling Via the Fibronectin Receptor Subunits alpha5 and beta1. Arterioscler. Thromb. Vasc. Biol. *22*, 69–75.

Uttayarat, P., Perets, A., Li, M., Pimton, P., Stachelek, S.J., Alferiev, I., Composto, R.J., Levy, R.J., and Lelkes, P.I. (2010). Micropatterning of three-dimensional electrospun polyurethane vascular grafts. Acta Biomater. *6*, 4229–4237.

Valdez-Jasso, D., Bia, D., Zócalo, Y., Armentano, R.L., Haider, M.A., and Olufsen, M.S. (2011). Linear and nonlinear viscoelastic modeling of aorta and carotid pressure-area dynamics under in vivo and ex vivo conditions. Ann. Biomed. Eng. *39*, 1438–1456.

Varcoe, R.L., Mikhail, M., Guiffre, A.K., Pennings, G., Vicaretti, M., Hawthorne, W.J., Fletcher, J.P., and Medbury, H.J. (2006). The role of the fibrocyte in intimal hyperplasia. J. Thromb. Haemost. *4*, 1125–1133.

Vepari, C., and Kaplan, D.L. (2007). Silk as a biomaterial. Prog. Polym. Sci. *32*, 991–1007.

Vernhet, H., Demaria, R., Juan, J.M., Oliva-Lauraire, M.C., Sénac, J.P., and Dauzat, M. (2001). Changes in wall mechanics after endovascular stenting in the rabbit aorta: comparison of three stent designs. Am. J. Roentgenol. *176*, 803–807.

Vignon-Clementel, I.E., Figueroa, C.A., and Taylor, C.A. Comparative Study of Viscoelastic Arterial Wall Models in Nonlinear One-Dimensional Finite Element Simulations of Blood Flow.

Wagenseil, J.E., and Mecham, R.P. (2009). Vascular Extracellular Matrix and Arterial Mechanics. Physiol. Rev. *89*, 957–989.

Wahlgren, M., and Arnebrant, T. (1991). Protein adsorption to solid surfaces. Trends Biotechnol. *9*, 201–208.

Wang, H.-B., Dembo, M., and Wang, Y.-L. (2000). Substrate flexibility regulates growth and apoptosis of normal but not transformed cells. Am. J. Physiol.-Cell Physiol. *279*, C1345–C1350.

Wang, H.Q., Huang, L.X., Qu, M.J., Yan, Z.Q., Liu, B., Shen, B.R., and Jiang, Z.L. (2006). Shear Stress Protects against Endothelial Regulation of Vascular Smooth Muscle Cell Migration in a Coculture System. Endothelium *13*, 171–180.

Wang, L., Wang, Y., Qu, J., Hu, Y., You, R., and Li, M. (2013a). The Cytocompatibility of Genipin-Crosslinked Silk Fibroin Films. J. Biomater. Nanobiotechnology *04*, 213–221.

Wang, X.-F., Fullana, J.-M., Lagree, P.-Y., and Armentano, R.L. (2013b). Effect of viscoelasticity of arterial wall on pulse wave: a comparative study on ovine: Computer Methods in Biomechanics and Biomedical Engineering: Vol 16, No sup1.

Wang, X.-F., Nishi, S., Matsukawa, M., Ghigo, A., Lagrée, P.-Y., and Fullana, J.-M. (2016). Fluid friction and wall viscosity of the 1D blood flow model. J. Biomech. *49*, 565–571.

Wang, Y., Rodriguez-Perez, M.A., Reis, R.L., and Mano, J.F. (2005). Thermal and Thermomechanical Behaviour of Polycaprolactone and Starch/Polycaprolactone Blends for Biomedical Applications. Macromol. Mater. Eng. *290*, 792–801.

Wang, Z., Lakes, R.S., Golob, M., Eickhoff, J.C., and Chesler, N.C. (2013c). Changes in Large Pulmonary Arterial Viscoelasticity in Chronic Pulmonary Hypertension. PLoS ONE *8*, e78569.

White, S.S., Zarins, C.K., Giddens, D.P., Bassiouny, H., Loth, F., Jones, S.A., and Glagov, S. (1993). Hemodynamic patterns in two models of end-to-side vascular graft anastomoses: Effects of pulsatility, flow division, Reynolds number, and hood length. J. Biomech. Eng. *115*, 104–111.

Whittemore, A.D., Clowes, A.W., Couch, N.P., and Mannick, J.A. (1981). Secondary femoropopliteal reconstruction. Ann. Surg. *193*, 35–42.

Wingate, K., Bonani, W., Tan, Y., Bryant, S.J., and Tan, W. (2012). Compressive elasticity of three-dimensional nanofiber matrix directs mesenchymal stem cell differentiation to vascular cells with endothelial or smooth muscle cell markers. Acta Biomater. *8*, 1440–1449.

Wise, S.G., Byrom, M.J., Waterhouse, A., Bannon, P.G., Ng, M.K.C., and Weiss, A.S. (2011). A multilayered synthetic human elastin/polycaprolactone hybrid vascular graft with tailored mechanical properties. Acta Biomater. *7*, 295–303.

Wottawah, F., Schinkinger, S., Lincoln, B., Ananthakrishnan, R., Romeyke, M., Guck, J., and Käs, J. (2005). Optical Rheology of Biological Cells. Phys. Rev. Lett. *94*.

Wu, M.H. (2005). Endothelial focal adhesions and barrier function. J. Physiol. *569*, 359–366.

Wurzinger, L.J., Optiz, R., Wolf, M., and Schmid-Schonbein, H. (1985). "Shear induced platelet activation" - a cricitcal reappraisal. Biorheology *22*, 399–413.

Wurzinger, L.J., Opitz, R., and Eckstein, H. (1986). Mechanical bloodtrauma. An overview. Angeiologie *38*, 81–97.

Xiao, W., Liu, W., Sun, J., Dan, X., Wei, D., and Fan, H. (2012). Ultrasonication and Genipin Cross-Linking to Prepare Novel Silk Fibroin-Gelatin Composite Hydrogel. J. Bioact. Compat. Polym. *27*, 327–341.

Yao, C. (2003). Preparation of networks of gelatin and genipin as degradable biomaterials. Mater. Chem. Phys.

Yellin, A.E., Jones, D.N., Rutherford, R.B., Ikezawa, T.B., Nishikimi, N.B., and Ishibashi, H.B. (1991). Factors affecting the patency of small-caliber prostheses: Observations in a suitable canine model. J. Vasc. Surg. *14*, 441–451.

Zarins, C.K., Giddens, D.P., Bharadvaj, B.K., Sottiurai, V.S., Mabon, R.F., and Glagov, S. (1983). Carotid bifurcation atherosclerosis. Quantitative correlation of plaque localization with flow velocity profiles and wall shear stress. Circ. Res. *53*, 502–514.

Zebda, N., Dubrovskyi, O., and Birukov, K.G. (2012). Focal Adhesion Kinase Regulation of Mechanotransduction and its Impact on Endothelial Cell Functions. Microvasc. Res. *83*, 71–81.

Zeisberg, E.M., Tarnavski, O., Zeisberg, M., Dorfman, A.L., McMullen, J.R., Gustafsson, E., Chandraker, A., Yuan, X., Pu, W.T., Roberts, A.B., et al. (2007a). Endothelial-to-mesenchymal transition contributes to cardiac fibrosis. Nat. Med. *13*, 952–961.

Zeisberg, E.M., Potenta, S., Xie, L., Zeisberg, M., and Kalluri, R. (2007b). Discovery of Endothelial to Mesenchymal Transition as a Source for Carcinoma-Associated Fibroblasts. Cancer Res. *67*, 10123–10128.

Zeisberg, E.M., Potenta, S.E., Sugimoto, H., Zeisberg, M., and Kalluri, R. (2008). Fibroblasts in Kidney Fibrosis Emerge via Endothelial-to-Mesenchymal Transition. J. Am. Soc. Nephrol. *19*, 2282–2287.

Zhao, X. (2014). Multi-scale multi-mechanism design of tough hydrogels: building dissipation into stretchy networks. Soft Matter *10*, 672–687.

Zhao, Y., Nakajima, T., Yang, J.J., Kurokawa, T., Liu, J., Lu, J., Mizumoto, S., Sugahara, K., Kitamura, N., Yasuda, K., et al. (2014). Proteoglycans and Glycosaminoglycans Improve Toughness of Biocompatible Double Network Hydrogels. Adv. Mater. *26*, 436–442.

Zheng, T., Fan, Y., Xiong, Y., Jiang, W., and Deng, X. (2009). Hemodynamic performance study on small diameter helical grafts. ASAIO J. Am. Soc. Artif. Intern. Organs 1992 *55*, 192–199.

Ziegler, T., Bouzourène, K., Harrison, V.J., Brunner, H.R., and Hayoz, D. (1998). Influence of oscillatory and unidirectional flow environments on the expression of endothelin and nitric oxide synthase in cultured endothelial cells. Arterioscler. Thromb. Vasc. Biol. *18*, 686–692.

Zieman, S.J. (2005). Mechanisms, Pathophysiology, and Therapy of Arterial Stiffness. Arterioscler. Thromb. Vasc. Biol. *25*, 932–943.

Zieman, S.J., Melenovsky, V., and Kass, D.A. (2005). Mechanisms, Pathophysiology, and Therapy of Arterial Stiffness. Arterioscler. Thromb. Vasc. Biol. *25*, 932–943.

APPENDIX 1: Mechanics of the Tube

A1.1   Thick-Walled Pressure Vessel Mechanics
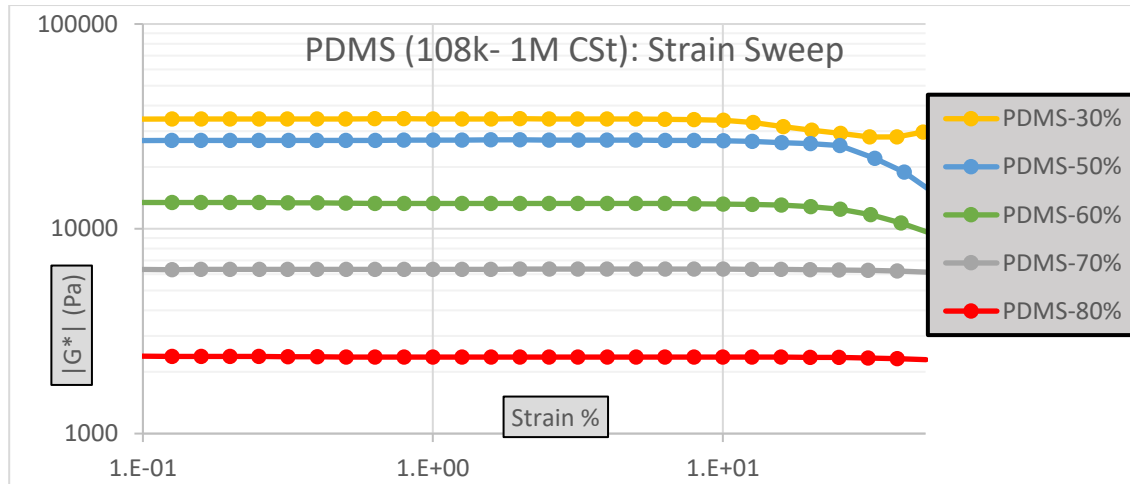
A1.1.1 Material Characterization

Figure A1.1.1.1- Strain sweep on PDMS gels with 108 kDa v-PDMS chains, and 1 million CSt viscosity. At 10% strain, complex modulus values begin to decrease, indicating strain softening. This softening effect decreases for softer gels.

As can be seen in results shown above, strain softening begins to occur at approximately 10% strain for stiffer gels (30%-50%), and occurs outside the range in softer gels (70%-80%). This range is well within the proposed compliance of 5-9%.
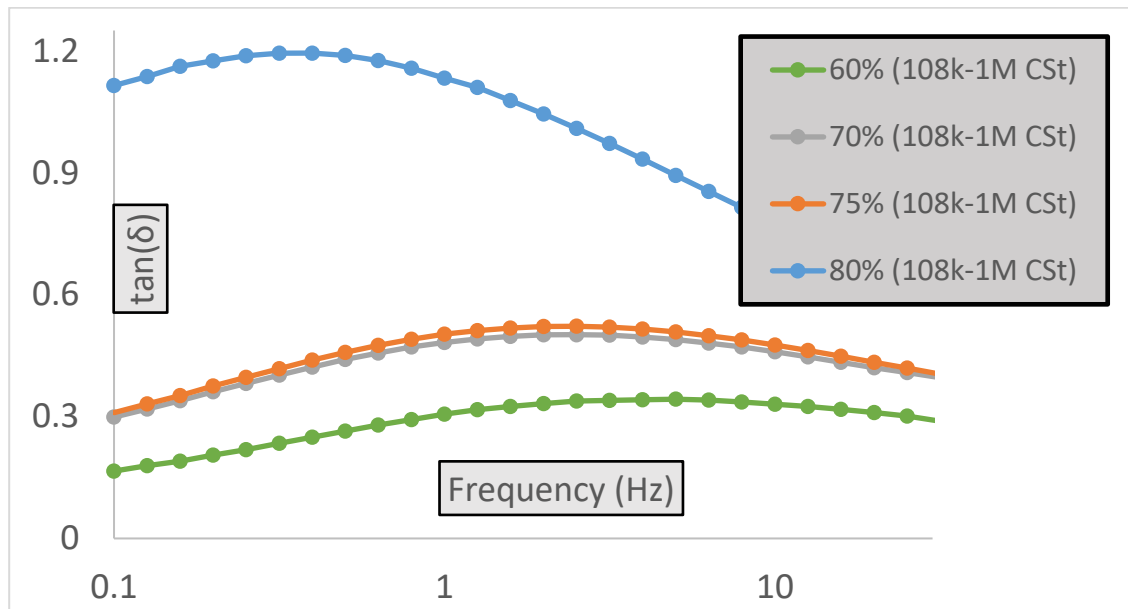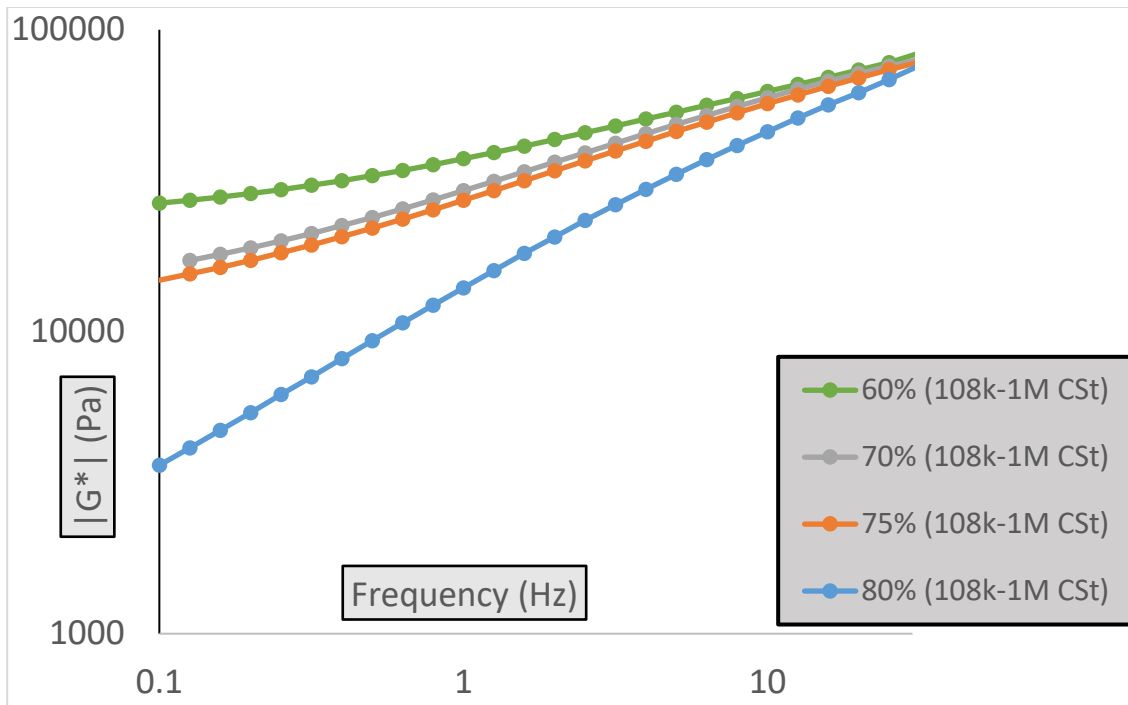
Figure A1.1.1.2- Shear modulus magnitude (|G*|) and ratio of viscous to elastic response (tan(δ)). Material stiffness and viscous response both correlate well with increased m-PDMS, as seen in the literature.

	Elastic (58.8% 500 CSt : 108 kDa PDMS)	Viscoelastic (70% 1M CSt : 108 kDa PDMS)
Material	**E' = 68.9 kPa**	**E'= 67.1 kPa**
Properties at 1 Hz	**E''= 4.09 kPa**	**E''= 32.3 kPa**
	tan(δ) = 0.06	**tan(δ) = 0.482**
	Method: DMA	Method: Rheometry

Table A.1.1.1- Frequency dependent material properties of poly(dimethylsiloxane) (PDMS).

A1.1.2 Radial Wall Strain

Thick-walled pressure vessel mechanics were used to cater inner lumen mechanics to two different compliances. This was done by casting the compliant tubes within a polypropylene jacket, which was treated as rigid. This allowed similar material properties between the viscoelastic and the elastic tubes, and equivalent frequency-dependent material properties between compliant and non-compliant tubes. Governing equations for the compliance of the thick-walled pressure vessel began with equation listed in section 5.3.2.

$$u_r(r) = \frac{1-\nu}{E^*}\frac{(r_i^2 p_i - r_o^2 p_o)r}{r_o^2 - r_i^2} + \frac{1+\nu}{E^*}\frac{(p_i - p_o)r_i^2 r_o^2}{(r_o^2 - r_i^2)r}$$

Where, $|E^*|$ is the magnitude of the complex shear modulus of the material, ν is 0.5 for Poisson's ratio for PDMS, p_i is the pressure inside the lumen, p_o is the pressure at the outer wall of the rigid jacket, r_i is the starting inner lumen radius, and r_o is the radius of the outer jacket.

Here the outer pressure must be solved for by setting the motion at the outer radius to 0, and solving for p_o:

$$u_r(r_o) = 0 \rightarrow p_o = \frac{4r_i^2}{r_o^2 + 3r_i^2}p_i$$

This may then be inserted for p_o:

$$u_r(r = r_i) = \frac{p_i}{2\,E^*} \frac{3r_i\left(r_i^2 - r_o^2\right)^2}{(r_o^2 - r_i^2)(r_o^2 + 3r_i^2)}$$

Form this we can integrate the measured frequency-dependent values of the material, and harmonics of the complex pressure wave by applying a discrete Fourier transform:

$$u_r(r = r_i) = \mathcal{F}^{-1}\left\{\frac{\mathcal{F}\{p_i\}}{G^*}\right\} \frac{r_i\left(r_i^2 - r_o^2\right)^2}{2(r_o^2 - r_i^2)(r_o^2 + 3r_i^2)}$$

From this, we can then prepare for the tube mechanics.

A1.1.3   Longitudinal Strain

Longitudinal strain would result from radial distension. This may be based on isovolumetric properties of PDMS ($v = 0.5$). Therefore, in examining a maximum radial strain of 10%, the change in longitudinal strain may be determined by simply accounting for the change in area resulting from radial strain:

$$V = const. \rightarrow L \cdot A = L_0 \cdot A_0$$

$$\varepsilon_x = \frac{\frac{L_0 A_0}{A} - L_0}{L_0} = \frac{A_0}{A} - 1 = \frac{r_o^2 - r_i^2}{r_o^2 - (\lambda r_i)^2} - 1$$

Where λ is the stretch ratio of the radial deformation. Applying conservative projected values of lambda towards both compliant and non-compliant tubes, ($\lambda = 0.9$ and 0.98, respectively). Resulting longitudinal strain values were 0.66% and 1.3% for compliant and non-compliant, tubes respectively.

A1.1.4   Error in Radial Strain

To ensure radial strain occurs within a given error boundary across the tube, radial strain was given as a function of lateral translation of the lumen and location along the circumferential coordinate. The resulting equation for the radius was given as a function of pressure:

$$r_i(P) = r_i(90\,mmHg) = \frac{90\,mmHg}{G_1^*} \frac{r_i\left(r_i^2 - r_o^2\right)^2}{2(r_o^2 - r_i^2)(r_o^2 + 3r_i^2)} + r_i$$

Where, the outer radius becomes:

153

$$r_o(\delta, \theta) = (r_o(1 + \delta \, Cos(\theta)))^2$$

$$\therefore r_i(P) \rightarrow r_i(P, \delta, \theta)$$

By making the outer radius a function of error (δ) and θ, we may then establish the error in cross sectional area by summing the area over fixed intervals of θ.

$$A(\delta, \theta) = \frac{1}{2} \int_0^{2\pi} r_i(90 \, mmHg, \delta, \theta)^2 \, d\theta = \frac{d\theta}{2} \sum_0^{2\pi/d\theta} r_i(90 \, mmHg, \delta, n \, d\theta)$$

This may then be compared to the area of a perfectly centered inner lumen, with the δ term equivalent to 0:

$$\Delta = \frac{A(\delta)}{A_0} - 1$$

Lumen
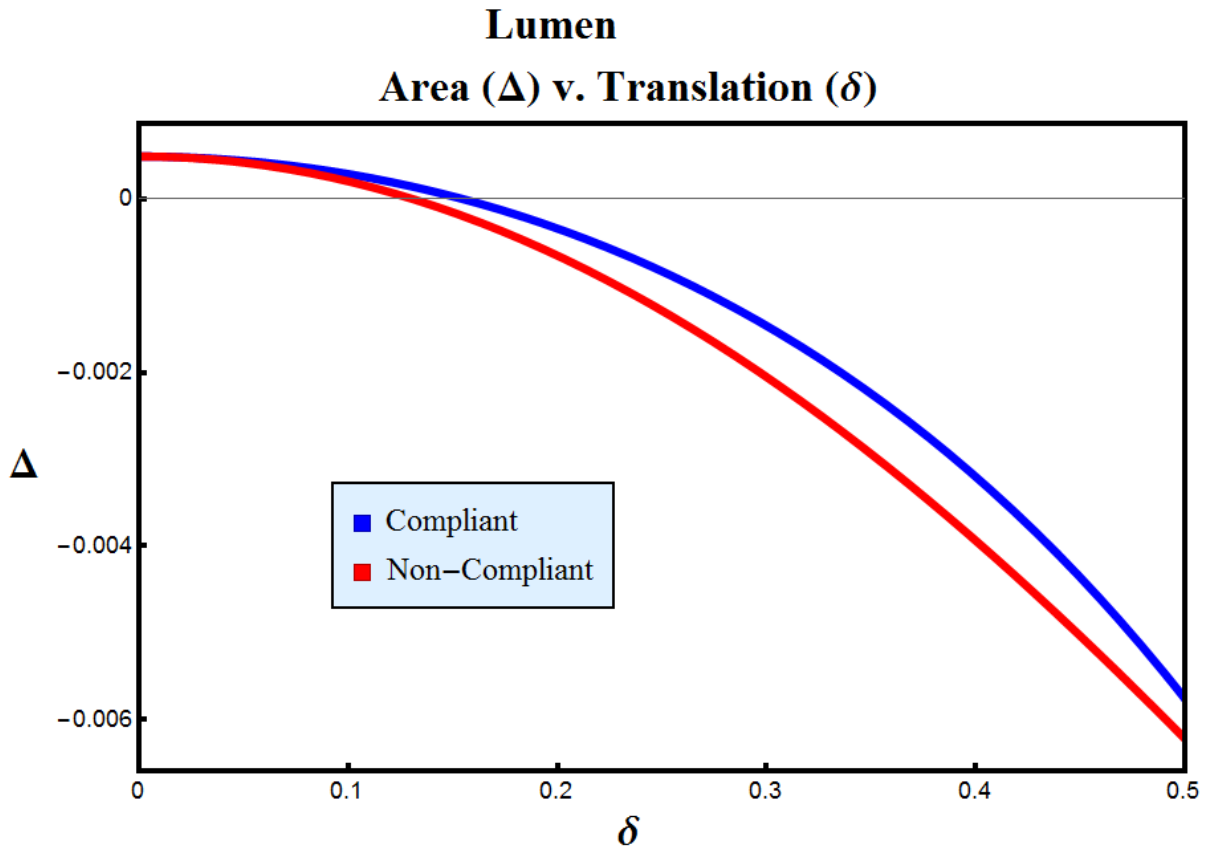## Area (Δ) v. Translation (δ)

Figure A1.1.4.1- The error is positive here at low values of δ due to the summation approximation for integrating the cross-sectional area value. By summing the area value, some area is not included within the calculated error.

APPENDIX 2: Normalization of the Flow System

A2.1 Normalizing Flow from Tee-Junction

To ensure minimal wave reflection and establish accurate volumetric flow within the flow system, connective tubing of the same cross-sectional area as the conduit must be used. To accomplish this, tee-junctions are connected to the fluid system, and Q-sensors are placed in parallel branches to the conduit line (figure A2.1.1).
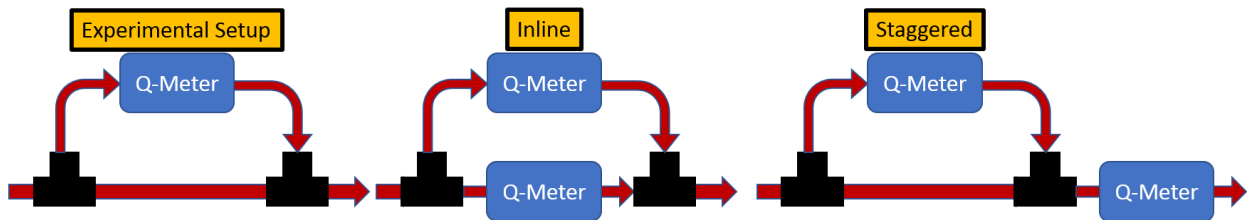

Figure A2.1.1- Different Flow (Q) sensor setup to determine effects of tee-junctions on volumetric flow rates. Here we see the experimental setup used to reduce wave reflections, inline measurement to compare phase shifts due to the tee-junction, and staggered measurement to compare Fourier harmonic amplitudes between the large conduit and smaller, parallel conduit.

In comparing volumetric flow rates between the parallel and staggered measurement setups, we may examine resulting phase shift and amplitude changes, respectively. Measuring in parallel demands that the outlets of the tee-junction have the same cross-sectional area, removing the effect of impedance change between the two outlets. Resulting Fourier constants indicate similar flow splitting between tee-junction outlets (figure A2.1.2), as well as phase shifts below measurement threshold (224 Hz → 0.004 s) for phase shift of the Q-measurement. Because the distance between both the parallel and perpendicular outlets is near zero, this measurement is most accurate for determining the time shift caused by splitting the flow with a tee-junction.
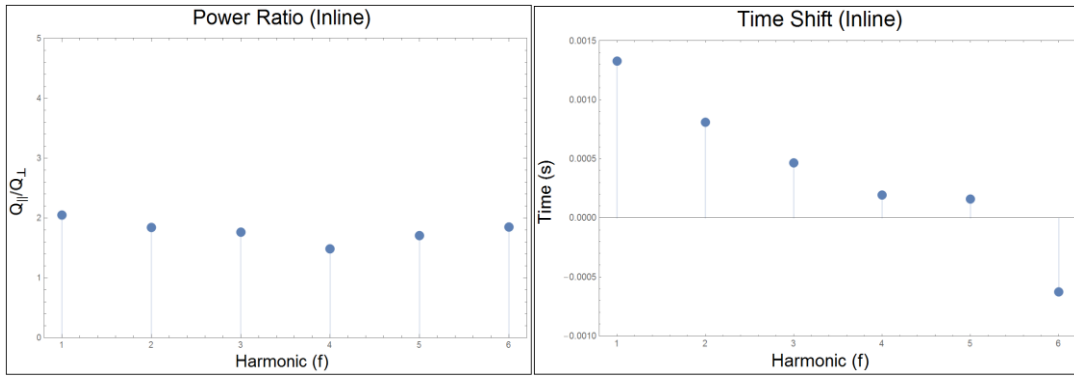
Figure A2.1.2- Power ratio (left) of the Fourier constant moduli. This was solved by finding the quotient between the Fourier power series of the parallel tee-junction outlet Q-measurement and the perpendicular tee-junction outlet. The time shift of each harmonic was also measured by the quotient of the phase shift between outlets and the angular momentum $\left(\frac{\varphi_{\parallel}-\varphi_{\perp}}{\omega}\right)$, and compared to the sampling threshold (0.004 s).

Measuring with a staggered setup allows for the flow to split at the tee-junctions according to the head loss of the tee, as well as the change in impedance due to reduced cross-sectional area of the Q-measurement. This additionally allows for the applied flow wave to be measured directly, and compared to the Q-measurement forced by the tee-junction. Here, we may see a drastic increase in harmonic moduli, with a minimal time shift of the primary harmonic. We may establish that this shift is due to the offset nature of the parallel measurement. Therefore, we may simply view the change in harmonic power to determine Q-wave amplitude in our experimental data. We multiply all Q Fourier Harmonics by the ratios plotted below in figure A2.1.3.
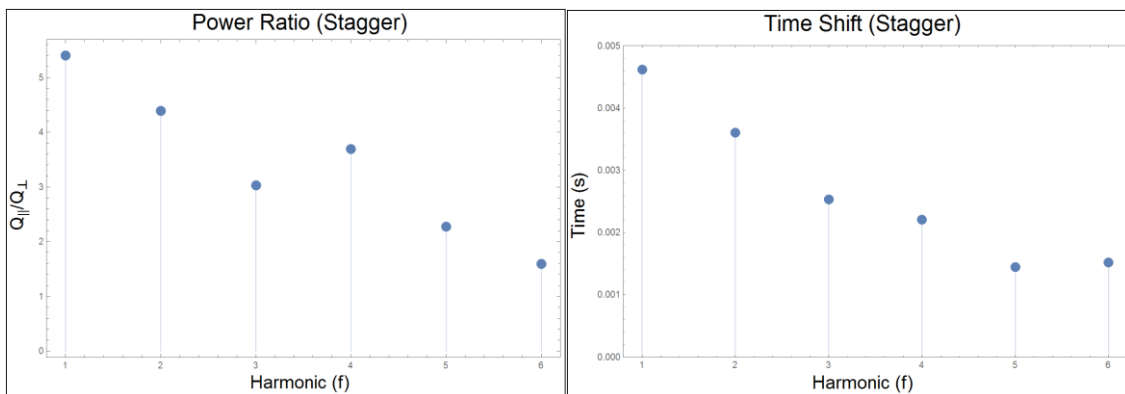

Figure A2.1.3- Power ratio (left) and time shift (right) of the Fourier constants from flow (Q) measured with a staggered Q-meter setup. This was solved similar that stated above. The time shift of each

harmonic was also measured by the quotient of the phase shift between outlets and the angular momentum $\left(\frac{\varphi_{\parallel} - \varphi_{\perp}}{\omega}\right)$, and compared to the sampling threshold (0.004 s).